Proton Radioactivity Studies

A. A. Hassan Mahmud

Thesis submitted for the degree of Doctor of Philosophy

Department of Physics and Astronomy
University of Edinburgh
2002

Abstract

A search for new examples of proton emission from ground and low-lying states was conducted at Argonne National Laboratory. Of particular interest were examples of proton emission from nuclei which were deformed or had an odd number of neutrons, the majority of known proton emitters being odd-even and near-spherical. Candidate nuclei were created via fusion evaporation, these recoils then being separated according to their mass to charge ratio by the Fragment Mass Analyser, before being implanted into a Double-Sided Silicon Strip Detector. Any subsequent alpha or proton decays were then recorded.

Proton emission from the new, deformed, odd-odd isotope ^{130}Eu was observed, with a proton decay energy of 1020(15) keV and a half-life of 900^{+610}_{-260} μs. This being assigned to the 2^+ ground state using a formalism which is discussed. The new isotope, ^{170}Au was also observed with an energy of 1735(9) keV and half-life of 570^{+310}_{-150} μs, which was assigned to a 75(15)% proton branch from the $h_{11/2}$ state. This assignment was made on the basis of a comparison of measured proton half-lives with those calculated using barrier penetration codes. The alpha decay from this new isotope is also reported. An independent observation of the proton decay of the spherical odd-odd isotope ^{164m}Ir was also made in the same experimental run. In a separate experiment, a measurement of the known proton emitter ^{117}La was combined with the search for a new proton emitter ^{116}La. Of note was the non-observation of an isomeric state, ^{117m}La, reported by Soramel *et. al.* at Legnaro. Recent theoretical calculations incorporating these new results are discussed, in particular those involving ^{130}Eu which is both odd-odd and deformed.

Declaration

No portion of the work referred to in this thesis has been submitted in support of an application for another degree qualification of this or any other university or other institute of learning.

A. A. Hassan Mahmud

Acknowledgements

The author would like to acknowledge EPSRC for funding this PhD research. Additionally, funding for the experiments which form the core of this thesis was provided by the DOE under Contract No. W-31-109-ENG-38.

Thanks are also due to the various people at Argonne and Edinburgh who assisted with experimental, technical and theoretical details in this work, in particular: Dariusz Seweryniak, Andreas Heinz, Cary Davids, Karsten Schmidt, Tom Davinson and last but not least, my supervisor, Phil Woods.

بِسْمِ اللهِ الرَّحْمٰنِ الرَّحِيمِ

Contents

List of Figures

List of Tables

Chapter 1

Introduction

1.1 Direct Proton Emission

The proton and neutron driplines represent lines beyond which nuclei are unbound with respect to a single nucleon, a proton for the proton rich side, and neutron for the neutron rich side. This manifests itself in the direct emission of the nucleon from the ground state of the nucleus, and the rapid decrease in nuclear life-times as one goes further beyond the dripline. In fact, the driplines represent the limits of nuclear stability, since the experimental observation of nuclei lying beyond them can be difficult, due to shortening half-lives. When one goes far enough past a drip-line, eventually nuclear half-lives become so small, i.e. the nuclei would be unbound by such a large energy, that they are not termed nuclei but resonances, (with $t_{1/2} \sim 10^{-21}s$).

Figure 1.1 shows the Segré chart of isotopes, the central strip of black squares being stable nuclei. At low atomic mass (A) stable nuclei have an approximately equal proton numbers (Z) and neutron number (N), though

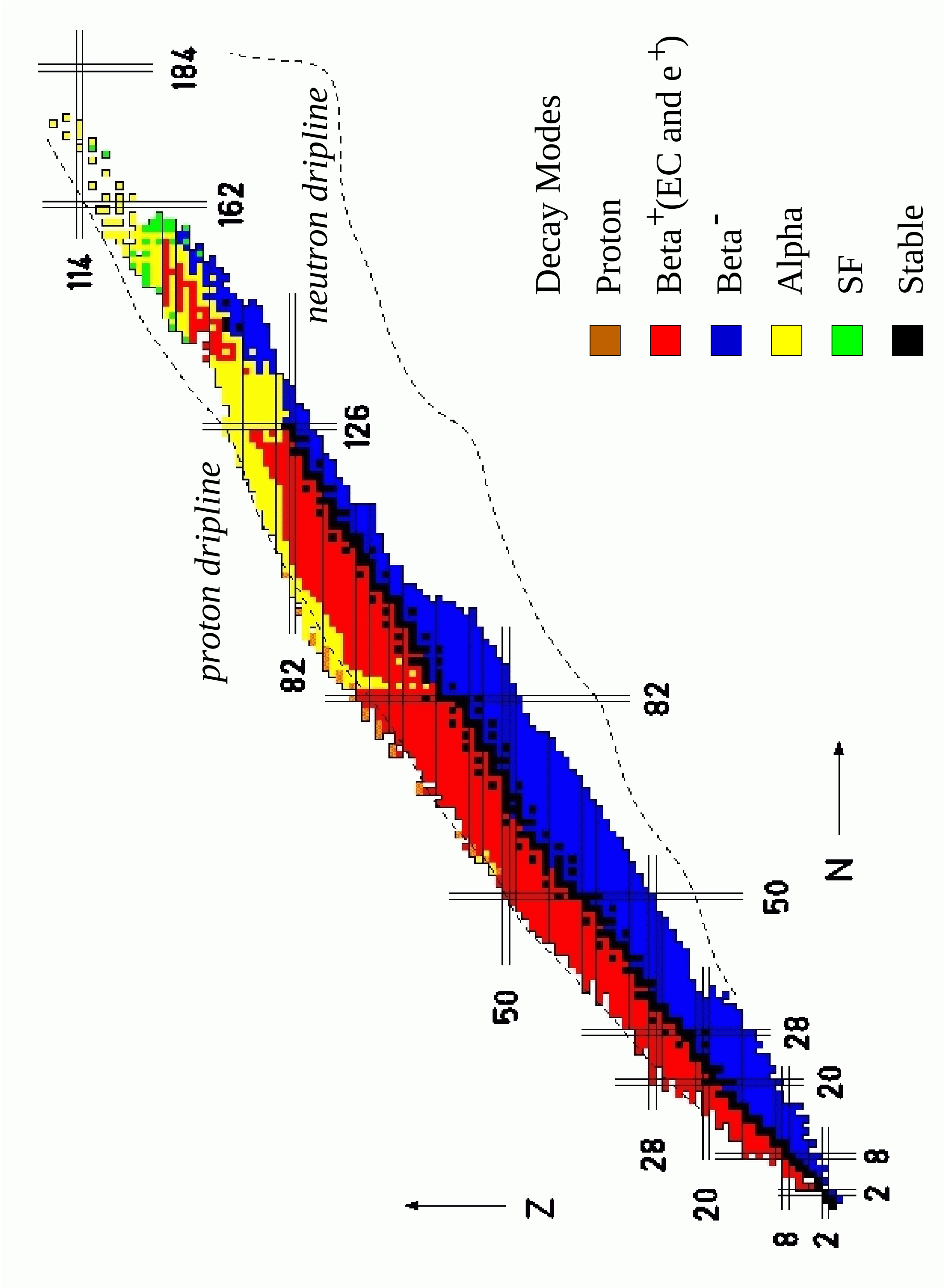

Figure 1.1: *Chart of nuclei, showing both the proton and neutron driplines, as well as the predominant decay modes of the various nuclei. The black squares are stable nuclei and the green show nuclei which decay via spontaneous fission.*

at higher mass, stable nuclei tend to be more neutron rich. This is because of the increasing influence of the repulsive Coulomb force of the constituent protons. This Coulomb repulsion is also the reason why the proton dripline is closer to the 'valley of stability' than the neutron dripline.

The most common form of decay is via β-decay, as can be seen in Fig. 1.1. Nuclei change the ratio of protons to neutrons to lie closer to stability by emitting an electron or positron (though for the second case, the possibility of electron capture of an atomic electron by the nucleus also exists). The further away from stability a nucleus lies, the greater the energy available for β-decay to occur. This brings about a gradual decrease in the lifetime of these nuclei as beta-decays occurs more quickly. Eventually, the energy available for decay is large enough that β-delayed particle emission can occur. This is due to the fact that the initial nucleus β-decays to an excited state with an energy larger than the separation energy of certain particles, in the emitting daughter. The emitting daughter nucleus then quickly de-excites by proton, alpha or neutron emission, depending on the energetics of nucleus, along with some possible γ-emission. The first example of this was $\beta\alpha$, observed by Rutherford and Wood [Rut16]. But the modern systematic search for β-delayed particle emitting nuclei began in the early sixties [Bar63, Kar63], with the observation of β-delayed proton activity.

The further away from stability a nucleus lies, the less bound nucleons are, and therefore, the more common particle emission can become in the daughters of β-decaying nuclei. Unfortunately, analysis can be complicated in the medium to high mass region by the high density of excited states, which can have energy spacings smaller the resolution of the detection system [Poe89]. This results in a broad energy distribution from which information on the individuals states is sometimes impossible to reconstruct, and even if possible, requires reasonable statistics. Obtaining a large number of events from nuclei far from stability can be problematic if their production cross-sections are very low.

For heavy, proton-rich nuclei, Coulomb repulsion can become important as the Coulomb energy increases faster ($\propto Z^2$) than the nuclear volume energy ($\propto A$). This can lead to direct α emission, emitted to lower the Z of the unstable nucleus, competing with β-decay. α-emission is also very sensitive to the available decay energy ($t_{1/2,\alpha} \propto e^{E_\alpha^{-1/2}}$) [Yan96]. This leads to α-decay becoming the dominant decay mode for proton-rich nuclei with $Z > 82$, and quite common for $Z < 82$ nuclei in this region. For the higher mass proton emitters ($Z > 68$), it has been found that α-branches are almost always present, and provide the main source of competition. At lower Z, with a lower Coulomb energy, this competition is with β-decay.

For nuclei beyond the proton dripline, ground state proton decay becomes energetically possible, and as one goes further away from the dripline, half-lives for proton decay decrease rapidly, so that proton decay not only competes with, but dominates α or β decay. This turns out to be quite beneficial in the study of these nuclei. Since the proton already exists within the nucleus, there is no pre-formation factor involved in proton decay, unlike α-decay where four nucleons have to form the α particle in the skin of the nucleus before it can be emitted. The lack of this extra factor simplifies the theoretical description of proton decay, and means that structural information is obtained in a relatively straightforward manner when compared with analysing α-decay data in similar cases.

Protons, like other emitted nucleons, have to pass through a potential barrier to escape from, and therefore be emitted by, a nucleus. For protons and alpha's, this includes a Coulomb and centrifugal barrier. For uncharged neutrons, the centrifugal term is generally the main component of the barrier. This means that neutrons are generally less hindered than protons and alpha's, which have to tunnel through addition Coulombic potential, and therefore their decay rates can be much larger, leading to lifetimes of nuclei that are too short to be measured experimentally ($< 1\mu$s, faster than the flight-time through a mass separator). To be observed experimentally, the emission of a neutron from a nucleus beyond the neutron-dripline would have to be hindered by a large centrifugal barrier, but not slowed enough to give β-decay the opportunity to effectively compete with direct neutron-emission. Coupled with this is the fact that neutron-dripline is extremely difficult to reach (currently it has only been continuously mapped to Fluorine, Z=9 [Uts01]), lying much further away from stability than the proton drip-line. This is related to the Coulomb repulsion of proton-rich nuclei, decreasing the binding energy available to neutron-deficient nuclei until they become unbound. Experimentally, the low efficiency and poor energy resolution of most neutron detectors would limit the accuracy of the results from observing the directly emitted neutron, and therefore how useful they would be in verifying theory.

1.2 Studies along the Dripline

Proton-decay studies are useful in providing structural information on the emitting nucleus, due to the sensitivity of the proton decay-rate to the orbital angular momentum of the emitted proton. This is due to the lower mass of the proton when compared to an α-particle, increasing the centrifugal barrier (which is $\propto 1/\mu$, where μ is the reduced mass), and the slightly lower Z (1 instead of 2), decreasing the Coulomb barrier and thereby increasing the relative importance of the centrifugal barrier in hindering the emission of the proton. Proton decay is analysed by comparing experimental decay rates with those calculated for differing orbital angular momenta, at the same experimentally measured proton Q-value, Q_p. This has enabled the verification of shell-ordering in these nuclei, far from stability, as well as looking at the effects of deformation on decay-rates and studying mass systematics in this region. In all these cases, we can confront theory with experimental evidence gained further from stability than the usual experimental techniques available in this region.

Another related topic of interest in the study of proton dripline nuclei is energy generation and the nucleosynthesis of heavy elements in explosive stellar scenarios (e.g. X-ray bursters, supernovae type IA) [Käp98]. One of the possible reaction pathways that nuclei could take from H/He to the heavier elements we see within the universe (and on Earth) is along the proton dripline. The experimental measurement of various physical properties of these 'rp-process' nuclei being of great benefit in network reaction calculations for relative elemental abundances, the results of which are compared to astronomical observations of these explosive stellar events. Certain waiting-point nuclei are of particular interest, marking important points on the reaction pathway where the reaction has to wait for a relatively slow process such as β-decay to occur before the reaction may continue. An example of this situation is ^{80}Zr, where continued proton capture from this nucleus is hindered by the fact that ^{81}Nb is proton unbound [Res00].

The neutron dripline, mentioned earlier, has only been reached at very low Z, due to its remoteness. Yet, in this neutron-rich region, a number of discoveries have been made. The observation of a neutron-halo in Li^{11} by Tanihata *et al.* [Tan85] perhaps being one of the most striking. Evidence has been found for proton 'halo' systems, where a large matter radius associated with the weakly bound valence nucleons, most recently for the first excited state in ^{17}F [Lew99] and ^{23}Al [Cai02]. It should be noted, though, that the 'halo' effect for proton rich nuclei is less pronounced than for most neutron-halos. This can be explained by the fact that the Coulomb potential barrier experienced by the valence proton will tend to suppress any extended proton wavefuntions.

All known ground-state proton emitters are odd Z, since the unpaired proton is less bound, and therefore lies closer to stability and is more easily accessible. However, ever since it was predicted by Goldanskii [Gol60], $2p$ emission has always remained a possibility and a number of candidates have been studied. Two candidates were the light, unbound nuclei ^{6}Be [Boc92] and ^{12}O [Kry95] which both emit protons from their short-lived ground states ($t_{1/2} < 10^{-20}s$), but they emit the two protons sequentially, through an intermediate state. Another recent candidate was ^{17}Ne observed at MSU [Chr02], where correlated $2p$, or ^{2}He was not observed. ^{45}Fe was the next candidate for ground state $2p$ emission [Bla96] and recent experiments at GANIL [Gio02] and GSI [Pfü02] have been successful in showing that ^{45}Fe exhibits two proton radioactivity. The GANIL and GSI respectively measured total proton decay energies of 1.06(4) and 1.1(1) MeV, with a half-life of $t_{1/2} = 4.7^{+3.4}_{-1.4}$ ms and $t_{1/2} = 3.2^{+2.6}_{-1.0}$ ms which are mutually supporting, and provide the first indication of ground state two-proton emission. It should be noted that these experiments do not provide any clear indication of the details of the two proton decay process in this case (clustered or individual emission).

Low Z nuclei beyond the proton dripline have low Coulomb barriers, and therefore do not hinder the immediate emission of an unbound proton as effectively. This decreases their half-lives until they may only exist as short-lived resonances, decaying before they pass through a mass separator. They can, however, be studied via resonance reaction mechanisms, e.g. resonance scattering. Fragmentation facilities in particular have enabled the one proton-dripline to be completely mapped over a large swath of the Segré chart. To directly study ground state proton emitters, however, one must look at nuclei with half-lives in the range of 1μs-1s, to which current experimental capabilities are geared to handle. This has entailed looking at heavier elements ($Z > 50$).

As an aside, it should be mentioned that work continues on prompt proton decay from excited states, where proton emission competes directly with γ-decay. Some of the most recent examples of nuclei exhibiting this are $^{58,59}Cu$ [Rud98, Rud02].

1.3 Technical Developments

A number of methods have been used to access proton-dripline nuclei. Transfer reactions have been used to study the very lightest nuclei, due to the proximity of the proton dripline to stability at these low masses. Proton induced target spallation has been used at ISOLDE in CERN to study proton rich nuclei [Axe98], but in general, the ion release times (can be $> 1s$)

from the target are slow, and this method has been of limited use in proton decay studies. This is because most nuclei beyond the proton dripline have sub-100ms half-lives in the region of interest, where α-decay is prevalent. Projectile fragmentation has been used to study a wide range of nuclei along the proton-dripline. GANIL and NSCL have focused on nuclei with masses up to A=100 [Gio01], using TOF and dE information to identify the ions produced (see Chap. 3). Fragmentation is also utilised at GSI to study proton rich nuclei with a large range of masses.

Fusion evaporation, has been used to great effect in producing all of the proton emitters known to date. One of the characteristics of fusion-evaporation is the preferential population of high-spin states in the nuclei produced, which explains to some degree why approximately a third of the proton emitting states observed have been isomeric states. Developments in ion sources allowed new, neutron-deficient beam target combinations to be used, enabling the production of compound nuclei closer to the proton dripline. Unfortunately, compound nuclei produced via fusion evaporation preferentially evaporate protons over neutrons in this region. Therefore, care must be taken in choosing the excitation energy of the compound nucleus if proton rich nuclei beyond the proton dripline are to be produced with as large a cross-section as possible.

This leads on to a related topic, that of background reduction. Since proton-emitting nuclei are very exotic, they are generally produced with a low cross-section among a large number of more stable nuclei. Initial background reduction is generally through the use of mass separators where particle identification can occur through mass selection. The advantage of in-flight separation (as opposed to ISOL) is its speed, with flight-times of $\sim 1\mu$s, meaning that proton-emitters survive to reach the detector. The development of new segmented or strip detectors also assisted in background reduction. Unknown decays could be identified through correlations between implantation, the emission of the proton, and subsequent daughter α-decays, increasing the sensitivity of experiments to this rare decay mode. This will be discussed in more detail in later sections.

1.4 Proton Radioactivity Experiments

1.4.1 Early Experiments

As previously mentioned, β-delayed proton emission had been previously observed in 1963, with ^{25}Si [Bar63], and work in studying this decay mode has continued ever since. One of the candidate nuclei for βp emission in 1970 was ^{53m}Ni, for which a search was conducted at Harwell, in Oxford, using an ^{16}O beam on a ^{40}Ca target. ^{53m}Ni was expected to emit a delayed proton with an energy of over 2 MeV, however, the proton line observed was at 1.5 MeV [Jac70]. A possible candidate for this proton line was the direct emission of a proton from the high-spin ($J^{\pi} = 19/2^{-}$) isomer, ^{53m}Co. This was later confirmed by a second experiment at Berkeley [Cer70], with ^{53m}Co having a proton branch of $\approx 1.5\%$.

It should be noted that ^{53m}Co is the only case of direct proton emission from an isomeric state in a nucleus which is proton bound in its ground state. For some time, it was thought that looking for proton emission from isomeric states in similar nuclei would be fruitful, since these nuclei (being proton stable in the ground state) would lie closer to stability and hence be more readily accessible experimentally.

Unfortunately, it wasn't until 1981 that the next proton emitter was discovered by S. Hofmann at GSI using the UNILAC accelerator. ^{151}Lu was the first ground state proton emitter discovered via the $^{96}Ru(^{58}Ni,p2n)^{151}Lu$ channel [Hof81a]. The reaction products entered the SHIP velocity filter [Mun79] to separate out the beam and fast reaction products, with a transmission efficiency of 2-40% depending on the reaction channel. After a separation time of $\sim 1\mu$s the surviving reaction residues where then implanted within an array of seven position sensitive detectors. The position sensitivity of the detectors allowed correlations to be made between implantation and subsequent particle emission as the implanted ion decayed, thus allowing implant ion identification to made with some confidence. Sensitivity to short half-lives was increased by pulsing the beam with a Duty Factor of 0.25 (in this case, 5 ms on, 15 ms off). Longer correlations could be made by blocking the residues upstream of the detector for up to 300 ms.

The short separation time of in-flight mass separators marked a great improved in sensitivity to short half-lives, overcoming the limitations of systems with chemically selective ion transport systems, these having been used in previous searches for proton emitters, for example at ISOLDE [D'Au78], the only exception being ^{147}Tm, which was observed at the on-line mass separator at GSI [Kle82]. A tantalum foil was used to catch the evaporation residues, the ion release times from the foil into the mass separator limiting the search to nuclei with half-lives $>$ 100ms.

TUM (Technische Universität München) took the opposite approach to the on-line mass separator method, with its high-efficiency and lack of sensitivity to longer half-lives. Instead, a fast catcher detection system developed for γ-spectroscopy of fast isomers was used to look for proton radioactivity from the residues from the reaction $^{58}Ni +^{54} Fe$ and ^{58}Ni, which were stopped in a foil. The decays were measured in an annular gas-filled detector system designed for α-spectroscopy, and the proton-emitters ^{109}I and ^{113}Cs were discovered [Fae84, Gil87]. Unfortunately, while sensitive to very fast decays ($> 10ns$), the efficiency and lack of selectivity in residues meant that it had a low sensitivity to other proton emitters with lower cross-sections.

1.4.2 Daresbury Experiments

It was in the UK where the next steps where being made in the search for new proton emitters. A new Double-side Silicon Strip Detector (DSSD) was developed by the Edinburgh group to study proton emitting isotopes [Sel92]. This was successfully used at the Daresbury Recoil Mass Separator (RMS) to study a large number of proton rich isotopes, including proton emitters. The 2-d position sensitive silicon surface barrier detector [Woo89] used in previous experiments at the RMS had an overload recovery problem where the position signal remained 'dead' for 200 μs following saturation by an implantation event. The DSSD did not have this deficiency (associated with the resistive layer of the barrier detector), its overload recovery taking $< 10\mu$s, dictated by the amplifiers used. The DSSD also had improved energy and positional resolution, the latter useful in improving implant-decay correlations, increasing the sensitivity to weak decays. Its use at Daresbury marked the introduction of double-sided silicon strip detectors in Nuclear Physics. The DSSD is described in greater detail in Chap. 3.

The RMS (see Fig. 1.2) contained Wein filters for beam rejection and

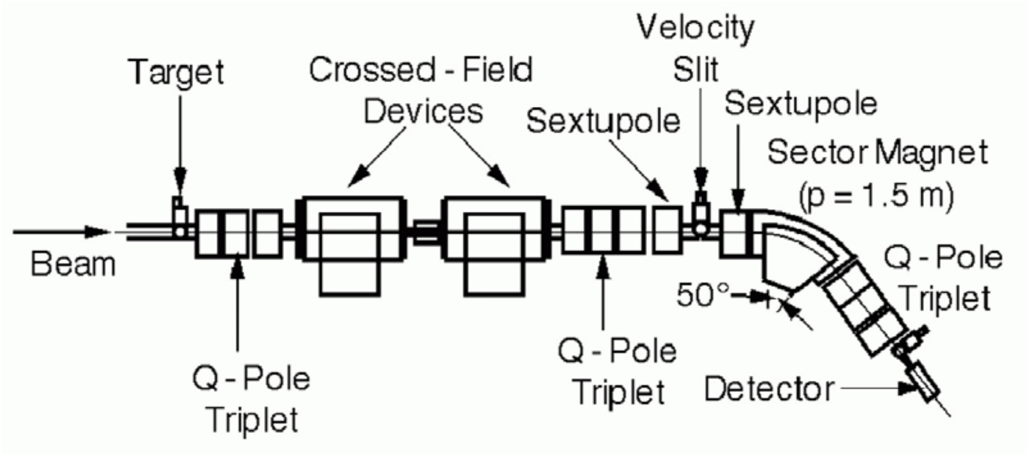

Figure 1.2: *The Daresbury Recoil Mass Separator (RMS).*

velocity selection. These were followed by a magnetic dipole to disperse the evaporation residues horizontally according to their mass to charge ratios. The position of the recoil ion in the DSSD (placed at the focal plane) would indicate their A/Q. This allowed mass assignments of recoils to be made directly, as opposed to using excitation functions. Initial experiments using the new set-up involved remeasuring the proton emitters discovered at GSI and Munich, remeasuring the decays of ^{109}I or ^{147}Tm, as well as studying ^{150}Lu [Sel93].

The Edinburgh group at Daresbury then went into production mode, discovering a large number of proton emitting states using implant-decay and decay-decay correlations [Pag92, Pag94, Liv93].

In 1993, the Nuclear Structure Facility at Daresbury, including the RMS and Tandem accelerator, were closed, bringing to an end the Edinburgh proton programme in the UK. However, the techniques developed there would later be used successfully at Argonne National Laboratory (ANL).

1.4.3 Argonne Experiments

The Edinburgh group re-established its proton radioactivity program at ANL in the US in 1993. Experiments were undertaken by using the Fragment Mass Analyser (FMA) in conjunction with a detector set-up at the focal plane which included a DSSD (for details, see Chap. 3). One of the first experiments involved the search for proton radioactivity using ^{78}Kr on ^{96}Ru, and protons from ^{171}Au and $^{165,166,167}Ir$ were observed [Dav97]. In fact, major progress has continued, with ^{155}Ta, ^{157}Ta, ^{161}Re, ^{177}Tl all being observed [Uus99, Irv97, Pol99].

A number of results merit special attention. The first example of proton radioactivity for $Z > 82$ was discovered in ^{185m}Bi [Dav96, Pol01]. One of the main experimental difficulties in accessing this region via fusion-evaporation is competition with fission. This was overcome by using a 'cold' reaction; the compound nucleus $^{187}Po^{*}$ having an excitation energy of less than 30 MeV. As of yet, this is the only heavy ($Z > 82$) proton emitter known.

Another set of exciting results were the discovery of the proton emitters, ^{131}Eu and ^{141}Ho [Dav98], lying in a region where large prolate deformation is predicted by Möller *et al.* [Mol97]. Comparisons of the experimental half-lives with those calculated using barrier penetration codes assuming spherical nuclei did not agree. This supported the prediction that these nuclei were heavily deformed, and spurred theoretical interest in the subject (see Chap.2).

These results were then followed by the discovery of fine-structure in the proton decay of ^{131}Eu [Son99]. This is when the nucleus can decay

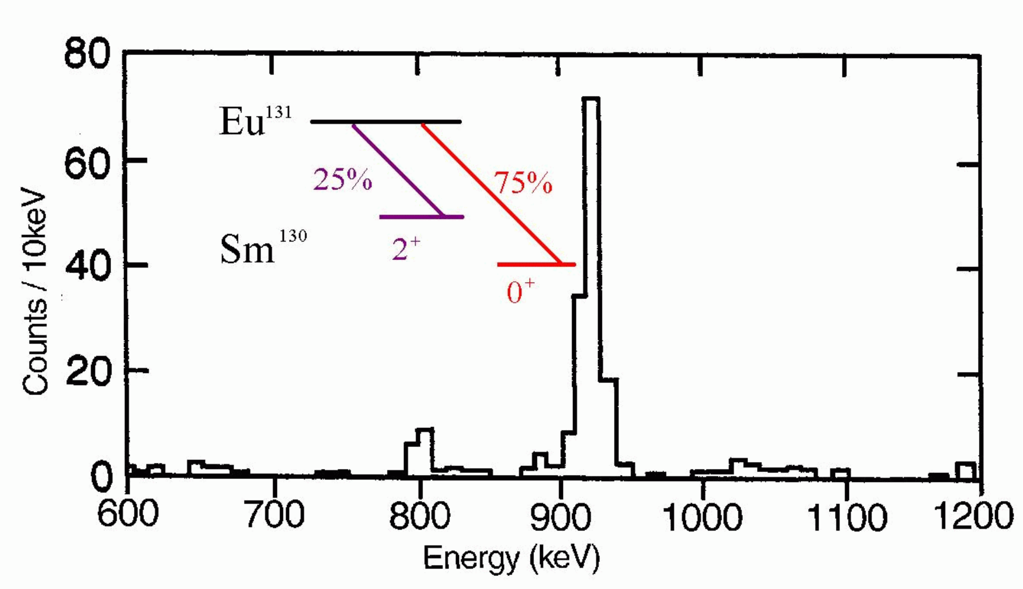

Figure 1.3: *Fine structure in the decay of* ^{131}Eu*. The spectrum shows the decays occurring within 100 ms of an A=131 ion being implanted within a 'pixel' in the DSSD.*

via proton emission to more than one state in the daughter nucleus, in this case from the ground state of ^{131}Eu to the ground state of ^{130}Sm, with a 0.24(5) branch to the 2^+ first excited state (see Fig. 1.3). Due to the extreme sensitivity of this fine-structure branching ratio to the different angular momentum components in the parent nuclear wavefunction, one possesses another probe into the structure of this deformed nucleus. An ancillary benefit was it provided a direct measurement of the 2^+ energy of the daughter, giving us a handle on the deformation by utilising Grodzins' formula [Gro62].

With the arrival of Gammasphere at ANL, an opportunity was taken to study deformed proton emitters using γ-spectroscopy. Seweryniak *et al.* [Sew01a, Sew01b], performed a recoil-decay tagging (RDT) experiment on ^{131}Eu and ^{141}Ho, providing confirmation of their deformed natures. RDT involves the study of the prompt γ-rays from a nucleus when it is formed in the target. These γ-rays are tagged by correlating them with the unique particle decays (proton and α) that the desired nucleus undergoes when it has been implanted in the DSSD.

Experiments performed at ANL in 2000 form the core of this thesis, and will be discussed later.

1.4.4 Recent Progress

During the nineties the Edinburgh group, whether at Daresbury or Argonne, had not been the only group performing proton radioactivity experiments. Berkeley, where the first known direct proton emitter, ^{53m}Co, was confirmed [Cer70], observed another proton emitting isotope, ^{105}Sb in 1994 [Tig94].

This was the lowest Z ground state proton emitter known, and interestingly from a structural perspective, possessing a valence proton out of the Z=50 closed shell. It was observed using a He-jet system to transport and deposit reaction products on to a tape, the tape being used to reduce background from long-lived activity. The protons were detected using an array of low energy, gas-ΔE, gas-ΔE and Si-E triple telescopes. A line at 478(15) keV was observed in a large β background, and attributed to a small proton branch ($\sim 1\%$).

Proton emitters have been successfully observed at another lab in the US, Oak Ridge National Laboratory (ORNL). Initially in conjunction with Edinburgh, and using some Edinburgh electronics including a DSSD setup, the new proton emitting isotopes, ^{140}Ho and ^{145}Tm were observed [Ryk99, Bat98].

ORNL has specialised in studying very fast decays, all of the states discovered there having $t_{1/2} < 50\mu$s, including ^{145}Tm ($t_{1/2} = 3.5(10)$ μs), with the shortest half-life observed for a proton emitter. This emphasis on looking for the very fast decays has led ORNL to use digital signal-processing techniques [Mom00], originally designed for γ-spectroscopy, in their proton decay studies. This involved digitally recording the implantation pulse for 10μs after the implantation occurred. By recording the whole pulse, they were able to observe proton events which occurred within this interval when the amplifier would still be recovering, these events lying on top of the large implantation signal. This method has been used to observe evidence for proton fine structure in ^{145}Tm [Ryk01].

In 1999, INFN Legnero in Italy announced its successful search for the proton emitter ^{117}La, their results can be found in [Sor01]. Since this is related to work done for this thesis, details will be presented later (see Chap. 4).

Jyväskylä (JYJL) has been upgrading the capabilities of the setup at the gas-filled spectrometer, RITU. In particular, the detector setup, with a gas-filled veto detector in front of a position accessible Si detector has meant they are able to increase their sensitivity to proton emitters. In 2000, they observed the new proton emitting isotope, ^{164m}Ir [Ket01]. This result was released simultaneously with a successful experimental run in Argonne where ^{164m}Ir was also observed. Since the result at ANL forms part of this thesis, more details are presented later.

Chapter 2

Theory

Proton emission is a quantum tunnelling phenomenon. It involves the tunnelling of an unbound proton through a potential barrier out of the nucleus, resulting in a relatively more stable daughter nucleus which will proceed to decay down to stability via α or β-decay. The decay rate of the proton emitting nucleus is related to the energy possessed by the unbound nucleus relative to the height of the potential barrier, the larger the energy, the faster the decay. For a proton decay branch to be observable, the proton has to be unbound, with an energy large enough for the decay to be competitive with β, and in some cases α, decay. But if the decay energy is too large, the nucleus decays before it can be experimentally observed ($t < 1$ μs).

In this chapter, a general introduction on elements of nuclear theory will be followed by a section on nuclear mass models and then details on proton decay calculations for spherical and deformed proton emitters. The last section will be on the topic of proton spectroscopic factors.

2.1 Energetics

As mentioned previously, for proton decay to be energetically allowed, it must possess a positive Q_p:

$$Q_p = (M_{Z+1} - M_Z - m_H)c^2 > 0 \tag{2.1}$$

where M are the atomic masses of parent and daughter and m_H is the mass of the hydrogen atom. This is equivalent to:

$$Q_p = B_Z - B_{Z+1} > 0 \tag{2.2}$$

where the binding energy is defined as:

$$B_{Z,N} = (ZM_H + NM_n - M_{Z,N})c^2 \tag{2.3}$$

which is the energy required to break up a nucleus consisting of Z protons and N neutrons into individual nucleons. One should also note that momentum must be conserved in the decay process which means that the kinetic energy available must be divided between the products (in this case a proton and the daughter nucleus) inversely proportional to their masses, which results in the proton having an energy:

$$E_p = \frac{M_Z}{M_Z + m_p} \times Q_p \tag{2.4}$$

with the remaining energy invested in the recoiling daughter nucleus. The energy measured in the laboratory is slightly different to the energy released when the proton was initially emitted from the nucleus. This is because the proton loses some energy when moving through the electrons surrounding the nucleus, this energy being needed to balance the differing atomic binding energies of the parent and daughter atoms. Theoretical analysis of proton decay requires the $Q_{p,nuc}$, which includes a screening correction, E_{sc}. This correction can be obtained from Huang and Mark [Hua76] and is of the order of 10 keV for most proton emitters. Therefore the energy used in the theoretical study of proton emission is:

$$Q_{p,nuc} = Q_p + E_{sc} = \frac{M_Z + m_p}{M_Z} \times E_p + E_{sc} \tag{2.5}$$

2.2 Spherical Shell Model

During the 1940's, experimental evidence begin to indicate that nuclei had discontinuities in physical parameters, such as the energies of 2^+ first excited states and nucleon separation energies, for nuclei containing certain 'magic' numbers of nucleons. For both protons and neutrons, some of these magic numbers are 2, 8, 20, 50 and 82. The shell model had been successfully used to understand atomic electrons which also showed similar discontinuities in behaviour, and was therefore proposed as a model to understand nuclei.

The main assumption of the shell model is that each nucleon moves independently within a central potential which is the average of the interactions between all the nucleons forming the nucleus. The chosen average potential is then used to solve the time-independent Schrödinger equation:

$$\left(\frac{-\hbar^2}{2\mu} \bigtriangledown^2 + V(r) \right) \phi_i(\underline{\mathbf{r}}) = \epsilon_i \phi_i(\underline{\mathbf{r}}) \tag{2.6}$$

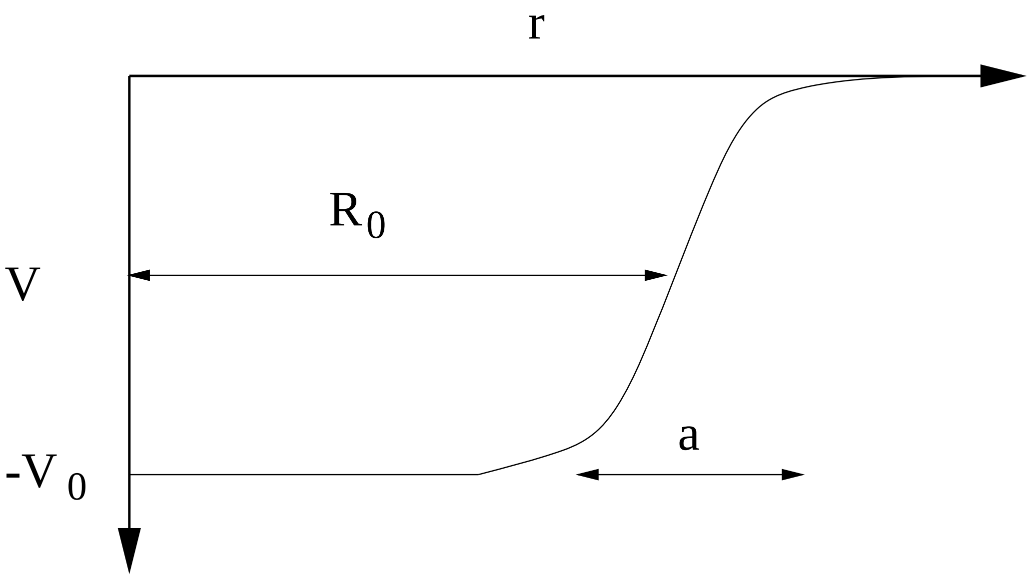

Figure 2.1: *The Woods-Saxon Potential.*

Different forms of the potential yield different energy levels, or shells, and hence different magic numbers - points where there is a large gap between energy levels. These shells, or orbits, are filled according to the Pauli Exclusion Principle. Since the energy levels are filled up to those of the valence nucleons, nuclei will generally stay within their orbital since, to be promoted internally by nucleon-nucleon collisions, they need enough energy to reach a free valence orbital, the lower energy orbitals already occupied and hence forbidden. Therefore, the exclusion principle ensures that internal nucleon collisions are not as common as one might expect when considering the large size of nucleons and their close proximity due to the high density in the nucleus.

Various potentials were used in an attempt to reproduce the magic shell numbers seen experimentally. The shapes postulated included infinite square well, finite square well and harmonic oscillator, though none were successful. Using a more realistic potential was then postulated, one which was not infinitely deep but saturated within the core as well as having a diffuse edge. This turns out to be similar to the matter distribution of the nucleus due to the short-range nature of the nuclear force. The Woods-Saxon potential [Woo54], shown in Fig. 2.1 is an example of such a potential, taking the form:

$$V_{nuc} = -V_{N0} f(r) \tag{2.7}$$

$$f(r) = \left[1 + exp\left(\frac{r - R_0}{a}\right)\right]^{-1} \tag{2.8}$$

where $R_0 = R_N A^{1/3}$ is the nuclear radius and a the surface diffuseness. This produces the energy level scheme seen on the left in Fig. 2.2. However, even this does not yield the observed magic number shell gaps. Therefore, Mayer and Jensen *et al.* [May49, Hax49] added a spin-orbit term to the potential, which, when included, reproduced the correct magic numbers while breaking the orbital angular momentum (l) degeneracy of the level. The general form of the potential then becomes:

$$V(r) = V_{nuc}(r) + V_{so}(r) l.s \tag{2.9}$$

$$l.s = \begin{cases} l/2 & \textbf{for } j = l + 1/2 \\ -(l+1)/2 & \textbf{for } j = l - 1/2 (l > 0) \end{cases} \tag{2.10}$$

where V_{nuc} is the nuclear potential, such as a Woods-Saxon potential, and V_{so} is:

$$V_{so}(r) = V_{so0}\lambda_{\pi}^{2}\frac{1}{r}\frac{d}{dr}f(r) \tag{2.11}$$

where λ_{π} is the pion Compton wavelength $= \hbar/m_{\pi}c \approx \sqrt{2}fm$, and $f(r)$ is the form factor, see equation (2.8).

Each l orbital now splits into two, with values of $j = l \pm 1/2$ for $l > 0$. By making the V_{so} negative, energy levels with $j = l + 1/2$ were actually pushed down in energy. This was done to reproduce the shell gaps experimentally observed. The shell model has done well in describing nuclei in the proximity of closed shells and the line of stability.

2.3 Nilsson Model

It had been noticed that certain nuclei found away from magic number shell closures exhibited collective modes of rotational excitation. This indicated, among other things, that nuclei had appreciable quadrupole moments, and therefore could not be well described by the standard shell model which assumed a spherically symmetric nuclear shape. While macroscopic models for nuclei exhibiting rotational excitations were proposed, it wasn't until 1955 that a self-consistent microscopic model was introduced by Nilsson and Mottelson in 1955 [Mot55]. This consisted of a shell model for an ellipsoidal nucleus with one axis of symmetry, using a deformed harmonic oscillator potential. An appropriate Hamiltonian for a nucleon in a deformed

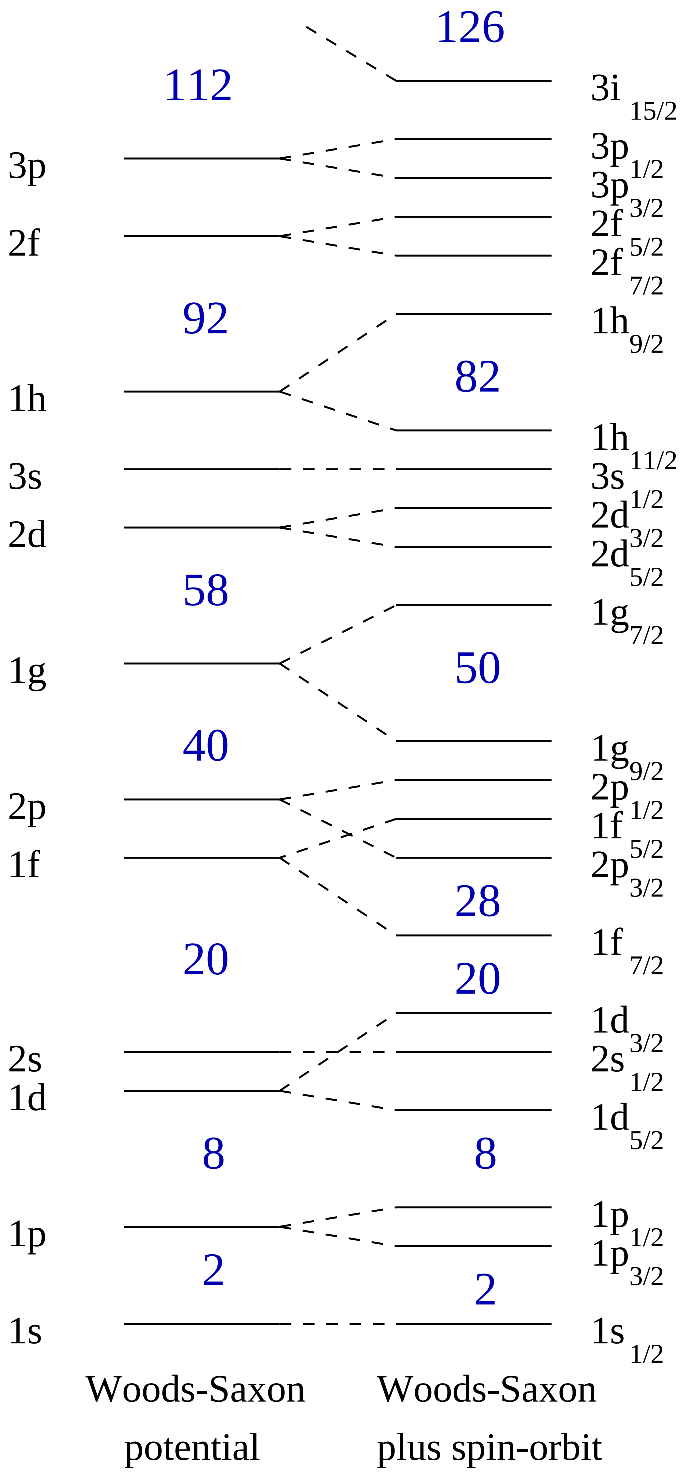

Figure 2.2: *Schematic of the level scheme obtained using a Wood-Saxon potential, and Wood-Saxon potential with a spin-orbit term. The spin-orbit terms breaks the $2j+1$ degeneracy of the levels from the simple potential on the left, to $(2j+1)/2$ for the shell levels obtained on the right. The magic numbers are shown in blue.*

potential around the symmetry axis, z, is:

$$H = -\frac{\hbar^2}{2m}\nabla^2 + \frac{1}{2}m\omega_0^2\mathbf{r^2} - \frac{4}{3}\sqrt{\frac{\pi}{5}}\delta m\omega_0^2\mathbf{r^2}\mathbf{Y_{20}} + C\mathbf{1}.\mathbf{s} + D\mathbf{l}^2 \qquad (2.12)$$

where ω_0 is the oscillator frequency ($\hbar\omega_0 = 41A^{-1/3}$), C and D are Clebsch-Godon and D-matrix coefficients, and $\mathbf{Y_{20}}$ is the spherical harmonic oscillator potential. The deformation parameter is $\delta = \Delta R/R_{rms}$, where R_{rms} is the root mean square nuclear radius and ΔR is the difference of between the semi-minor and semi-major axes of the nuclear ellipsoid. This can then be related to other deformation parameters via the expressions:

$$\epsilon_2 = \delta + \frac{1}{6}\delta^2 + \frac{5}{18}\delta^3 + \frac{37}{216}\delta^4 + \ldots$$

$$\beta_2 = \sqrt{\pi/5}\left(\frac{4}{3}\epsilon_2 + \frac{4}{9}\epsilon_2^2 + \frac{4}{27}\epsilon_2^3 + \frac{4}{81}\epsilon_2^4 + \ldots\right) \simeq \frac{2\sqrt{5/4\pi}}{3}\delta$$

One of the main consequences of the deformed potential is to break the $2j + 1$ degeneracy of the spherical levels into $j + 1/2$ sub-shells, each with a degeneracy of two. For a finite deformation, only the parity and Ω, the projection of j along the symmetry axis, are good quantum numbers. However, for an infinite deformation, N, n_z and Λ can be used to characterise the nucleon wavefunction, where N is the total oscillator shell number, n_z the number of nodes in the z direction and Λ is the projection of l along the symmetry axis. Therefore, Nilsson orbitals are labelled by $\Omega^\pi(Nn_z\Lambda)$, where the numbers in parentheses are the asymptotic quantum numbers.

An example of a Nilsson level scheme, calculated using a Woods-Saxon potential as opposed to a harmonic oscillator, can be seen in Fig. 2.3. The

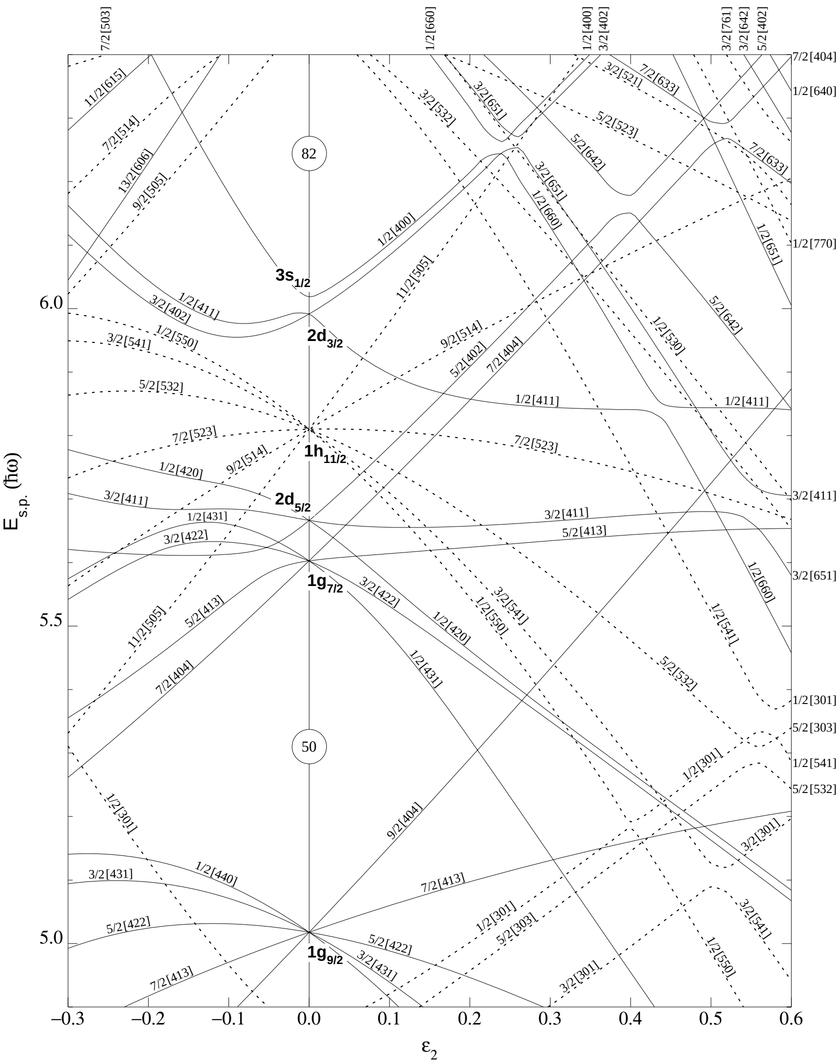

Figure 2.3: *Nilsson level diagram for protons (*$50 < Z < 82$*), calculated as described by Bengtsson and Ragnarsson [Ben85], as a function of the deformation parameter* ϵ_2 *with* $\epsilon_4 = \epsilon_2^2/6$ *and using a deformed Woods-Saxon potential.*

orbitals are populated by protons and neutrons separately, starting at the lowest energy, as normal, and filled up until one reaches the outer most nucleons at the Fermi level. The ground state deformation is determined by minimising the summed single particle energies with respect to the deformation.

By experimentally measuring nuclear quadrupole deformation, it has been found that most known nuclei are prolate ($\beta_2 > 0$) which is cylindrical. The alternative is oblate ($\beta_2 < 0$) where the nucleus is more flattened, like a pancake. A possible explanation for this preference is that while downward sloping energy levels are found on both sides of the Nilsson diagram, for oblate deformation, the lowest energy states are the ones with the largest Ω, while for prolate levels, it is the lowest Ω states which are downward sloping. We can then note that within each major shell, low Ω are much more common relative to the highest Ω states, since only the largest j spherical states can yield large Ω Nilsson states. Therefore, while large Ω oblate states are isolated, there may be a number of prolate, small Ω states from different j shells in close proximity [Cas00].

2.4 Mass Models

The first attempt to fit known atomic masses was made by von Weizsäcker [Wei35] using a semi-empirical liquid drop model, which was later simplified by Bethe and Bacher [Bet36] to give a function dependent on Z and N, with five adjustable parameters. While nuclear theory has advanced, with more models proposed, they all contain adjustable parameters which are fitted against known data. Data from proton radioactivity experiments have been incorporated into recent mass models. Generally, models with more parameters give a better fit to known data, though not necessarily beyond it.

Mass models have been useful in the experimental search for proton emitting nuclei. As will be illustrated, proton emission is very sensitive to the decay energy available, and so identification of possible candidates is influenced by proton separation energy predictions. As more examples of proton emission have been observed, this situation has been partially reversed, and mass model predictions can be tested against known proton separation values, as will be shown in Chap. 4. It should be noted that proton decay studies have led to indirect mass excess measurements of nuclei beyond the reach of current mass measurement techniques, using α and proton decay chains anchored on an isotope of known mass [Dav97]. Other features of certain mass models that are of use in the study of proton emitters are deformation and energy level predictions.

A widely used mass table, that will not be discussed in detail here, is by Audi and Wapstra [Aud95]. It incorporates experimentally known masses and uses systematics to extrapolate the masses for selected isotopes of unknown mass. In its current iteration this mass table does not provide extrapolated predictions on a number of known and candidate proton-emitters, these isotopes lying too far from nuclei of known mass.

Three different mass models will now be discussed, as examples of mass models that are still in use today and are based on shell model calculations, a macroscopic-microscopic approach and a purely microscopic calculation.

2.4.1 Liran-Zeldes

While this may be a relatively old model, presented in 1976 [Lir76], it has been quite successful, as will be shown later, and is still used today. It is a shell model calculation using a strong pairing-pairing approximation, where the maximum number of $J = 0$ and $T = 0$ nucleon pairs is formed in the ground state. One and two nucleon excitation within shells and between neighbouring sub-shells, and to a lesser extent between major shells, complicates this picture, and gives rise to deformation and core excitation respectively. The ground state energy of a nucleus is then written as:

$$E(Z, N) = E_{pair}(Z, N) + E_{def}(Z, N) + E_{coul}(Z, N) \tag{2.13}$$

where E_{pair} is the contribution from the nucleon pairs, E_{def} accounts for configuration mixing and E_{coul} is the proton Coulomb energy.

Regions where the valence nucleons occupy the same shell, and those along which they fill different major shells, are differentiated, with the terms E_{pair} and E_{def} having different forms for each region. Effective two-body interactions are used to calculate the binding energy of the core, the core with valence nucleons and between the valence nucleons. The parameters used in these expressions are adjusted by least-squares fitting to experimental data within each shell region. These shell regions are bounded by Z,N=2,8,20,28,50,82; N=126,184 and Z=114, where the magic numbers N=184 and Z=114 are based on theoretical calculations [Bei75]. Note that no explicit account is taken of sub-shells, these effects are assumed to express themselves in oscillatory terms in E_{def}. Initially, parameters are obtained for each region individually, and checked to ensure they are statistically significant, as well as physically plausible according to the properties of the effective nuclear interaction. This is then repeated, adjusting parameters for adjacent regions simultaneously to ensure continuity between the regions, requiring that masses on the boundaries are the same.

A total of 178 coefficients are present in this model, whose value are adjusted by fitting to 1818 known isotopes in the various shell regions. A comparison of these predictions with 268 subsequently measured nuclear masses results in an RMS deviation of 590 keV.

2.4.2 Möller-Nix

This is a macroscopic-microscopic model which has gone through a number of iterations, the latest form of which is found in [Mol95, Mol97]. Here, the total binding energy is:

$$E(Z, N, \epsilon) = E_{mac}(Z, N, \epsilon) + E_{mic(Z,N,\epsilon)} \tag{2.14}$$

where E_{mac} is a macroscopic term which varies smoothly with N, Z and a deformation parameter ϵ, and E_{mic} which includes shell-pairing corrections which are dependent on single-particle effects. One of the strengths of this model is that it explicitly includes deformation, the deformations for the various isotopes calculated by solving a Schödinger equation for a deformed oscillator potential with a modified version of a three-quadratic surface parametrisation code [Mol74], the results of which are shown in Fig. 2.4. The mass of each nucleon is then obtained for the specific deformation calculated. The deformation predictions of Möller *et el.* have been useful in providing β_2 values for use in calculations on deformed proton emitters, where little other information may initially be available.

The macroscopic energy is from the Finite-Range Droplet Model (FRDM), based on the droplet model [Mye77], with a Yukawa-plus-exponential model for the surface energy to account for the finite range of the nuclear force. An empirical exponential term was also added to account for compressibility effects, important for $A < 120$ nuclei. The microscopic energy is evaluated using a set of Nilsson single-particle levels. Shell corrections are then obtained by comparing the calculated single-particle levels with those obtained via the Strutinsky method, originally envisaged to solve an infinite single-particle potential well [Str67, Str68]. The pairing term is obtained using the Lipkin-Nogami version of the BCS model [Lip60, Nog64].

Having calculated the single-particle energies for use in the mass model, the Möller-Nix model also provides level diagrams for nuclei representative of various regions, as well as explicit angular momentum assignments for the odd nucleons in all the nuclei present in the mass table, which can be provide assistance in assigning ground state spins for these nuclei, providing initial candidate states for use with proton decay calculations. Other physical parameters are also explicitly calculated in this mass table, such as predicted α and β partial half-lives.

This model contains a total of 38 parameters, only 16 of which are obtained using a least-squares fit to known mass data. The other parameters are obtained from other data not directly related to mass, such as nuclear radii. A total of 8979 nuclear masses, and related properties, are predicted, using a set of 1654 nuclei of known mass for parametrisation. The RMS error is 669 keV, but does seem to perform better for heavier nuclei ($N > 64$).

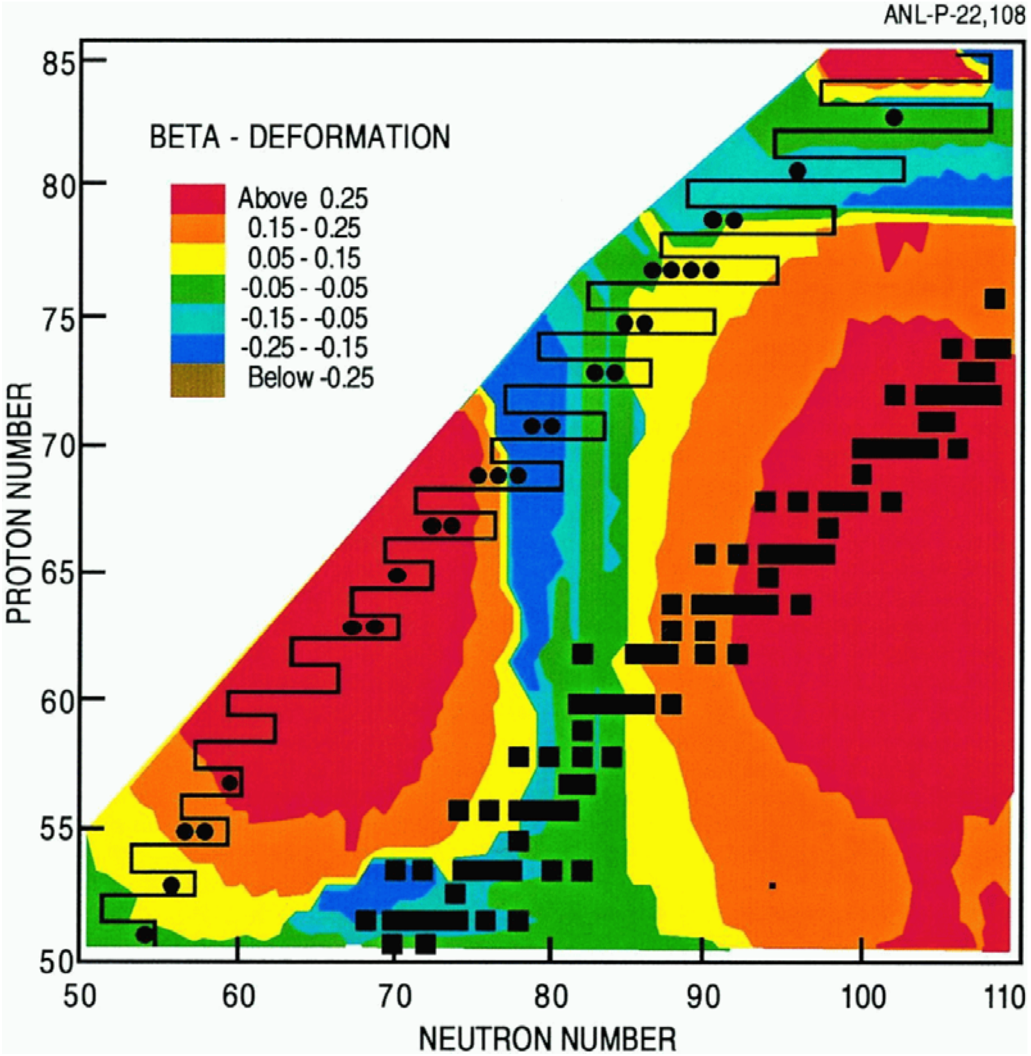

Figure 2.4: *Plot of β_2 deformation versus Z and N, calculated by Möller* et al. *[Mol97]. The black squares represent stable nuclei, and the line represents the Liran-Zeldes predicted position of the proton dripline [Lir76]. The circles represent known proton emitters.*

2.4.3 Aboussir-Pearson

This is the first mass model based on a purely microscopic basis, and details can be found in [Abo95] and references contained therein. It uses the Extended Thomas-Fermi plus Strutinsky Integral method (ETFSI) which is an approximation to the Hartree-Fock method (HF). The HF method cannot be used itself since it is computationally too taxing to calculate masses for a large number of nuclei in a reasonable length of time. As an aside, one can mention that more recently, full HFB and relativistic mean field mass calculations have been made, but only for a limited number of even-even, spherical nuclei [Pat99]. The ETFSI method utilises a Skyrme force with a BCS pairing correction, and is a semi-classical approximation of the HF method. This approximation effectively smoothes out the fluctuations which would give rise to shell effects, and therefore shell corrections are introduced using an integral form of the Strutinsky method. It should be noted that while there are some similarities with Möller *et al.*, both using SI shell-corrections between this method, in terms of the smoothed ETF term with is similar to [Mol97], the both term contains the same, microscopic, Skyrme force. This provides an extra degree of coherence between the two parts, not found in macroscopic-microscopic models where the two parts are not connected by a microscopic force, for example, the droplet model in Möller-Nix. The total internal energy calculated is then minimised with respect to the deformation parameters.

One of the features of this model is that it only uses 8 parameters which are fitted to mass data from 1492 nuclei, and predicts the mass of over 700 nuclei. With a RMS error of 736 keV, this model provides a reasonable fit considering how few free parameters it contains relative to the other models shown here.

2.5 Spherical Proton Emitters

While, in principle, proton decay theory is analogous to α-decay theory, both being the decay of a nucleus via emission of a particle through a potential barrier, a number of differences remain. Since the proton is lighter and has a lower Z than an α-particle, it experiences a larger centrifugal barrier, and lower Coulomb barrier. This results in proton decay rates being much more sensitive to the orbital angular momentum of the emitted proton, and hence the state from which it was emitted. Also, since the proton is a single fermion, as opposed to an α composed of an even number of fermions, the proton will have a spin of 1/2, and therefore a spin-orbit term will be included in the potential.

2.5.1 Semi-Classical Decay Rate Calculations

Proton emission initially sparked interest more than 40 years ago, with predictions of proton unbound nuclei by Goldansky, as well as experimental searches for nuclei exhibiting this decay mode [Gol60, Gol66]. However, modern interest in theoretical calculations of proton decay rates was spurred by the discoveries made at GSI in the 1980's, of near-spherical proton emitters such as ^{147}Tm and ^{151}Lu. The need to theoretically analyse these results led Hofmann [Hof82a, Hof89a] to use a method analogous to that used in α-decay theory [Man64]. In this method, the proton, at $Q_{p,nuc}$, tunnels through a potential, shown in Fig. 2.5, which is:

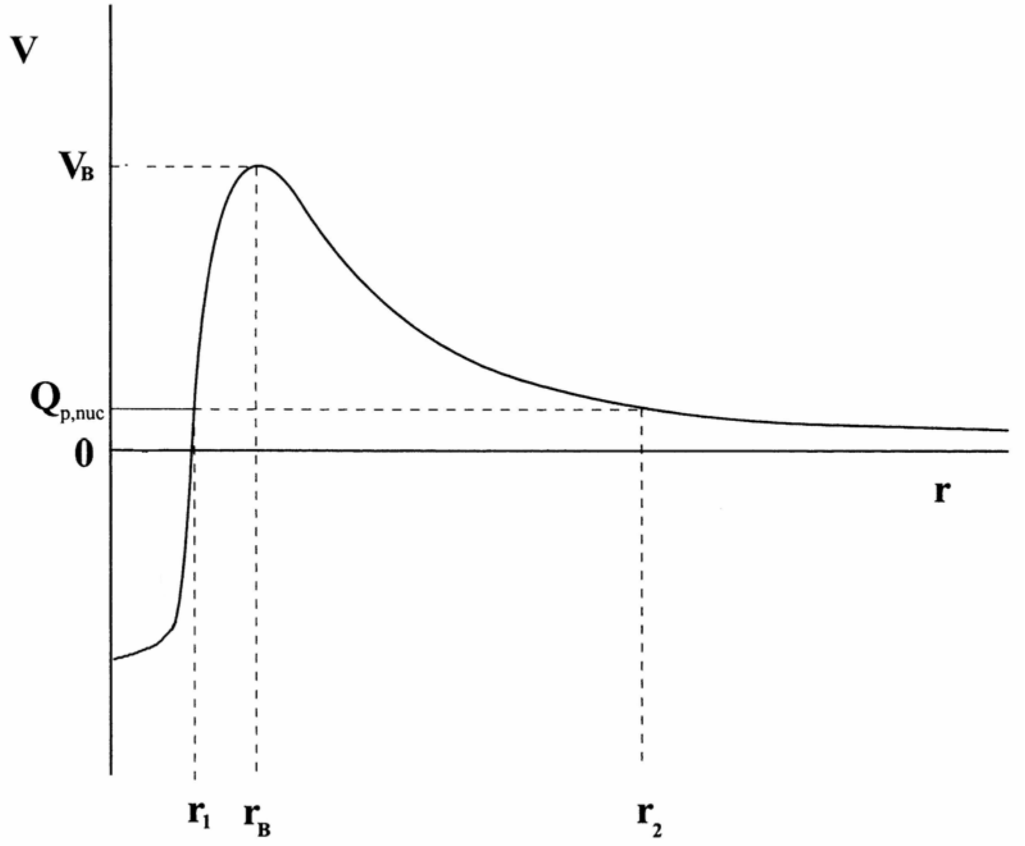

Figure 2.5: *Potential experienced by an unbound proton with the nucleus.*

$$V(r) = V_{nuc}(r) + V_{so}(r) + V_C(r) + V_l(r) \tag{2.15}$$

the sum of the nuclear, spin-orbit, Coulomb and centrifugal potentials. For details of the potential, see Sec. 2.5.2. A semi-classical decay constant is then calculated, as described by Gamow [Gam28]. From this, the half-life can be obtained:

$$\lambda = ln2/t_{1/2} = P\nu \tag{2.16}$$

where P is the transmission coefficient and ν is the frequency factor of the proton within the potential well, a measure of how often it impinges the potential barrier. An expression for the frequency factor is:

$$\nu = \frac{\sqrt{2}\pi^2\hbar^2}{\mu^{3/2}R_C^3(zZe^2/R_C - Q_{p,nuc})^{3/2}} \tag{2.17}$$

where μ is the reduced mass of the system, R_C is the Coulomb radius ($R_C = 1.21fm \times A^{1/3}$) and z, Z are the proton and daughter nucleus charge respectively. ($\nu \sim 1.2 \times 10^{27}$ Hz for the proton decay of ^{170m}Au).

The WKB (Wentzel, Kramers, Brillouin) approximation is then implemented, which assumes that the potential varies slowly with respect to the radial variation in the proton wavefunction. The transmission coefficient is then:

$$P = e^{-2G} \tag{2.18}$$

where G is the Gamow factor:

$$G = \sqrt{2\mu/\hbar^2} \int_{r_1}^{r_2} \sqrt{(V(r) - Q_{p,nuc})}\, dr \tag{2.19}$$

is the integral over the classically forbidden region of the potential, between the turning points r_1 and r_2.

This exponential dependence of P on the proton Q_p is clearly shown in Fig. 2.6, with a change in energy of 1.5 MeV for the $h_{11/2}$ line resulting in the half-life changing by over 22 orders of magnitude. One can also see the importance of l, due to the variation of the centrifugal barrier, $V_l(r)$. In this example, calculated for ^{155}Ta, changing the angular momentum of the emitted proton by 5, changes the proton half-life by over 4 orders of magnitude. The experimental half-life, can be compared to half-lives for protons emitted with different l's, calculated at the observed decay energy. In this case, one sees that the proton seems to have been emitted from a $h_{11/2}$ configuration, for details see [Uus99].

One other point illustrated in Fig. 2.6 is the Q-value window which in this case is approximately between 1.2 and 1.8 MeV. Only ^{155}Ta protons with energies within this range would be emitted with a half-life which would make proton decay from this nucleus feasible, or experimentally detectable. Below 1 μs, the nucleus decays in flight in the mass separator before reaching the detector, and if the half-life is more than a second or so, it would not be competitive with other decay mode such as β-decay. The elements with lower Z have an even smaller Q-value window in general due to the smaller Coulomb barrier.

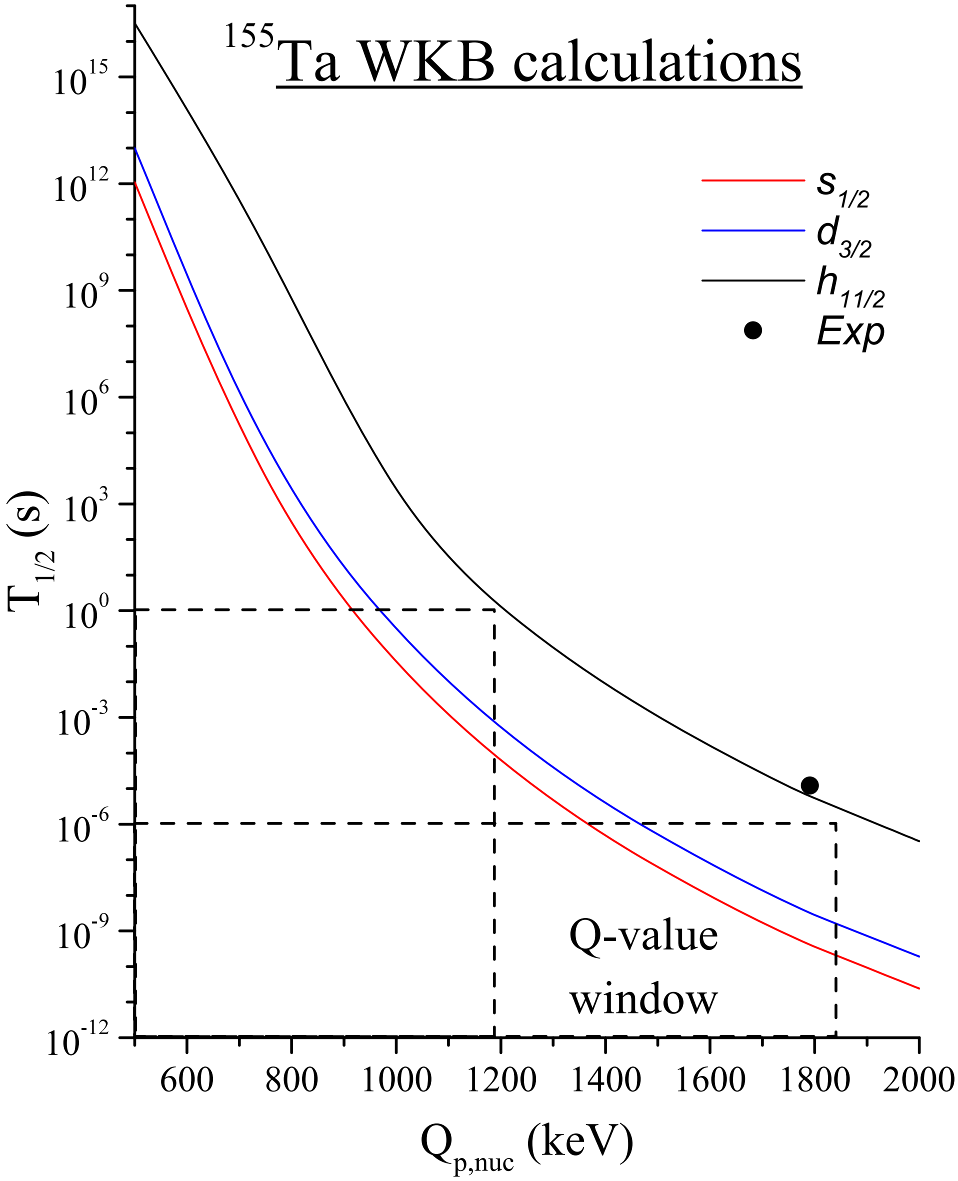

Figure 2.6: *Proton half-lives calculations for ^{155}Ta, calculated for protons with $l=0$, 2 and 5, using the BARRY code and compared to the experimental data. The Becchetti-Greenlees potential was used [Bec69].*

2.5.2 Proton-Nucleus Potentials

A number of potentials are available, and as mentioned, a common shape for the central nuclear potential is the Woods-Saxon, see Fig. 2.1. One commonly used potential is Becchetti-Greenlees [Bec69], which is an optical potential, the parameters of which were obtained from proton elastic scattering experiments performed at low energies ($10 < E < 100$ MeV) with medium to heavy targets ($A > 40$). Only the real part of this potential is necessary for barrier penetration calculations:

$$\begin{aligned} V(r) = -V_{N0} f(r, R_{nuc}, a_{nuc}) + V_{so0} l.s \lambda_{\pi}^{2} \tfrac{1}{r} \tfrac{d}{dr} f(r, R_{so}, a_{so}) \\ +V_C(r) + V_l(r) \end{aligned} \tag{2.20}$$

$$\begin{aligned} V_{N0} &= 54.0 - 0.32 Q_{p,nuc} + 0.4 Z/A^{1/3} + 24.0 (N-Z)/A \\ R_{nuc} &= 1.17 A^{1/3} \\ a_{nuc} &= 0.75 \\ V_{so0} &= 6.2 \\ R_{so} &= 1.01 A^{1/3} \\ a_{so} &= 0.75 \end{aligned}$$

Assuming a uniform charge distribution within the nucleus, one obtains a Coulomb potential:

$$V_C(r) = \begin{cases} (\frac{Ze^2}{4\pi\epsilon_0 R_C})(3 - \frac{r^2}{R_C^2}) & \textbf{for } r < R_C \\ \frac{Ze^2}{4\pi\epsilon_0 r} & \textbf{for } r > R_C \end{cases} \tag{2.21}$$

where $R_C = 1.21A^{1/3}$ fm. Semi-classical theory uses a centrifugal potential:

$$V_l(r) = \frac{l(l+1)\hbar^2}{2\mu r^2} \tag{2.22}$$

A number of other potentials are available, such as the ‘universal’ potential [Cwi87] or the liquid drop potential from Myer [Mye76]. It has been observed that calculated proton decay half-lives are relatively insensitive to the parameters chosen for the potential used, rarely differing by more than a factor of 2 when studying spherical nuclei [Åbe97].

Another proton-nucleus potential can be found in [Esb00] which has been used to calculate partial half-lives for deformed proton emitters, including nuclei presented in this thesis. These parameters were obtained by adjusting them to reproduce the decay of ^{131}Eu to the 2^+ state in ^{130}Sm. However, this does not preclude its use with spherical proton emitters for comparative purposes. A modified spin-orbit term is used, some details of which are discussed in Sec. 2.6.1. Here we only have to concern ourselves with the radial part of the spin-orbit term, along with the parameters:

$$V_{so} = 4V_{so0}l.s\frac{1}{r}\frac{d}{dr}f(r, R_{so}, a_{so}) \tag{2.23}$$

$$\begin{aligned}
R_{nuc} &= 1.25A^{1/3} \\
a_{nuc} &= 0.65 \\
V_{so0} &= 6 \\
R_{so} &= 1.25A^{1/3} \\
a_{so} &= 0.65
\end{aligned}$$

For V_{N0}, the Becchetti-Greenlees term is used. It should be noted that in a review of potentials for use in deformed proton decay calculations by Ferreira, Maglione and Fernandes, the Becchetti and Greenlees potential fares unfavourably, being unable to reproduce experimental data [Fer02]. The reason cited is the relatively small radius parameter of the Becchetti-Greenlees potential, with a larger radius being necessary for calculations to produce reasonable results. This is to account for longer range couplings within nuclei when, for example, deformation is involved.

2.5.3 Theory of Proton Decay

As more near-spherical proton emitters were discovered at Daresbury (such as ^{156}Ta and ^{160}Re [Pag92]), and then Argonne (^{157}Ta, ^{161}Re [Irv97]), theoretical interest in calculating proton decay widths has also grown, with a desire to move beyond the simple, semi-classical approach, to more complex methods.

The common thread with most of these methods is the view of spherical proton emitters as extremely narrow ($< 10^{-10}$ eV), quasi-bound resonances, the widths of which, when calculated, yield the proton partial half-life:

$$t_{1/2,p} = \frac{\hbar}{\Gamma} ln2 \tag{2.24}$$

Here, only two formalisms will be related in detail, the ‘direct’ and ‘distorted wave’ methods. Examples of other approaches to calculating proton decay widths can be found in Åberg, Semmes and Nazarewicz [Åbe97], where a review of formalisms developed through the 90’s is presented. A more recent, particle-vibrational coupling, formalism by Esbensen and Davids allows for proton emitters to experience quadrupole excitations, while still retaining a time-averaged spherical shape [Dav01].

2.5.3.1 Direct

Maglione, Ferreira and Liotta [Mag98] used the 'direct' method, describing the parent nucleus as a single nucleon moving within the potential of the daughter nucleus. The single particle wavefunction at a large distance, R, outside the nucleus is set to be an out-going Coulomb wave:

$$\psi^{out}(r) = \frac{u(r)}{r} = \frac{N[G_l(kr) + iF_l(kr)]}{r} \textbf{ at } r = R \tag{2.25}$$

where N is a normalisation constant, k the wavenumber and G_l and F_l are the irregular and regular Coulomb functions respectively. The probability flux of the particle penetrating a sphere far from the nucleus can then be calculated:

$$Flux = |\psi^{out}(\underline{\mathbf{r}})|^2 vr^2 sin\theta d\theta d\phi \tag{2.26}$$

where $v = \hbar k/\mu$ is the velocity of the particle. One can note that:

$$\lim r \rightarrow \infty |r\psi^{out}(r)|^2 = |N|^2 \tag{2.27}$$

as well as the fact that the flux is the inverse of the mean lifetime. One can then integrate the flux over all angles to obtain the 'direct' decay width

$$\Gamma^{Dir} = \frac{\hbar^2 k}{\mu}|N|^2 \tag{2.28}$$

The normalisation N, is determined by matching, at R_{mat}, the wavefunction $\psi^{out}(R_{mat})$ with the solution of the Schrödinger equation, $u(R_{mat})$.

An example of how this can be done is shown by Davids and Esbensen [Dav00a]. The Schrödinger equation to be solved is:

$$\frac{\hbar^2 k}{\mu}\frac{d^2}{dr^2}u(r) - V(r)u(r) = -Q_{p,nuc}u(r) \tag{2.29}$$

where $V(r)$ is given in equation (2.20), the only difference being the addition of a free parameter, f, that scales V_N0. This equation is solved numerically, for example using a simple 4-point difference formula [Koo90], out to radius R_{mat} which lies outside the nucleus. Boundary conditions are imposed, requiring $u(r)$ to be regular at the origin, and to match the logarithmic differentials of $u(r)$ and the irregular Coulomb function:

$$\frac{u'(r)}{u(r)} = \frac{G_l'(kr)}{G_l(kr)} \ \textbf{for} \ r = R_{mat} \tag{2.30}$$

If this condition is not met to within a certain numerical accuracy, one can perform another iteration, but changing the depth of the nuclear potential V_N0, with the f factor. The Coulomb functions were obtained using the method described in [Bar74]. One then has to normalise the wavefunction $u(r)$, requiring:

$$\int_0^R [u(r)]^2 dr = 1 \tag{2.31}$$

where one can simplify the calculation by approximating $u(r)$ with the irregular Coulomb function far from the nucleus:

$$u(r) = G_l(kr)\frac{u(R_{mat})}{G_l(kR_{mat})} \textbf{ for } r > R_{mat} \tag{2.32}$$

Finally, the normalisation factor N can be determined:

$$N(R) = \frac{u(R)}{G_l(kR) + iF_l(kR)} \tag{2.33}$$

which, when inserted in equation (2.28), yields the decay width. It should be noted that while the matching condition in equation (2.25) implies a complex wavefunction, and hence energy, the imaginary part of the decay width is usually extremely small, and hence real wavefunctions are used which results in:

$$N(R) = \frac{u(R)}{G_l(kR)} \tag{2.34}$$

This expression is actually very similar to the previous one (2.33), since we can always choose a value of R such that $G_l(kR) \gg F_l(kR)$. Reasonable matching and integral radii are $R_{mat} = 16$ fm and $R = 100$ fm.

2.5.3.2 Distorted Wave

Starting from the premise that proton emitters are extremely narrow resonances, and that the decay is a specific reaction channel, we can express the resonance width:

$$\Gamma^{DW} = 2\pi|T_{A+1,Z+1;A,Z}|^2 \tag{2.35}$$

where, using the distorted-wave Born approximation (DWBA), the transition amplitude can be written as:

$$T_{A+1,Z+1;A,Z} = \langle \psi_{Ap} \Psi_{Ap} | V | \Psi_{A+1} \rangle \tag{2.36}$$

where ψ_{Ap} is the incoming wave representing the motion of the proton relative to the daughter, Ψ_{Ap} is the product of the intrinsic proton and daughter wavefunctions and Ψ_{A+1} is the metastable state of the parent nucleus. The potential V is the normal proton-daughter interaction.

The Gell-Mann Goldberger transformation [Fes92] is then used to rewrite equation (2.36) as:

$$T_{A+1,Z+1;A,Z} = \langle \psi_{Ap} \Psi^{C}_{Ap} | V - V^{0}_{C} | \Psi_{A+1} \rangle \tag{2.37}$$

where Ψ^{C}_{Ap} is the scattering wavefunction associated with the point-like Coulomb potential, V^{0}_{C}. The wavefunction ψ_{Ap} can be written as the product of the intrinsic proton wavefunction (assumed to be in the ground state) and that of the daughter nucleus, Ψ_{Ap} (which is treated as an inert core). The radial part of Ψ^{C}_{Ap} is:

$$\Psi^{C}_{Ap} = \sqrt{\frac{2\mu}{\pi \hbar^2 k}} \frac{F_l(kr)}{r} \tag{2.38}$$

where k is the wave number and $F(kr)$ the regular Coulomb function. We can then numerically obtain the radial proton wavefunction $u(r) = r\psi_{Ap}(r)$, in a similar manner to that described in Sec. 2.5.3.1. Finally, we can combine equations (2.35-37) to yield an expression for the resonance width:

$$\Gamma^{DW} = \frac{4\pi}{\hbar^2 k} \left| \int_0^\infty F_l(kr)[V(r) - V_C^0(r)]u(r)dr \right|^2 \tag{2.39}$$

It has been shown by C. N. Davids [Dav00b] that the direct and distorted wave methods are equivalent, and for spherical proton wavefunctions produce the same result, with a small discrepancy due to difference in accuracy of the numerical methods used.

2.6 Deformed Proton Emitters

While the decay rates of the spherical proton emitters were reasonably explained by methods cited earlier in this chapter, the results for ^{109}I and ^{113}Cs, discovered at TUM (Technische Universität München) [Gil87], were in obvious disagreement with spherical decay calculations. It had been experimentally observed that a region of deformed nuclei existed above ^{100}Sn [She61]. Predictions and early experiments [Ars69, Lea82, Lis85] indicated a rapidly increasing prolate deformation above $Z, N = 50$, which reaches a plateau and then gradually falls approaching $Z = 82$. This onset of rapidly changing deformation between daughter and parent was one explanation of the large hindrances calculated for these two proton emitters by spherical calculations. Therefore, during the eighties and early nineties, Bugrov and Kadmenskii included deformation effects in their calculations and managed to reasonably account for these anomalous decay rates [Bug89, Kad96]. A limiting factor was the scarcity of data available at the time, with only 3 proton emitting states exhibiting these anomalous decay rates. This limited the confidence with which one could one could explain the anomalies as being caused by, for example, deformation alone.

Then at ANL in the nineties, the proton emitters ^{131}Eu and ^{141}Ho were discovered, and again the experimental half-lives were not well reproduced using spherical calculations [Dav98]. That these nuclei were deformed was confirmed by the γ-spectroscopy studies of ^{131}Eu and ^{141}Ho [Sew01a, Sew01b]. The observation of these additional examples of nuclei, later including ^{140}Ho at ORNL [Ryk99], with anomalous decay rates sparked further interest in descriptions of deformed proton emitters in various theoretical groups. One of the clearest examples of deformation being involved in proton decay was the fine-structure exhibited in the decay of ^{131}Eu to the low-lying 2^+ excited state in ^{130}Sm [Son99].

As an example of the latest theoretical work on deformed proton emitters, a coupled-channel approach will be discussed here. The method described in Sec. 2.5.3 is a special, spherical, case for this method by Davids and Esbensen [Dav00a]. I will then mention a method for calculating the decay width of an odd-odd deformed proton emitter, in which the odd neutron is also accounted for.

2.6.1 Coupled-Channel Approach

This approach models the decaying system as an unbound proton interacting with an axially symmetric deformed core; a particle-rotor system. We will start with the more general formulation then end by using the adiabatic approximation which was used to perform the calculations found in Chap. 4. In the laboratory frame, for a total spin I of the decaying state, we label the channels by the quantum numbers (ljR) where lj specify the single particle orbits and R the angular momentum of the core i.e. the daughter nucleus. The rotor possesses a low-lying rotational band, with energy $E_R = (\hbar^2/2J_0)R(R+1)$, where J_0 is the moment of inertia and $R = 0, 2, 4....$ For the adiabatic limit, used in Sec. 4.6.1.3, E_R is set to zero.

The total wavefunction is:

$$\Psi_{IM}(\underline{\mathbf{r}}, w) = \sum_{ljR} \frac{\psi^I_{ljR}}{r} |l(jR)IM\rangle \tag{2.40}$$

where

$$|l(jR)IM\rangle = \sum_{mM_R} \langle jmRM_R|IM\rangle |RM_R\rangle |ljm\rangle \tag{2.41}$$

is the channel-spin wavefunction, obtained by coupling the single particle wavefunction $|ljm\rangle$ to that of the rotor $|RM_R\rangle$, with M being the projection of the total spin on the laboratory axis.

The Hamiltonian of the proton-core system is:

$$H = T + V(\underline{\mathbf{r}}, w) + V_{ls}(r, \theta) + H_R \tag{2.42}$$

consisting of the relative kinetic energy T, the Coulomb plus nuclear interaction $V(\underline{\mathbf{r}}, w)$ which depends on the position $\underline{\mathbf{r}}$ of the proton and w, the Euler orientation angle or orientation of the rotor. H_R is the rotor Hamiltonian. The nuclear and Coulomb term is expanded in even multipoles:

$$V(r, w) = \sum_{\lambda} V_\lambda(r) P_\lambda[cos(\theta')] \tag{2.43}$$

where θ' is the orientation of the proton with respect to the symmetry axis of the rotor. Including this in the Schödinger equation, along with the wavefunction from eqn. (2.40) results in the set of coupled differential equations for the radial wavefunction:

$$\begin{aligned}(h_{lj} + E_R - E)\psi^I_{ljR}(r) = &- \sum_{l'j'R'} \sum_{\lambda \neq 0} \langle l(jR)IM | P_\lambda[cos(\theta')] \\ &\times | l'(j'R')IM \rangle V_\lambda(r) \psi^I_{l'j'R'}(r)\end{aligned} \tag{2.44}$$

where h_{lj} includes the monopole terms of the interaction:

$$h_{lj} = \frac{\hbar^2}{2\mu}\left(-\frac{d^2}{dr^2} + \frac{l(l+1)}{r^2}\right) + V_0(r) + V_{ls}(r) \tag{2.45}$$

In a similar way one can include the deformed spin-orbit interaction [She69] which has the form:

$$V_{ls}(r,\theta) = 4V_{SO}([\nabla f(r,\theta)] \times \underline{\mathbf{p}}).\underline{\mathbf{s}} \tag{2.46}$$

where θ is he angle between $\underline{\mathbf{r}}$ and the symmetry axis of the rotor, $\underline{\mathbf{p}}$ is the momentum and $f(r,\theta)$ is the Fermi function. Using the multipole expansion $f(r,\theta) = \Sigma_\lambda f_\lambda(r) P_\lambda[cos(\theta)]$, we can derive the expression:

$$\begin{aligned}V_{ls}(r,\theta) =&4V_{SO} \sum_\lambda \left(\frac{1}{r}\frac{df_\lambda}{dr} P_\lambda \underline{\mathbf{l}}.\underline{\mathbf{s}} - \frac{f_\lambda}{r}[\underline{\mathbf{l}}.\underline{\mathbf{s}}, P_\lambda]\frac{d}{dr} \right. \\ &\left. - \frac{f_\lambda}{r^2}\frac{dP_\lambda}{d\,cos(\theta)}\frac{\underline{\mathbf{r}}.\underline{\mathbf{s}}}{r} l_z \right)\end{aligned} \tag{2.47}$$

Further details of these potentials can be found in Davids and Esbensen

[Dav00a].

2.6.1.1 Direct

The decay width can be determined in similar way to that described in Sec. 2.5.3.1, with the total decay width being the sum of the partial decay widths:

$$\Gamma_{IR} = \sum_{lj} \Gamma^{I}_{ljR} = \sum_{lj} \frac{\hbar^2 k_R}{\mu} |N^{I}_{ljR}|^2 \tag{2.48}$$

where $\hbar k_R = \sqrt{2\mu|E - E_R|}$ is the momentum of the emitted proton, and $|N^{I}_{ljR}|$ can be either determined by the direct or distorted wave method.

A resonance solution for the radial wavefunction $u_{nn_0}(r)$, where $n = (ljR)$, can be obtained numerically. A boundary condition of the solution is the requirement that all solutions be regular at the origin, i.e. $u_{nn_0}(r = 0) = 0$. A simple way to generate solutions for a fixed n_0 is to require:

$$u_{nn_0}(r) \to \delta_{nn_0} r^{l+1} \textbf{ for } r \to 0 \tag{2.49}$$

so only channel $n = n_0$ has a non-zero wavefunction near the origin. The coupled equations from eqn. (2.44) are solved out to the matching radius, r_{mat}, outside of the nucleus, where they are matched to Coulomb wavefunctions

$$u_{nn_0}(r) = A_{nn_0} F_l(k_R r) + B_{nn_0} G_l(k_R r) \tag{2.50}$$

A general set of solutions to the coupled equations can be expressed as

$$\psi_n(r) = \sum_{n_0} \alpha_{n_0} u_{nn_0}(r) \tag{2.51}$$

We can determine the resonance solution be requiring $\psi_{ljR}(r)$ match the irregular Coulomb wavefunction at $r = r_{mat}$. Using the Wronskian $F_l G_l - G_l F_l = k_R$ and the equivalent expression for the radial derivative of u_{nn_0}, we obtain :

$$\psi_n(r) = \left(\sum_{n_0} \alpha_{n_0} A_{nn_0} \right) F_l(k_R r) + \left(\sum_{n_0} \alpha_{n_0} B_{nn_0} \right) G_l(k_R r) \tag{2.52}$$

where we can see that the regular solution, $F_l(k_R r)$ disappears if:

$$\sum_{n_0} A_{nn_0} \alpha_{n_0} = 0 \textbf{ i.e. if } det\{A_{nn_0}\} = 0 \tag{2.53}$$

The resonance solution $\psi_n(r)$ is then normalised c.f. eqn. (2.31).

Since real energies have been adopted, for $E > E_R$, we can obtain $|N^I_{ljR}|$ for the direct method with $\psi^I_{ljR}(r_{mat}) = N^I_{ljR} G_l(k_R r_{mat})$, as with eqn. 2.34.

2.6.1.2 Distorted Wave

Once the resonance solution of the total wavefunction Ψ_{IM} has been found numerically out to a matching radius, the DW method can be used to include long range Coulomb interactions, producing an outgoing wavefunction out to a larger integration radius, r_{int}. The expression for the outgoing wave function is provided by Davids and Esbensen [Dav00a], who generalise this to the non-adiabatic case by inserting the correct proton momenta to account for the excitation energy of the rotor, $\hbar k_R = \sqrt{2\mu(E^{-}E_R)}$. Thus, for $r \to \infty$ we obtain the expression:

$$\Psi_{IM}^{out}(\underline{\mathbf{r}}, w) = \sum_{ljR} N_{ljR}^{DW} \frac{1}{r} [G_l(k_R r) + iF_l(k_R r)] |(ljR)IM\rangle \tag{2.54}$$

where

$$\begin{aligned} N_{ljR}^{DW} = &- \frac{2\mu}{\hbar^2 k_R} \int_0^{r_{int}} dr \ rF(k_R r) \langle l(jR)IM | V(\underline{\mathbf{r}}, w) + V_{ls}(r) \\ &- V_C^0(r) | \Psi_{IM}(\underline{\mathbf{r}}, w) \rangle \end{aligned} \tag{2.55}$$

with V_C^0 as the point Coulomb interaction between the proton and daughter nucleus. The three parts of the interaction are then expanded in the form shown in (2.43), resulting in the multipole terms shown in eqn. (2.44), with the addition of the point Coulomb interaction in the monopole part in eqn. (2.45). Inserting this expansion, along with the expression for the resonance wave function (2.40) into eqn. (2.55) yields:

$$\begin{aligned} N_{ljR}^{DW} = &- \frac{2\mu}{\hbar^2 k_R} \sum_{\lambda} \sum_{l',j',R'} \langle (ljR)IM | P_\lambda | (l'j'R')IM \rangle \\ &\times \int_0^{r_{int}} dr \ F_l(k_R r) V_\lambda(r) \psi_{l'j'R'}^I(r) \end{aligned} \tag{2.56}$$

The amplitude N_{ljR}^{DW} can determine the partial widths in (2.48).

As mentioned in Sec. 2.5.3, the direct and DW decay widths are the same for spherical nuclei. For deformed nuclei, this is still true for $r_{mat} = r_{int}$. However, it has been shown that when $r_{int} \gg r_{mat}$, this is not true since the DW method can now include longer range Coulomb couplings to first order

[Esb00]. This results in DW widths being independent of r_{mat} provided it is outside of the nucleus. The direct width approaches the value of the DW as r_{mat} approaches r_{int}. But note that it is calculationally much easier to extend the integration radius, rather than r_{mat} which would involve numerically calculating the wavefunction out to a very large radius.

2.6.1.3 K Representation and the Adiabatic Limit

An alternative to the R representation is to describe the system in the body-fixed frame of the rotor, where the included channels are labelled (ljK), K is the projection of I on the symmetry axis. This representation has the advantage that it simplifies calculations in the adiabatic limit, where the rotor excitation energy is set to zero.

Transformations can be made between the R and K basis, and it can be shown [Esb00] that:

$$\psi_{lj}^{IK}(r) = \sum_R A_{jR}^{IK} \psi_{ljR}^{I}(r) \quad \textbf{and} \quad \psi_{ljR}^{I}(r) = \sum_{K>0} A_{jR}^{IK} \psi_{lj}^{IK}(r) \tag{2.57}$$

where

$$A_{jR}^{IK} = \sqrt{\frac{2R+1}{2I+1}} \langle jKR0|IK\rangle \sqrt{1+(-1)^R} \tag{2.58}$$

assuming R is even, which is true for ground state rotational band of a quadrupole deformed nucleus. Note also that K is sign degenerate, hence we can limit ourselves to only positive values.

The coupled equations (2.44) can be obtained in the K representation by using the relations (2.57) and then summing over R

$$\begin{aligned}(h_{lj}-E)\psi_{lj}^{IK}(r)+\sum_{K'>0}W_{KK'}^{jI}\psi_{lj}^{IK'}(r) = \\ -\sum_{l'j'}\sum_{\lambda>0}\langle ljK|P_\lambda|l'(j'K\rangle_0 V_\lambda(r)\psi_{l'j'}^{IK}(r)\end{aligned} \tag{2.59}$$

where

$$W_{KK'}^{jI}=\sum_R A_{jR}^{IK}E_R A_{jR}^{IK'} \tag{2.60}$$

This coupling matrix is not purely diagonal, the off-diagonal terms being independent of r and a result of Coriolis mixing between neighbouring K values. For a constant motion of inertia i.e $E_R=(\hbar^2/2J_0)R(R+1)$, the off-diagonal terms [Ker56] become:

$$\begin{aligned}W_{K,K+1}^{jI}=&W_{K+1,K}^{jI}= \\ &-\frac{\hbar^2}{2J_0}\sqrt{(I-K)(I+K+1)(j-K)(j+K+1)}\end{aligned} \tag{2.61}$$

with the equivalent expression for the diagonal terms being

$$\begin{aligned}W_{KK}^{jI}=&-\frac{\hbar^2}{2J_0}[I(I+1)+j(j+1)-2K^2 \\ &+\delta_{K,1/2}(-1)^{I+j}(I+1/2)(j+1/2)]\end{aligned} \tag{2.62}$$

Further refinements may be needed since calculations using this method does not reproduce experimental results very well.

Using the adiabatic limit in the K representation eliminates the off diagonal Coriolis terms, simplifying the calculation. Using the transformation (2.57) on eqn. (2.56), including the single particle matrix elements of the Legendre polynomials [Esb00] and summing over R' results in the DW amplitude:

$$\begin{aligned} N_{ljR}^{DW} &= -\frac{2\mu}{\hbar^2 k_R} \sum_{\lambda l' j'} \langle ljK | P_\lambda | l'j'K' \rangle \\ &\times \int_0^{r_{int}} dr \; F_l(k_R r) V_\lambda(r) \psi_{l'j'R'}^{IK}(r) \end{aligned} \tag{2.63}$$

This expression is equivalent to that found in [Dav00a] for a ground-state to ground-state decay.

2.6.2 Odd-Odd Emitters

In the current descriptions of proton emitters, the odd neutron in odd-odd proton emitters is treated as part of the inert core. However, a formalism developed by Ferreira and Maglione [Fer01], includes the odd neutron as part of a rotor plus two particle system.

The potential is not modified to include any residual p-n interactions, but the presence of the neutron allows the emitted proton to possess more than one possible value of j. In fact, a number of channels are now possible due to the coupling of $J + j = J_T$ where J is the angular momentum possessed by the daughter nucleus, and J_T is that possessed by the decaying nucleus.

The rotational band head is the parent nucleus angular momentum projection on the symmetry axis, $K_T = |K_p \pm K_n|$, and the two possible rotational bands are formed by the parallel and anti-parallel alignment of the proton and neutron angular momenta projections. Note that we can assume that the decaying nucleus is in the band head, so that $K_T = J_T$. Also, since the even-even daughter nucleus is treated as an inert core, and the odd neutron is treated as a spectator, $K_D = K_n$.

The partial decay width for a specific channel is similar to eqn. (2.48), with the addition of the overlap of the proton-daughter, and parent nucleus systems as well as a Clebsch-Godon term resulting from the angular momentum coupling of the odd nucleons. The expression for the partial decay width:

$$\Gamma^J_{lj} = |N_{lj}|^2 \frac{\hbar^2 k}{\mu} \frac{2J+1}{2K_T+1} \langle J K_n j K_p | K_T K_T \rangle^2 \tag{2.64}$$

which is summed, along with the other partial widths allowed by parity and angular momentum conservation to produce the total decay width:

$$\Gamma^J = \sum_{j=max(|J-K_T|,K_p)}^{J+K_T} \Gamma^J_{lj} \tag{2.65}$$

The actual method used to calculate the resonance solutions and proton wavefunctions is based on that shown in Sec. 2.6.1, and the calculations that will be discussed further in Chap. 4, were performed using the adiabatic limit and the distorted wave method.

2.7 Spectroscopic Factors

The theoretical descriptions of proton decay described in this thesis neglect some nuclear structure effects involved in obtaining the absolute proton decay rate. Specifically, the effects of incomplete overlap of parent and daughter wavefunctions caused, for example, by a hole in the parent state of a proton emitting nucleus being filled in the daughter. This effect is accounted for with the spectroscopic factor S.

Theoretical spectroscopic factors can be calculated analogously with proton-pickup reactions where:

$$S_p^{th} = \langle \psi_{J_i m} || a_{nlj}^{+} || \psi_{J_f m} \rangle |^2 \tag{2.66}$$

is the measure of the fragmentation of the single-particle orbital (njl), with a_{nlj}^{+} as the creation operator [Hey94]. The proton is emitted (or removed) from the nucleus (J_i) with angular momentum j, leaving the nucleus in its final state (J_f). It is a measure of the probability that a hole will exist within an orbital. Presented here are two methods for calculating theoretical spectroscopic factors.

These can be compared to experimental data with an experimental spectroscopic factor:

$$S_p^{exp} = \frac{t_{1/2}^{th}}{t_{1/2}^{exp}} \tag{2.67}$$

which is the ratio of the experimental and theoretical half-lives calculated using any of the methods described here. Since the theoretical half-life assumes an inert core, the ratio between the actual and theoretical half-life is indicative of the influence of structure effects, such as the degree of parent-daughter wavefunction overlap. Incomplete overlap is a hindrance to any decay, which can only result in longer experimental half-lives, and hence to spectroscopic factors less than unity.

2.7.1 Low-Seniority Method

Davids *et al.* performed a low-seniority spherical shell-model calculation for the spectroscopic factor of proton emitters between $64 < Z < 82$ [Dav97]. The model space consists of the eighteen particles in the $s_{1/2}, d_{3/2}$ and $h_{11/2}$ proton orbitals, the neutrons being considered spectators. The two body pairing Hamiltonian is:

$$\begin{aligned} H = &\sum_j \epsilon_j n_j + G_p \sum_{j,j'} (-1)^{l+l'} \left[\left(j + \frac{1}{2} \right) + \left(j' + \frac{1}{2} \right) \right]^{1/2} \\ &\times a^+(j^2) a(j'^2) \end{aligned} \tag{2.68}$$

where G_p is the strength of the proton pairing interaction, ϵ_j and n_j are the single particle energies and particle numbers in orbital j, and $a^+(j^2), a(j'^2)$ are, respectively, the creation and annihilation operators for a pair of protons in orbital j, coupled to spin 0. One of the major assumptions that simplifies this calculation is that the orbitals are all degenerate ($\epsilon_j = \epsilon$), allowing the use of the quasi-spin lowering and raising operators:

$$\begin{aligned} S^+ &= \sum_j (-1)^l \left(j + \frac{1}{2} \right)^{1/2} a^+(j^2) \\ S^- &= \sum_j (-1)^{l'} \left(j' + \frac{1}{2} \right)^{1/2} a(j^2) \end{aligned} \tag{2.69}$$

The Hamiltonian (2.68) is then of the form

$$H = N\epsilon + G_p S^+ S^- \tag{2.70}$$

where N is the number of particles occupying the relevant single-particle levels. Since the quasispin operators obey the normal angular momentum commutation relations, we have

$$[S^{+}, S^{-}] = 2S_0 = N - \sum_{j} \frac{2j+1}{2} = N - \Omega \tag{2.71}$$

where Ω is the total number of pair states. The lowest seniority eigenfunctions of the quasispin operator can then be obtained [Law80] as being:

$$\begin{aligned} &\phi^{S=\Omega/2}_{S_z=1/2(N-\Omega)} \ \textbf{for even Z,}\ J=0 \\ &\phi^{S=(\Omega-1)/2}_{S_z=1/2(N-\Omega)} \ \textbf{for odd Z,}\ J=j \end{aligned} \tag{2.72}$$

With a total of eighteen protons in the three orbitals in the model space being considered, $\Omega = 18$. Setting p to be the number of proton pairs counting down from $Z = 82$, we have $N = 18 - 2p$ for even Z nuclei, and $N = 19 - 2p$ for the odd Z proton emitters, for $1 \leq p \leq 9$.

We can now obtain the spectroscopic factor, defined as the overlap between parent and daughter wavefunctions:

$$S^{th}(p) = |\langle \psi^{4}_{5-p}(J=j)|a^{1/2+}_{1/2}(j)|\psi^{9/2}_{9/2-p}(J=0)\rangle|^2 \tag{2.73}$$

which is then reduced to

$$S^{th}(p) = \left(\frac{9}{2}\frac{1}{2}\frac{9}{2} - p\frac{1}{2} \right)^2 |\langle \psi^{4}||a^{1/2+}||\psi 9/2\rangle|^2 \tag{2.74}$$

The Clebsch-Gordon coefficient contains the p dependence. The reduced matrix element is then solved for $p = 9$, where $S(9) = 1$, yielding the result:

$$S^{th}(p) = p/9 \tag{2.75}$$

2.7.2 BCS Method

A more sophisticated alternative method for calculating proton spectroscopic factors is presented by Åberg, Semmes and Nazarewicz [Åbe97], using the quasi-particle or BCS approximation. Here the ground state of the nucleus is a vacuum with respect to the quasi-particles (which are holes below, and particles above, the fermi surface) [Rin80].

One assumes that the ground state of the odd Z proton emitter is a one quasi-particle state ($\psi_{J_i m} = c^{+}_{nlj}|\overline{0}\rangle$, and that the daughter is an even-even nucleus ($\psi_{J_f m} = |\overline{0}\rangle$). This results in the spectroscopic factor (2.68) being:

$$S^{th}_{p} = |\langle\overline{0}|c_{nlj}a^{+}_{nlj}|\overline{0}\rangle|^2 = u_j^2 \tag{2.76}$$

where u_j^2 is the probability that a specific orbital is empty in the daughter nucleus, with 1 corresponding to a completely empty, and 0 a completely filled, orbital. c_{nlj} is the fermion creation operator associated with the BCS ground state wavefunction $|\overline{0}\rangle$, for details see [Hey94, Sor66]. It is assumed that the core, including any odd neutron in an odd-odd proton emitter, is inert.

The occupation probability ($v_j^2 = 1 - u_j^2$) can be calculated using the BCS method found in [Hey94, Naz90], where:

$$v_j^2 = \frac{1}{2}\left[1 - \frac{\epsilon' - \lambda}{E}\right] \tag{2.77}$$

with

$$E = [(\epsilon' - \lambda)^2 + \Delta^2]^{1/2}$$
$$\epsilon' = \epsilon_j + (4\lambda_2 - G_p)v_j^2$$

The proton pairing strength G_p is taken [Dud80] as being:

$$G_p = 1/A[19.9 + 0.176(N - Z)] \qquad (2.78)$$

and the single particle energies (ϵ_j) are calculated by solving Schrödinger's equation with the relevant potential [Naz90]. It should be mentioned that the occupation probability is sensitive to the single-particles energies, particularly those near the Fermi surface. The Fermi level (λ) and pairing gap (Δ) are obtained by simultaneously solving the pair gap and total particle-number (N) equations:

$$\Delta = G_p \sum_j u_j v_j \textbf{ and } N = \sum_j 2v_j^2 \qquad (2.79)$$

Finally, the coefficient λ_2 is defined by:

$$\frac{4\lambda_2}{G_p} = \frac{(\sum_j u_j^3 v_j)(\sum_j u_j v_j^3) - \sum_j u_j^4 v_j^4}{(\sum_j u_j^2 v_j^2) - \sum_j (u_j v_j)^4} \qquad (2.80)$$

Eqns. (2.79, 2.80) are solved numerically to obtain the occupation coefficients (2.77), and hence the spectroscopic factor.

For proton emitters, the model space consists of the five orbitals ($1g_{7/2}$, $2d_{5/2}$, $1h_{11/2}$, $2d_{3/2}$ and $3s_{1/2}$) above the $Z = 50$ closed shell. A final note is that this method can be extended to the case of deformed proton emitters, though with the main additional requirement of desiring accurate single-particle energy levels for all the relevant orbitals, particularly those lying near the Fermi surface.

Chapter 3

Experimental Method

As mentioned in Chap. 1, there are a number of problems associated with the production, detection and identification of exotic nuclei such as proton emitters. However, over the nineties, a recoil tagging technique has been successfully utilised in accessing these nuclei beyond the proton drip-line. This chapter will describe the equipment and technique used at ANL to search for new proton emitting nuclei.

In brief, the beam hits the target producing fusion evaporation residues which pass through the FMA. They are dispersed horizontally according to their A/Q, with up to three charge states from a single mass transmitted through the FMA to reach the focal plane detector which is a thin, gas-fill, Multi-Wire Proportional Counter (MWPC), known colloquially as the Parallel Plate Avalanche Counter (PPAC). This provides position and ΔE information on the ions, the former providing an A/Q for the residue, and latter enabling discrimination of any scattered beam which may have passed through the FMA. The recoil ions are then defocussed so as to cover the area of the DSSD. The DSSD, described in Sec 3.3, consists of 48×48 orthogonal

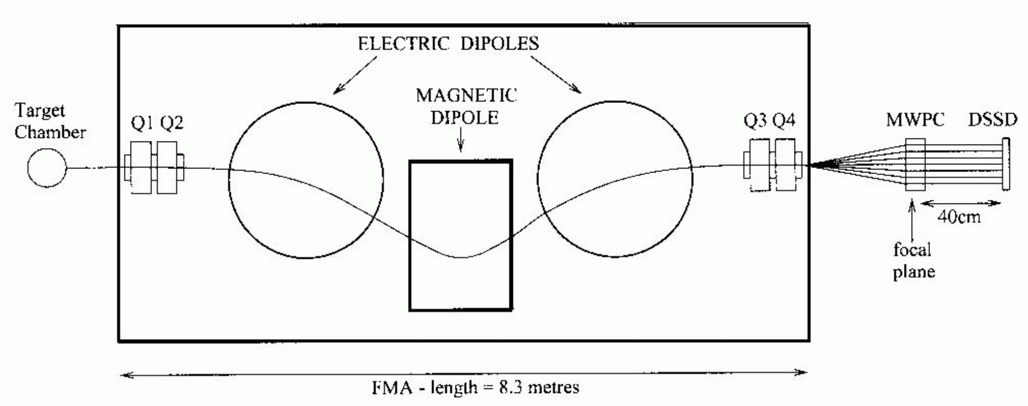

Figure 3.1: *Schematic of the experimental setup at the FMA.*

strips providing 2304 'pixels'. The ion implanted within a pixel then decays, these decays being recorded and distinguished from implant events by DSSD-MWPC anti-coincidences. The decays are correlated to the initial implanted ion, and its associated MWPC signal, from which mass assignments can be made. The decays can also be correlated to subsequent daughter decays, which if known, provide an extra handle on particle ion identification. A diagram of the setup is shown in Fig. 3.1.

3.1 Isotope Production

Heavy ion beams at ANL are provided by the Argonne Tandem Linear Accelerator System (ATLAS). It uses a 9 MV tandem Van de Graaff, or an upgraded electron cyclotron resonance (ECR) ion source linked to a 12 MV linac called the Positive Ion Injector (PII), to inject ions into a 20 MV 'booster' linac, followed by the 20 MV ATLAS linac section, see Fig. 3.2. ATLAS can provide beams up to 17 MeV per nucleon, providing more than enough energy to perform fusion evaporation reactions in the heavy mass region of the proton dripline ($Z > 50$). With the ECR, the ATLAS can produce a wide variety of beams up to uranium, including elements, such as selenium or the noble gases, which are hard to produce efficiently as negatively charged ions which are needed in a tandem accelerator such as is the case in Legnero or ORNL. Beam currents of up to 300 pnA of ^{58}Ni have been achieved using the new ECR source.

All of the ground state proton emitters observed so far have been produced by heavy fusion ion evaporation reactions. The beam and target combination are chosen to produce a compound nucleus as proton rich as possible. Points to be considered included the variety of isotopes available for the beam. Isotopically enriched material is available, but can become prohibitively expensive for use as a beam, so generally the initial source of ions is from commercially available elements with their natural isotopic abundances. The accelerating structure can then be tuned to selectively accelerate the isotope of the desired mass down the beamline to the target, with maximum currents dependant on their isotopic abundances. Another decision is whether one desires normal or inverse kinematics, though this may be determined by the availability of targets. Inverse kinematics can increase transmission of the desired nucleus through the FMA to the detector since the recoils are more forward focused, hence more recoils being accepted by the FMA. The caveat is that inverse reactions can also increase the amount of scattered beam which can pass through the FMA and reach the focal plane detector, the MWPC. This can provide some constraints on the experiments, and are discussed later in this chapter.

The beam energy is chosen, along with the target thickness, to optimise

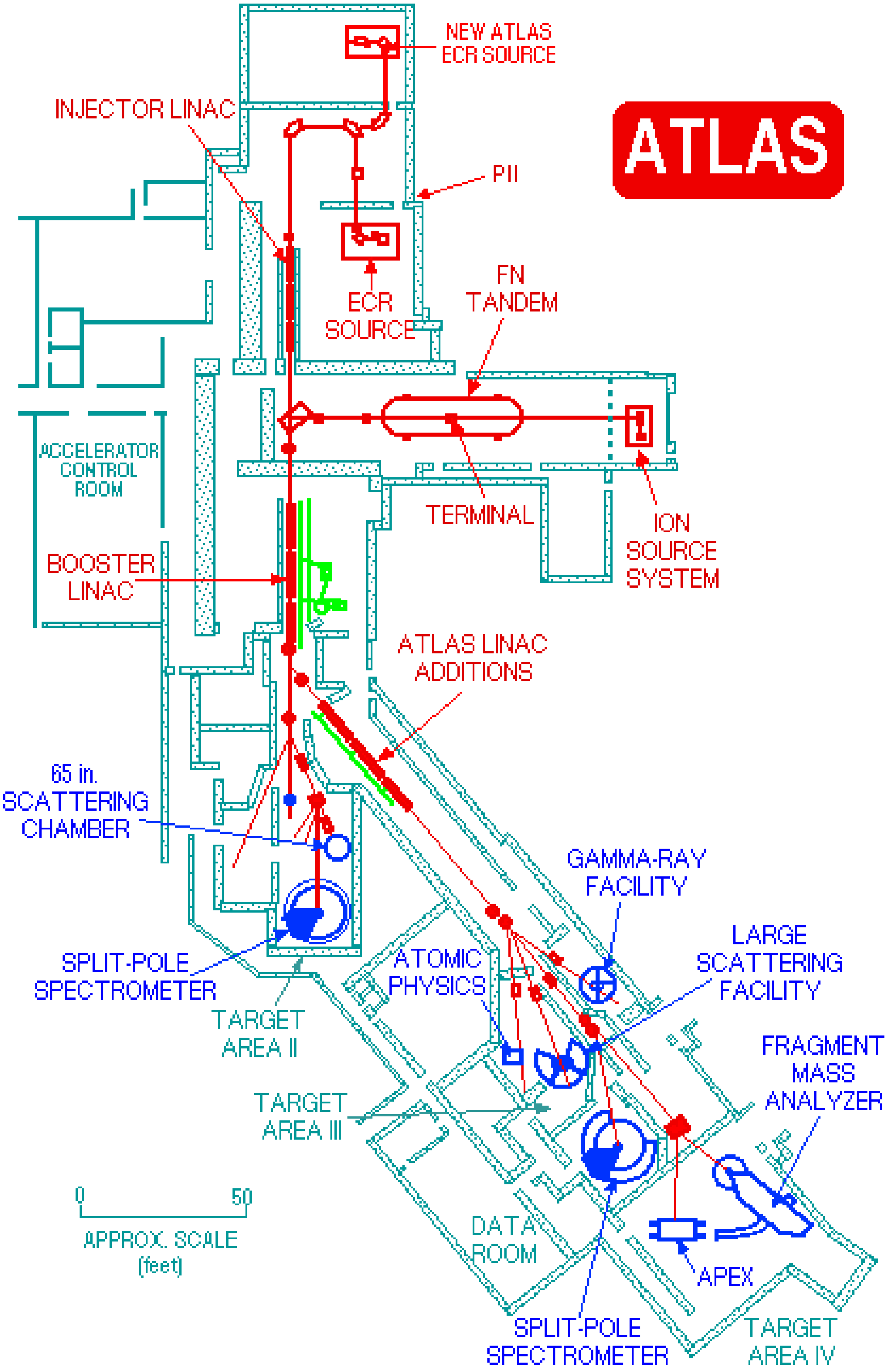

Figure 3.2: *Layout of ATLAS in the experimental area at ANL (2000).*

the excitation energy of the compound nucleus for the desired evaporation channel, with this optimum energy ideally achieved in the center of the target so that a range of energies around the theoretical maximum are covered. The choice of target thickness has to take into account two conflicting criteria, that thicker targets produce a higher yield of evaporation products, but that they also result in the recoils straggling and having an energy spread which may be larger than the acceptance of the FMA. In general, the targets chosen were just under 1 $\mathrm{mg/cm^2}$, the actual thickness dependent on the availability and in some instances, the ability of the target material to withstand the beam currents desired. The choice of the optimum excitation energy for the desired channel was made by comparison with other experiments performed in this region, as well as using the HIVAP cross-section code from GSI [Rei81, Rei85].

The HIVAP code is a statistical calculation program which models the fusion-evaporation/fission of a compound nucleus. The evaporation component of the break up is modelled using the WKB calculations and a real optical potential [Ver84]. Effective fission barriers are adjusted to fit experimental data [Rei85], and the level densities which are needed to calculate fission barriers are obtained using the two-Fermi gas model [Boh69]. In fact, it has been the study of the effective fission barrier which has fuelled the development of this code at GSI. The excitation of the compound nucleus is determined by the beam energy and mass differences of the constituent nuclei. Where experimental data is not available, mass predictions are used, such as Liran-Zeldes [Lir76].

In the first experiment, a ladder was used to mount up to four targets, which could be raised or lowered to change the target. Later, a wheel target holder became available, again with four target positions. This wheel can be rotated so that the beam would trace a circular path across the target. This would spread the energy across a larger area of the target, reducing the damage it experiences, and enabling higher beam intensities to be used, though this function was not used in the experiments described in this thesis. This facility could be coupled with a beam ‘wobbler’ which oscillates the beam in a vertical direction, again to spread the deposited beam energy over a larger area. A beam sweeper is synchronised with the wheel to divert the beam when the wheel spokes were in the beam’s path, preventing the beam being scattered off the spokes.

In the second set of experiments described in this thesis, the wheel holder was used. Different targets were placed in each position, the wheel being rotated to change target. The wobbler was used to reduce the damage to the target by the beam.

A 20 μg/cm^2 carbon reset foil is placed a few centimeters downstream of the target to equilibrate the charge state of recoil ions before they enter the FMA.

3.2 Fragment Mass Analyser

The FMA, shown in Fig. 3.3, is a triple-focusing electromagnetic mass separator, designed to separate nuclear reaction products from the primary beam and disperse them according to their A/Q at the focal plane [Dav89, Dav92]. It consists of two electric dipoles and a 40^0 magnetic dipole, as shown in Fig. 3.1. This layout results in no energy dispersion for the ions, but they are achromatically dispersed at the focal plane according to their A/Q. The

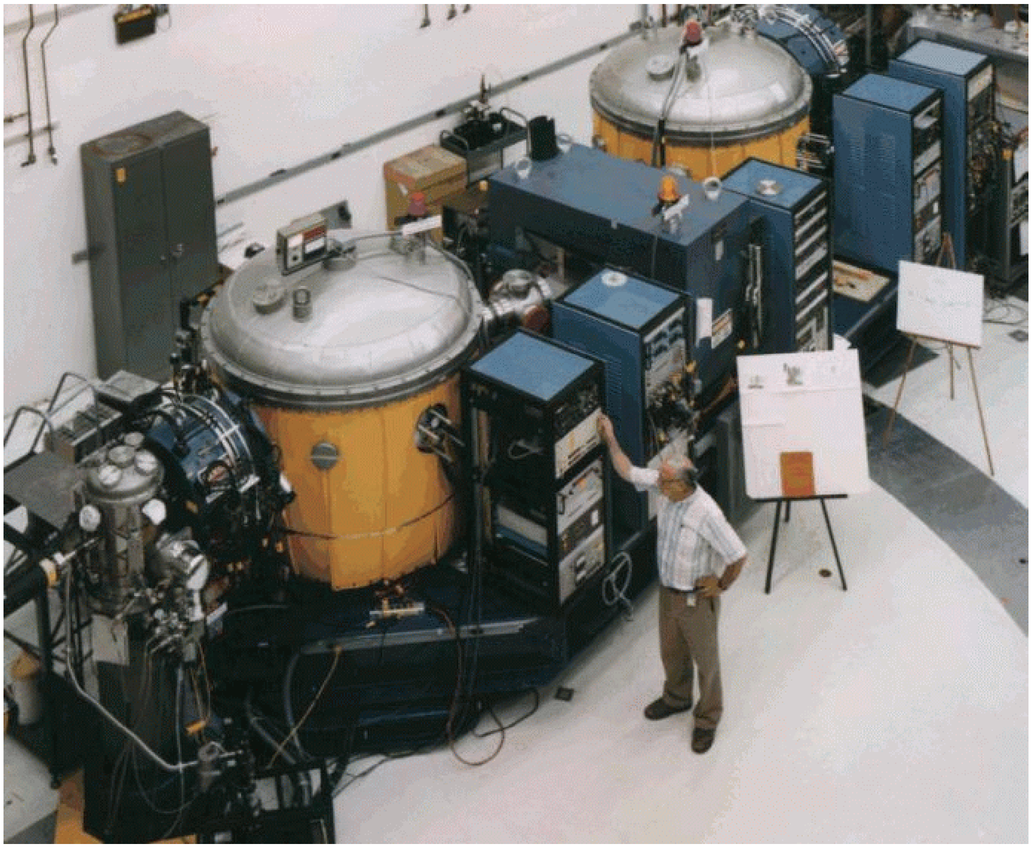

Figure 3.3: *Photograph of the FMA.*

advantages of this setup are its large acceptance in A/Q, energy, and solid angle (±7%, ±20% and $\sim$ 8 msr respectively), resulting in a transmission efficiency of 10%-20%, depending on the reaction involved. The beam is stopped at the anode of the first electric dipole, but multiple scattering can result in some beam reaching the focal plane, though beam rejection is quite high - of the order of 10^{-12}. Quadrupole doublets at the front and back of the FMA provide extra geometric focussing and second-order corrections.

The quadrupoles can also be used to vary the A/Q dispersion, though this is usually set at 10mm/%. The mass resolution achieved by the FMA is typically: $M/\Delta M \sim 350$. An example of the setup, including data taken from the focal plane MWPC, will be shown in section 3.6.

The FMA is relatively simple for an experimental user to operate since a dedicated microcomputer constantly monitors the fields, currents, voltages and vacuum of the FMA. The FMA can be setup for an experiment by simply inputting the mass, energy and charge state of the recoil desired [A,E,Q], and the computer will automatically calculate and adjust the fields necessary to transmit the specified ion through the FMA. In fact, a web-based code can be used to calculate the energy and optimum charge state for a specific beam and target [Blu96]. However, this calculated charge state sometimes has be to changed manually, depending on the specific experiment. The first reason is when scattered beam arrives at the focal plane due to coincident A/Q. This can increase the count rate at the focal plane detector, increasing dead-time and damaging the MWPC. The other reason is related to the number of charge states of a specific mass transmitted to the focal plane. For heavy ion experiments, such as proton radioactivity searches with $A > 100$, up to three charge states are transmitted. However, in specific cases, the yield in the states on the edge of the MWPC can be small, and the overall yield can be improved by only transmitting two charge states, neither of which are near or past the edge of the detector at the focal plane.

3.3 Detection System

The basic layout of the focal plane detectors is shown in Fig. 3.4, along with a photograph of the same in Fig. 3.5. The MWPC (or PPAC), lies at the focal plane and records energy loss, TOF with the DSSD, and the position

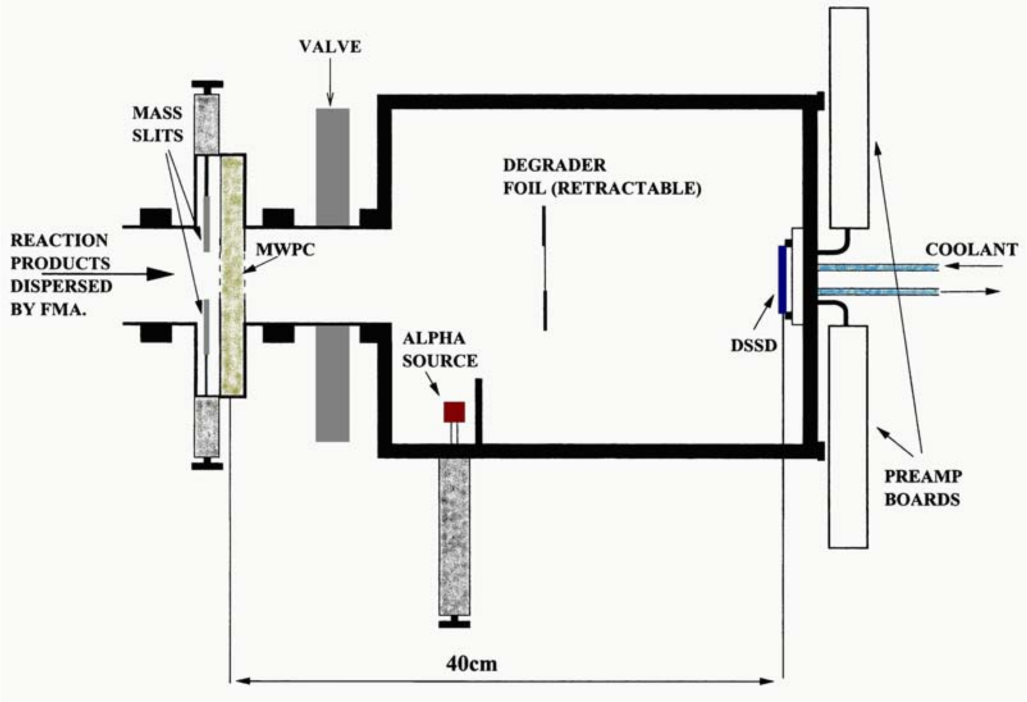

Figure 3.4: *Diagram showing the chamber containing the detection system at the end of the FMA .*

of the ions as they pass through it. The ions then pass through a degrader whose thickness is chosen to insure that the desired recoils are implanted at a reasonable energy. Too high an energy increases the dead-time after implantation due to saturation of the amplifier. Too low an energy and the recoil may be imbedded too close to the surface, with a larger fraction of the proton emitted upstream escaping out of the front of the detector. An implantation depth of about 10μm is typical in most experiments, corresponding to several 10's of MeV for a recoil ion.

The α-source is introduced in front of the DSSD for gain-matching an initial online calibration, and can be used to monitor the degradation in resolution of the DSSD due to radiation damage. This also provides a

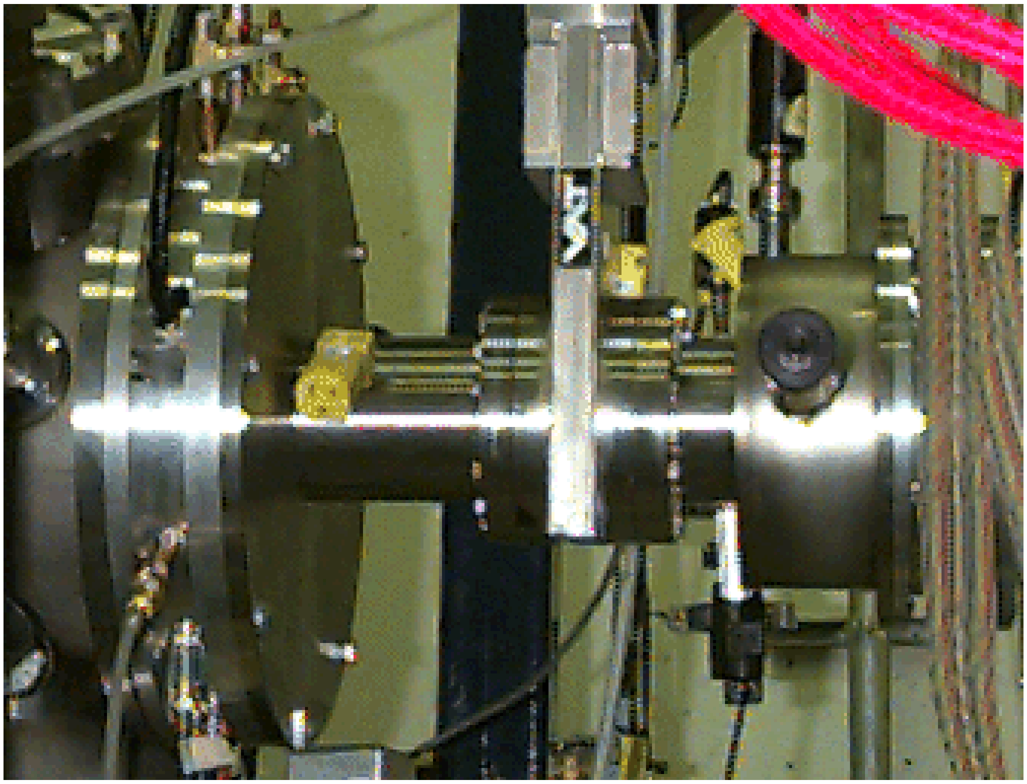

Figure 3.5: *Photograph showing a side-view of the chambers at the FMA focal plane containing the PPAC and DSSD detectors.*

check as to whether any gain-shifts have occurred over the course of a longer experiment.

The recoils are then implanted within the DSSD, lying 40 cm downstream from the PPAC. The 48×48 orthogonal strips of the DSSD form 2304 'pixels' in which correlations can take place. Implant events are categorised by their energies which are 10's of MeV, decays being only a few MeV, as well as PPAC-DSSD coincidences, decays by DSSD signals anti-coincident with the PPAC. All the events are time-coded by a 48-bit, 100 ns counter (which can run for a year without needing to be reset). Implant-decay and decay-decay correlations are used to identify known transitions, as well as assign new ones to their parent nuclei. The implantation rate establishes the limit on how long a correlation time can be used with confidence. If implantation times within a pixel are comparable with decay lifetimes, then the likelihood that the mis-assignment of a decay can occur increases, with decays incorrectly associated with implants. This would be caused by a decay from a previously implanted ion occurring, within the same pixel, before the newly implanted nucleus can itself decay. Since most proton and α-decays in the region of interest occur within 100 ms, implantation rates of 2 kHz on a DSSD with around 2000 pixels results in a mean time between implant events of $\sim$ 1 s, adequate for most purposes. Below $Z = 68$, α-decay is uncommon and there is a region of deformed nuclei, with some cases where the proton decay is predicted to be quite fast ($t_{1/2} < 10$ ms), where there are no daughter α-decays which could require longer correlation times. This enables the PPAC rate to be increased up to 5 kHz. This limit is imposed by the dead-time of the data acquisition system, as well as damage to the PPAC, which can typically run for less than a week at this rate.

A way to overcome this problem is to partially obstruct the recoils in front of the PPAC, creating mass slits. They cut out undesired mass groups, as well as any scattered beam, but can only allow up to two charge states through to the detectors. If three charge states are transmitted through the FMA, only the central charge state reaches the PPAC. So, to maximise the efficiency when slits are used, the FMA is reconfigured to transmit only two charge states, both of which pass through the slits.

3.3.1 PPAC

The PPAC is a multi-wire proportional counter placed at the focal plane of the FMA. It has thin, 0.8 μm mylar entrance and exit windows, and contains a series grids which, in order downstream, are: cathode, x-position, anode and y-position. The position of a transmitted recoil ion is determined by using delay-line readouts from both ends of the two sets of position grids, giving an R, L, U and D signal which combined give an x,y position. Since the A/Q dispersion occurs horizontally, it is mainly the x-position which allows the assignment of the recoil ion mass to be made. Energy loss information is taken from the cathode, and the anode provides a start signal for a TDC which is stopped by the DSSD signal. This provides the PPAC-DSSD time-of-flight and is used to discriminate between recoils and scattered beam, see Fig. 3.9.

The PPAC is filled with isobutane at 3 Torr, though this pressure is sometimes decreased slightly if the PPAC will be running at high rates (> 4 kHz) to minimise sparking from the grid wires due to radiation damage.

3.3.2 DSSD

The 48×48 DSSD, shown in Fig. 3.6, was designed by the Edinburgh group and produced by Micron Semiconductors Ltd. . It consists of 96 silicon strips arranged orthogonally to provide 2304 'pixels', each pixel identified by its front and back strip number [Sel92]. It is a reversed biased, p-n junction, with the p^+ side on the front, and is biased at -50 V, the depletion voltage being about -15 V. This overbias insures saturation and hence complete charge collection.

The detector is 256 mm^2 and 60 μm thick. The strips are each 16 mm long with an active width of 0.3 mm. Each strip is longer and wider than the stopping distance of any of the charged particles it is designed to detect, i.e. 1 MeV protons with a range of 15 μm, or 5 MeV alpha's with a range of 26 μm. It should be noted that some alpha's may escape out of the front or back of the detector, depending on how deeply the emitting ion was implanted. This issue is dealt with in the next section. Each strip intentionally has too small an active volume to stop most β-particles, for example, a 1 MeV β having a range of about 1 mm. β-particles will deposit less than 100 keV in a DSSD strip before escaping, which is less than the threshold of the amplifiers (which is 300-450 keV depending on the set-up). Being effectively transparent to β's greatly reduces the background, since there are large numbers of β-emitters produced in these experiments, and they would particularly interfere with protons with their low energies of less than 2 MeV. The DSSD is generally cooled to -25^0C, and at this temperature, has an energy resolution of $\sim$ 25 keV FWHM for α particles, which can increase to about 30 keV as the detector incurs further radiation

Figure 3.6: *48×48 DSSD mounted on a plate which forms the end of the detector chamber. The ribbon cables can be seen connecting the front and back sides of the DSSD to preamp boxes mounted on the back of the plate. Feed-throughs of the cooling system for the DSSD can also be seen.*

damage.

Another variety of DSSD was also developed, a 40×40 detector, similar to the 48×48 except with a strip pitch of 1 mm, resulting in a larger area detector with 1600 mm^2, but fewer 'pixels', only 1600. This detector was used in the first experiment which forms the basis of this thesis, and the 48×48 was used in the second. The 40×40 has a greater efficiency in capturing recoils at the end of the FMA due to its larger area, but the smaller number of pixels limits the rate at which ions can be implanted while still retaining long correlation times. However, this is not always a problem if your implant rate is low due to other constraints (e.g. low beam, weak target, fission break-up). It can be noted that a number of the reactions in the second experimental run (described later) had inverse kinematics, focussing the recoils more tightly and offsetting the loss of efficiency due to the smaller area 48×48 detector.

3.3.3 Box and Back Si Detectors

All DSSD experiments have included a large area Si detector placed right behind the DSSD. It is a single, 0.3 mm thick detector, which can detect the 50% of β-particles which escape out of the back of the DSSD. These signals are used to detect β-decay events with the intention of vetoing them, especially β-delayed proton events. The β's do not themselves contribute a large background to the ~1 MeV protons which are being studied. But β-delayed protons, with energies of about 2-5 MeV, do leave a large background, even below 2 MeV as they can escape out of the DSSD (a 3 MeV proton having a range of $\sim$90 μm in silicon) to obscure signals from direct proton emission.

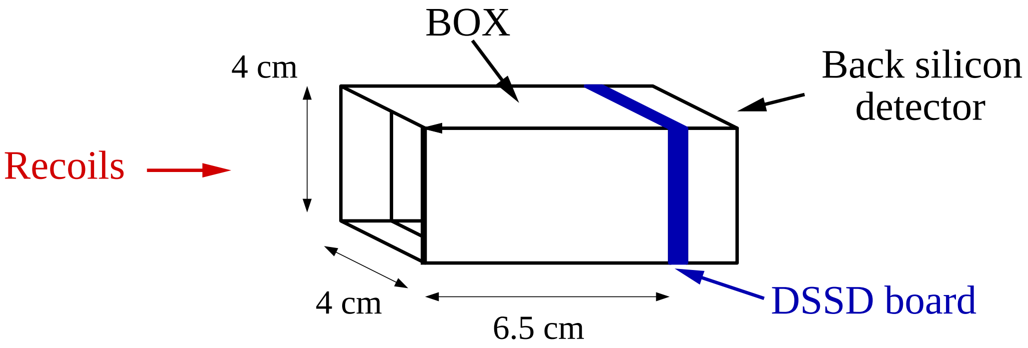

Figure 3.7: *Diagram showing the BOX, DSSD and back Si detectors.*

An example of this is shown in Sec. 4.1 (Fig. 4.1).

Another veto detector that is available is the BOX detector which is mounted in front of the DSSD. It consists of a set of four silicon strip detectors, each with 7 strips, around the front of the DSSD, as shown in Fig. 3.7. As mentioned earlier, recoil ions are generally implanted about 10μm into the DSSD, which means that about a third of the α's can escape out of the front of the DSSD where there is insufficient silicon to stop them. They typically leave about 1-2 MeV background, in the region of interest for proton decay studies, depending on recoil ion implantation depth. The BOX detector was designed to detect these escaping α's, and covers $\sim$75% of the 2π str upstream of the DSSD, in the direction in which the α's can escape. Their escape can be detected and used to veto them, thereby reducing background in the energy region of interest. An example of these various vetoes being used is shown in Fig. 3.10.

The initial function for the BOX when designed was for the reconstruction of these decays, with the energy of escapes detected in the BOX summed with the signal in the DSSD. This would be useful, not just for the $\alpha' s$, but for proton which can also escape from the front of the DSSD, depending on their energy and how deeply the recoil was initially implanted. Unfortunately, this was difficult to put into practice, resulting in very poor energy resolution. The reason was the uncertainty in direction of the escaping particle, and hence the path length and energy loss through the BOX and DSSD. The BOX only has 7 strips along its 6.5 cm length, resulting in course angular resolution.

3.4 Electronics

Signals from the DSSD pass through two preamp boxes mounted on the end plate of the detector chamber, for the p^+ front and n^+ back sides respectively. The signals are then fed to a series of 192 RAL shaping amplifiers [Tho90, Dav90], handling the decays and recoils of both the front and back sides of the DSSD. The shaping amplifiers are mounted in groups of eight on Eurocard motherboards, and produce suitable pulses for use by the ADC, with a rise times of $\sim 1\mu$s and a tail extending a few hundred μs. It should be noted than very fast decay signals ($\leq 10\mu$s) may lie on this tail, and therefore have a higher energy than expected. This can usually be accounted for by using a calibration reaction with a very fast proton emitter (e.g. ^{113}Cs) so that this implant-decay time dependent energy increase for fast decays can be compensated for.

The recoil amplifiers have a low gain ($\sim$ 5) giving a full scale range of 200 MeV. The decay amplifiers have an order of magnitude larger gain, resulting in a 20 MeV full scale range. It should be noted that any DSSD signals pass through both sets of amplifiers, the relevance being that the decay amplifiers are exposed to high energy implantation signals. If recoils are implanted with energies much greater than the maximum acceptable range of the decay amplifiers (~ 80 MeV), they produce a long lived (> 0.5 ms) DC pedestal which renders the decay amplifiers insensitive to decays occurring within this period. It is for this reason that the recoil implantation energy is sometimes decreased by placing a foil in front of the DSSD. The amplifiers are designed to minimise this effect, though modified amplifier cards are available in which the overload recovery characteristics are not as good, but which have lower thresholds (~ 350 keV instead of the usual ~ 450 keV with the electronic setup used).

Two potentiometers on each amplifier card allow pole-zero and DC offset adjustments to be made. A discriminator provides logic pulses for use in timing and the trigger. There is a single potentiometer for each amplifier module to set the discriminator threshold, which results in a common level for each set of eight amplifier cards. This is set as low as practically possible, which is usually ~ 10 mV.

The electronics are available to instrument up to 160 channels from a 80×80 DSSD, which was in development at the time when these experiments were conducted, and has since entered service (see Chap. 5), though in experiments which do not form the core of this thesis. In particular, this has meant that cost savings have had to be made with regards to the electronics, and the recoils are digitised used PTQ's (pulse-to-charge), and then QDC's (charge-to-digital converters). This two stage process may not provide the resolution of single step ADC's, but the modules are cheaper and, as mentioned previously, energy resolution for the recoils is not of prime importance. Analogue signals from the decay amplifiers are fed into Silena and

Philips ADC's for the front and back respectively. The Philips ADC's have better linearity at low energies, of interest in proton radioactivity studies, though not enough are available to instrument both sides of the DSSD.

The data acquisition system used is the MSU/NSCL. A VME system front-end is used, in which the MASTER packs events into buffers and sends them out on an etherlink link to the back-end Alpha computer, where a ROUTER program sends the data as necessary to be written on tape, used in the on-line analysis or displayed on the scalers. When a trigger is accepted by the electronics, the SLAVE reads the required ADC's in the CAMAC crate as well as the clock. The SLAVE software is written in C, and can be modified to accommodate new electronics, as well as various experimental setups and requirements. While this allows the system to be flexible, there is no corresponding standard unpacking routine, which necessitates the need for custom unpacking routines when analysing the data.

The readout time is generally a few hundred microseconds, and decays with implant-decay times less than this are recorded by vetoing the decay busy signal after the electronics common to both implant and decay events are read. After the implant electronics are read, the system checks to see if a decay occurred during the readout, and if so, a 1 is placed in the data stream to indicate a fast event and the decay data is appended on to the implant data. This reduces the effective implant-decay dead-time to $< 10\mu$s compared to the implant-implant dead time of up to 0.5 ms.

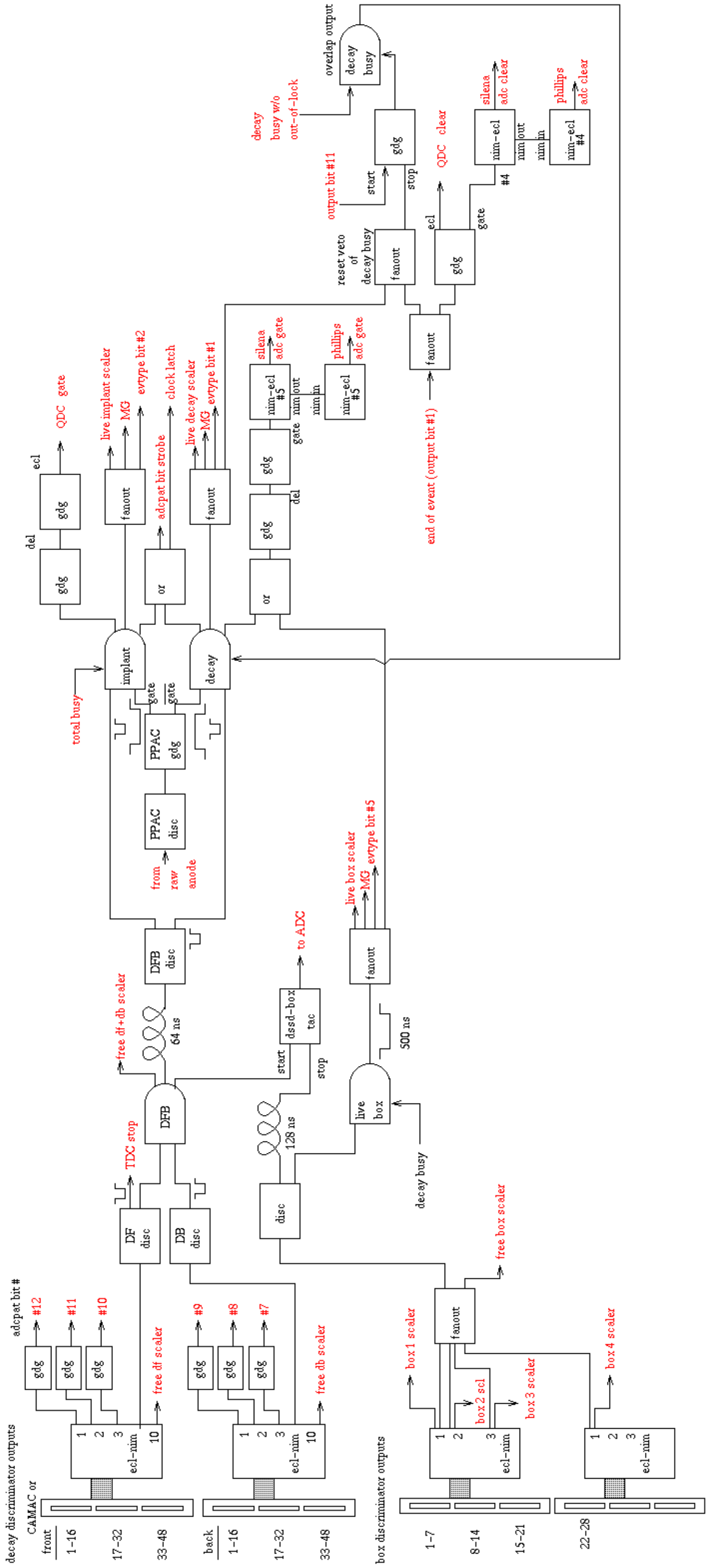

Figure 3.8: *DSSD Logic for implants and decays.*

3.4.1 Logic

The ECL logic signal from each set amplifier module is combined to produce an OR signal for each set of 16 strips, 1-16, 17-32 and 33-48 for the front and the back which forms the ADC hit pattern (each ADC or QDC having 16 channels). A total OR is then produced, first summing all the strips from one side to produce a DF (Decay Front) or DB (Decay back) signal, a coincidence of which (DF.DB) resulting in a valid DSSD event with both a front and back strip firing. The PPAC signal is provided by the anode, and the coincidence or anti-coincidence of the PPAC signal with the DF+DB signal generates the DECAY (event type 1) and IMPLANT (event type 2) signals respectively. These are then used to trigger the acquisition as well as gate the relevant ADCs, including those for the ancillary detectors such as the BOX or back silicon for a DECAY. The clock is also latched, and the relevant event type bit is set in the data stream. Fig. 3.8 shows a schematic of the logic. When the relevant electronics has been readout, the relevent ADCs are cleared, ready for a new event.

3.5 Experimental Setup

Using the FMA setup code [Blu96] and inputting variables such as beam species and energy; target species and thickness; and desired recoil, the initial FMA settings are obtained. A degrader foil thickness is also chosen with this program to insure that recoils that reach the DSSD are implanted with a reasonable energy, as mentioned at the beginning of Sec. 3.3.

Care must be taken initially to insure that the beam does not inadvertently damage a detector or hit a section of the FMA causing radiation damage, since the beam may be hitting, for example, the target frame and scattering. Therefore, the beam is initial set to hit the target with low intensity, and slit are placed behind the PPAC to protect the DSSD if a large amount of scattered beam is transmitted through the FMA, the DSSD being the detector most susceptible to radiation damage. The PPAC spectrum is examined on-line to see how much scattered beam is reaching the focal plane, and therefore whether it is safe to unmask the DSSD. The initial FMA settings default to transmit three charge states of $A > 100$ recoils, but if the charge states on the edge are weakly transmitted, or there is too much scattered beam, the FMA settings are adjusted. Slits can also be placed before the PPAC if scattered beam is still a problem, only allowing the desired mass through to the detectors. The presence of scattered beam can be indicated by, for example, looking at the Energy-TOF data (see Sec. 3.6.1). The main problem with a large amount of scattered beam is that it can damage the PPAC, requiring the beam current to be lowered and hence reducing the sensitivity of an experiment to the exotic nuclei of interest. The slits only allow two masses to be transmitted, either side of the central position of the PPAC, but this is preferable to damaging the detectors with the scattered beam, or running with a very low beam current.

The electronics are tested during this setup period to insure they are working, and once recoils reach the DSSD and are implanted, the response of the decay amplifier to the large implant signals can be observed, and pole-zero and DC offset adjustments made. This minimises the energy resolution loss of decay signals occurring after the saturating implant due to the pole-zero undershoot.

A $^{240}Pu,^{244}Cm$ α-source is used to perform a rough, online calibration, taking into account the DSSD dead layer. The gains and offsets are calculated by computer and implemented on the online analysis and display program; DAPHNE. The online analysis is initially used to check the mass assignments of the peaks seen on the PPAC spectrum, to insure, for example, that if slits are used, they transmit the correct mass through to the DSSD. This will be touched on in more detail in the next section. The QDC pedestals are also observed, and offsets applied online to account for them.

3.6 Data Analysis

Decay and implantation events are treated separately by the sort program, and all vetos and conditions are placed in the sorting software. The only hardware conditions are that for a valid DSSD event (whether implant or decay) at least one front and one back signal has to be detected. Unfortunately, a few multiplicity zero events are still observed, perhaps due to pickup in the DSSD electronics providing false trigger. The only other hardware condition is PPAC-DSSD coincidence which identifies implantation events, with anti-coincidence signifying a decay event. Fast decay events are treated as both, with the initial implantation information analysed by the relevant routines in the sort program, and the decay information as a decay event. Note, that with these events, the decay occurs after the implantation.

3.6.1 Implantation Events

Initially, the strip multiplicity is checked to insure a front and back signal was received, and then, if strip multiplicity was greater than one, the front and back strips with the largest signal were used in the analysis. No gain matching was done with the implant energies since a good energy resolution isn't necessary for the analysis. The implant data includes the PPAC information which is analysed. This is done to distinguish recoil ions with scattered beam particles by, for example, looking at the energy time-of flight spectrum, Fig. 3.9. Beam particles, with their lighter masses and larger angular and energy dispersion, can be distinguished from recoils and therefore vetoed. Another option is to look at the ΔE-E characteristics of the implants, since scattered beam ions generally have higher energies and therefore have smaller ΔE signals in the PPAC.

When the sort program sees a valid implant event, it's time and PPAC x position are stored in an array, referenced by front and back strip number to identify the pixel into which it was implanted. This is then correlated with decays occurring in that pixel prior to the next implanted recoil in the pixel.

3.6.2 Decay Events

The first software condition placed on decay events is that only one front, and one back strip fired. Generally, this accounts for 90-99% of the decay events, depending on the specific experimental run. Higher multiplicity events are generally caused by charge sharing effects between adjacent strips, and hence their full decay energy is not collected.

The decays are then gain-matched using a calibration reaction such as $^{78}Kr(362.5MeV) +^{92} Mo \rightarrow {}^{167}Ir + p2n$ which was used at ANL in 6/2000 during an experimental run which forms the bulk of this thesis. The first condition on all decays is to check that they aren't implants. While implants

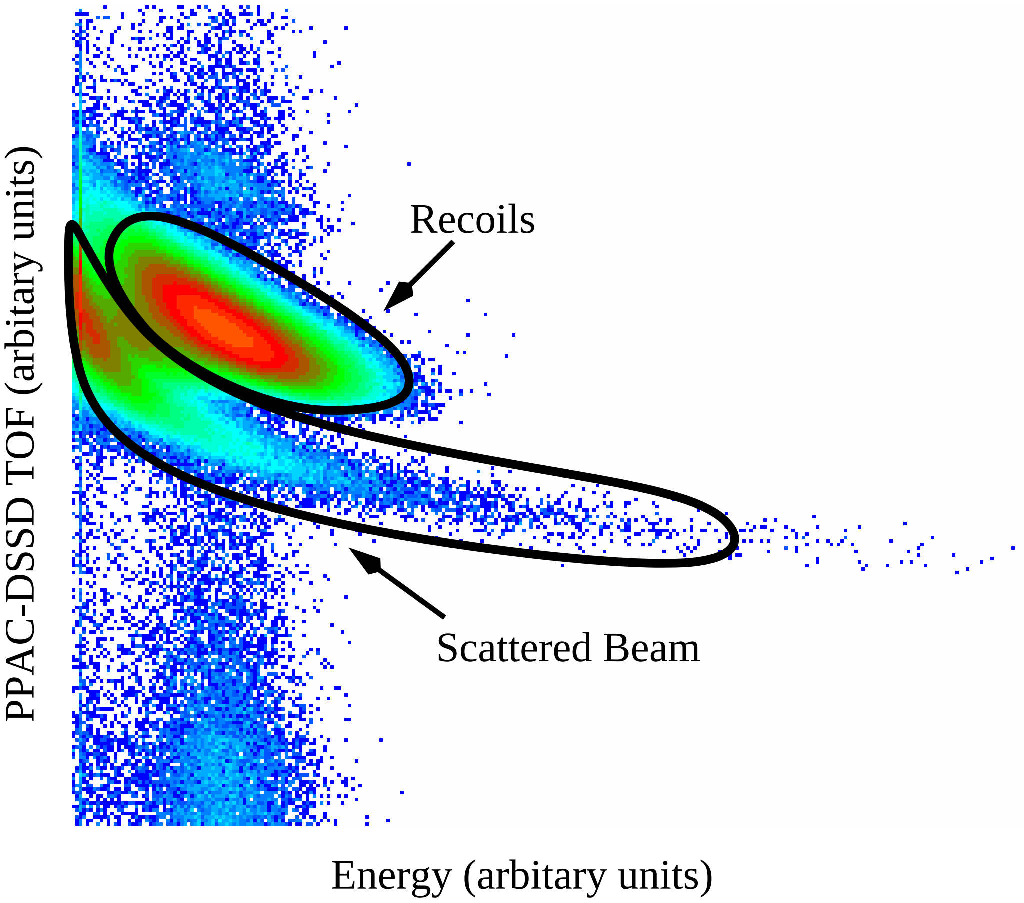

Figure 3.9: *Spectrum showing implant energy versus PPAC-DSSD time-of-flight.*

and decays are discriminated by PPAC-DSSD coincidences in the electronics, sometimes the PPAC anode, which provides the PPAC trigger signal to the electronics, does not fire, and when the recoil is implanted in the DSSD, the event is recorded by the electronics and acquisition as a decay. To counter this possibility, during a decay, the PPAC cathode ADC is read to see if a signal was present here (the cathode providing ΔE information), and packed with the decay event info. If a PPAC ΔE signal is present, the decay event is rejected as an implant by the sort program. Then a condition of strip multiplicity being equal to one is introduced and a decay spectrum is obtained, as shown in black in Fig. 3.10(a). This spectrum is calibrated using known proton and α-decays. The proton calibration for this experimental run was performed using the known transitions, ^{167}Ir, ^{167m}Ir and ^{165}Ir which were also observed during the course of the experiment, during the search for ^{164}Ir. In this case, three proton lines could provide a reasonable proton energy calibration, the many known α-lines providing many reference points for a calibration for α's.

Generally, the proton calibration is not straightforward, due to the low production cross-section of proton-emitting isotopes when compared to known α-emitters. Usually, the time allocated only allows one proton-emitter to be produced in the calibration reaction, and α lines also have to be included as calibration points. But protons and α's behave differently in silicon detectors, and there is a small pulse-height defect between them, with the ratio of the pulse heights between protons and α's of the same energy being $p/\alpha = 0.986(2)$ [Len86, Pai81]. Another factor that has to be taken into account is the recoil energy of the emitting nucleus. All these decays take place internally in the DSSD, so no dead-layer has to be accounted for, but

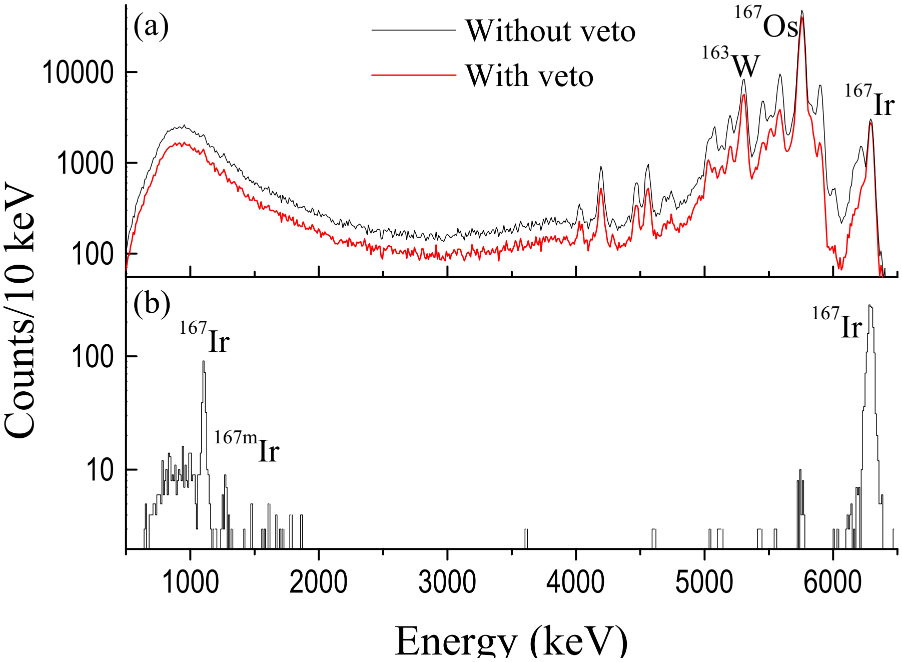

Figure 3.10: *Figure showing decays occurring within the DSSD from the reaction of a 362.4 MeV* ^{78}Kr *impinging on a 1.14* mg/cm^2 ^{92}Mo *target. (a) Shows all decays with (in red) and without (black) veto conditions such as equal energy in the front and back strips, and signals from the BOX and back Si detectors. (b) Now shows decays occurring within 200 ms of an A=167 implant, followed by a second decay in the same pixel within 1.8 s.*

the recoiling nucleus does deposit its energy in the detector. But again only with a caveat, since only about 28% of the energy of the recoiling nucleus contributes to the charge collected by the silicon detector [Hof82b, Hof89a]. This is because the electron-hole pairs are created in such a high density around the dense nucleus that some pairs are partially screened and recombine before they can be collected. Another option is that with the larger nuclear mass, the recoiling nucleus deposits some of its energy by interacting with the atoms in the lattice, displacing them, which results in energy loss that is not sensed by the detector in terms of collected charge. One also has to account for the recoiling nuclei of different particles possessing different ratio's of the energy: $1/A-1$ and $4/A-4$ for protons and α's respectively. These considerations have all taken into account, where necessary, when producing the proton energy calibrations used in the work described in this thesis.

A number of vetos and conditions can be implemented to clear up the spectrum. One condition requires equal energy signals between the front and the back strip, decay events with an energy difference of more than 50 keV being rejected. Vetoes from the back Si and BOX detectors (described in Sec. 3.3.3) can also be implemented to reject most of the escape α's, and some of the β-delayed protons. These constitute most of the background below 4 MeV, though in this region most of the background is escape α's, as seen in the hump at 1 MeV. This results in the spectrum seen in red in Fig. 3.10(b). The energy resolution for α's is generally about 30 keV.

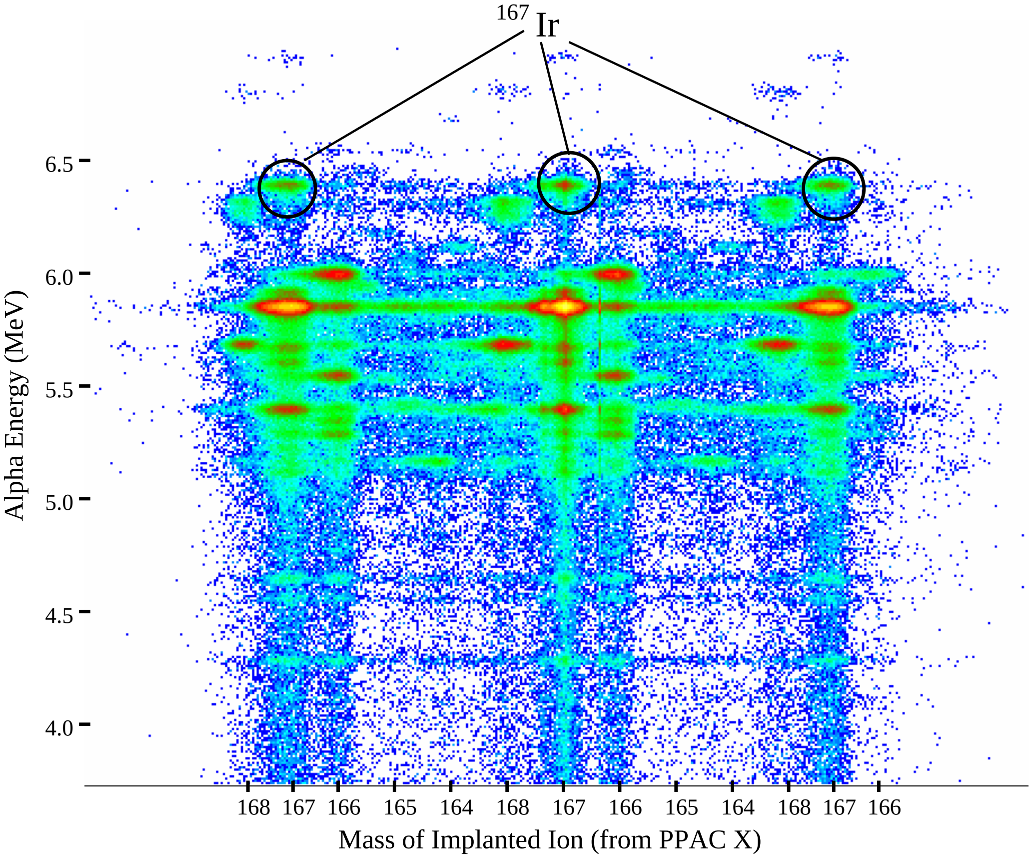

Figure 3.11: *DSSD decay energy versus PPAC x position of the previously implanted ion, which yields the mass of that ion. Note the known α decay of ^{167}Ir identifies the position of the A=167 recoils in the PPAC.*

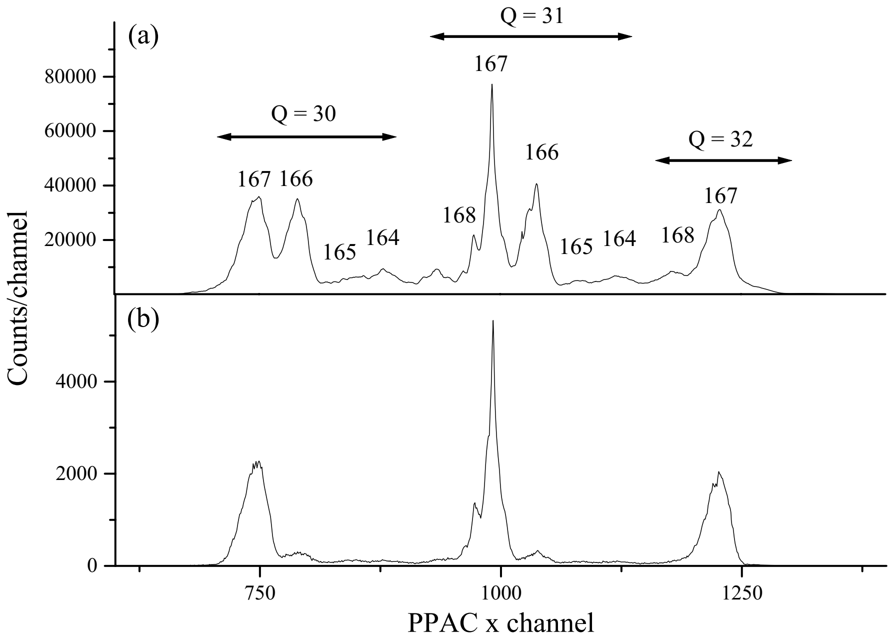

Figure 3.12: *Spectrum showing PPAC x position and the corresponding masses associated with the positions. (a) Shows all position of all recoil ions which were implanted in the DSSD. (b) shows the PPAC position of recoils which were immediately followed by an* ^{167}Ir *α-decay. This helps to identify which peaks correspond to which mass.*

3.6.3 Decay Assignments

The implantation rate per pixel (~ 1 per second) is set to be long compared to the half-lives of the decays of interest (e.g. α half-lives of < 100 ms). So as along as the implant-decay times looked at are less than the average time between implantations, one can confidently assign decays occurring within a certain time of an implant, to that recoil. Mass assignments of decays are made by looking at the PPAC x position of this implanted ion. The sort program looks at the recoil array, referenced by the front and back strip numbers, for the preceding implant in the same pixel and obtains the implant time and PPAC x position of the recoil. The PPAC x position of the recoil can be plotted against, for example, the energy of the decay occurring in the same pixel as a recoil was implanted, as in Fig 3.11, where one can see the known decay of ^{167}Ir. Once the decay energy is calibrated, strong, known decays will identify the masses occurring in the peaks of the PPAC x position spectra, as shown in Fig. 3.12, where the decay of ^{167}Ir denotes the position of the A=167 mass group. This is initially done with a standard calibration reaction, to calibrate the PPAC, i.e. determine the center of the PPAC in terms of the mass spectrum, as well as provding known decays for the energy calibration.

Decays can also be identified by using time gates which are usually 2-5 times the half-life of the nucleus in question. Spectra with short time gates will preferentially show decays from nuclei with short half-lives. The implant-decay time, or decay-decay time for a daughter nucleus, can yield the mean lifetime of the nucleus, and hence its half-life. Decay-decay correlations can be used to assist in identifying unknown decays, which can be followed by

α-emitting daughters that decay with characteristic half-lives and energies. An example of this is shown in Fig. 3.10. The red line in Fig. 3.10(a) shows the total decays occurring in the DSSD after various vetos have been enabled to reduce the background. Then a number of conditions are enacted, asking for a decay to occur within 200 ms of an A=167 implant, and be followed by another decay within 1.8 ms, the resulting spectrum shown in Fig. 3.10(b). The 200 ms time gate is about 6 times the half-life of ^{167}Ir, and the daughter from its proton decay, ^{166}Os, has a half-life of 181 ms, which falls well within the 1.8 s time gate for a second decay to occur, as does the half-life of the α-daughter, ^{163}Re. Therefore, all the ^{167}Ir decays can be seen. Tighter conditions, for example on the energy of a daughter decay, would result in being able to select specific decays with a high degree of confidence, as will be shown in the next chapter.

Chapter 4

Results and Discussions

The results presented in this thesis are from several experimental runs performed in two batches at Argonne National Laboratory in 2000. These experiments were analysed by myself and will be described in this chapter. The first run, in which the proton emitter ^{117}La was observed, took place in June 2000, while the second set of runs in September/October 2000 successfully observed three, odd-odd, proton emitters, ^{130}Eu, ^{164m}Ir and ^{170m}Au. The results from ^{117}La, presented here, are published in [Mah01]. The results from the odd-odd proton emitters were included in an oral presentation at ENAM 2001, the 3rd International Conference on Exotic Nuclei and Atomic Masses in Hämeenlinna, Finland. This presentation has been published in EPJA [Mah02a], and the results will also submitted to PRC in a larger paper [Mah02b]. Data from proton radioactivity studies will also be used to confront predictions from the mass models described in Sec. 2.4. A summary of the proton radioactivity experimental runs performed at Argonne in 2000 that form the core of this thesis is shown in Table 4.1.

As an aside, further analysis on data from an experiment at ANL in

Table 4.1: *Details from the proton radioactivity experimental runs described in this chapter.*

Nuclide	Beam	Target
^{116}La	325 MeV, 3.5 pnA ^{58}Ni	^{64}Zn 730μg/cm^2
^{117}La	295/310 MeV, 3.0 pnA ^{58}Ni	^{64}Zn 730μg/cm^2
^{126}Pm	432 MeV, 3.5 pnA ^{78}Kr	^{54}Fe 751μg/cm^2
^{130}Eu	432 MeV, 3.5 pnA ^{78}Kr	^{58}Ni 425μg/cm^2
^{164}Ir	437 MeV, 4.0 pnA ^{78}Kr	^{92}Mo 773μg/cm^2
^{170}Au	400 MeV, 4.5 pnA ^{78}Kr	^{96}Ru 513μg/cm^2

1996 will also be presented. This includes measurements made on the α-emitting nucleus, ^{162}Os and its daughter, ^{158}W. The results on these nuclei were published in [Mah00].

4.1 Proton Radioactivity from ^{117}La

During 1999, the Legnaro group in Italy observed the new proton emitting isotope, ^{117}La, initially presenting their results in PROCON‘99 [Sor00]. A 1.5 pnA beam of 319 MeV ^{58}Ni on a 1 mg/cm^2 thick target of ^{64}Zn was used to create the $p4n$ nucleus, ^{117}La, which was initially reported to have a 783(6) keV proton emission line, and $t_{1/2} = 20(5)$ ms. This decay rate could not be reproduced using spherical calculations, indicating that, like ^{113}Cs or ^{131}Eu , ^{117}La was a deformed proton-emitter, with Möller *et al.* predicting a deformation of $\beta_2 = 0.29$. This result was therefore of interest to the theoretical community (see Chap. 2).

The group at Legnaro used a recoil mass separator as well as a setup at the focal plane similar to that successfully employed at Argonne, with a PPAC transmission detector and a 40×40 DSSD. Unfortunately, there were a number of experimental difficulties, including electronic noise. Also, while the x strips in the DSSD were fully instrumented, with position and energy information for each strip, the y strips were chained together with a delay-line, and only position information was obtained in this plane. But problems with the electronics registering the low-energy proton signals precluded this position information being obtained for the y direction, hence correlations could only take place within each x strip, resulting in only 40 'pixels' instead of 2000.

The general interest of the community in these results, coupled with experimental difficulties of the first observation, indicated that an independent verification of these results would be a profitable first experiment for the proton collaboration at the FMA after the removal of Gammasphere in 2000.

4.1.1 Experimental Details

In this experiment, the 60 μm thick, 40 DSSD was used, with a back silicon detector placed immediately behind it to veto some β-delayed protons. No BOX was emplaced in front of the DSSD.

All of the reactions undertaken in this experimental run used a ^{58}Ni beam. For the calibration reaction, proton lines from ^{147}Tm and its isomer ^{147m}Tm were obtained using a 261 MeV ^{58}Ni beam on a 773μg/cm^2 thick ^{92}Mo target. A number of known α transitions were also obtained, some from isotopic contaminants in the ^{92}Mo target. The α and proton lines were used in the calibration, taking into account the various factors such as pulse-height defect, etc. mentioned in Sec. 3.6.2.

The main experiment consisted of the ^{58}Ni beam impinging on a 730

μg/cm^2 thick ^{64}Zn target to produce the compound nucleus, ^{122}Ce. Initially, to adhere as closely as possible to the conditions of the Legnaro experiment, the same beam energy of 310 MeV was used, producing a center-of-target excitation of 90 MeV. The beam energy was then decreased to 295 MeV, producing a center-of-target excitation of 82.5 MeV, which was the optimum energy, predicted by HIVAP [Rei81], for the production of the $p4n$ evaporation channel, yielding ^{117}La. A 2.16 mg/cm^2 aluminium degrader foil was placed in front of the DSSD to reduce the energy of the recoil ions when they were implanted in the DSSD to under 40 MeV. The FMA was set to E=121.5, Q=26.5 and A=117, with slits positioned to only transmit A=117 recoils that had a charge states of 26^+ and 27^+. This was done to reduce the implantation rate from recoils with other masses, particularly since the beam current was increased to a mean intensity of $\sim$ 3 pnA. At this beam current, the DSSD implant rate was about 1 KHz, the PPAC rate about twice that of the DSSD.

A search for the odd-odd proton-emitting partner, ^{116}La, was also undertaken, with HIVAP predictions indicating that increasing the beam energy to 325 MeV would be optimum for the production of ^{117}La. The new FMA settings where E=127, Q=27.5 and A=116. The experimental run ended with a calibration using the α-source to check for strips which may have shifted in gain over the course of the experiment.

4.1.2 Decay of ^{117}La

All the decays that occurred in the DSSD are shown in Fig. 4.1(a). All the usual conditions have been enacted, as described in Sec. 3.6. Slits

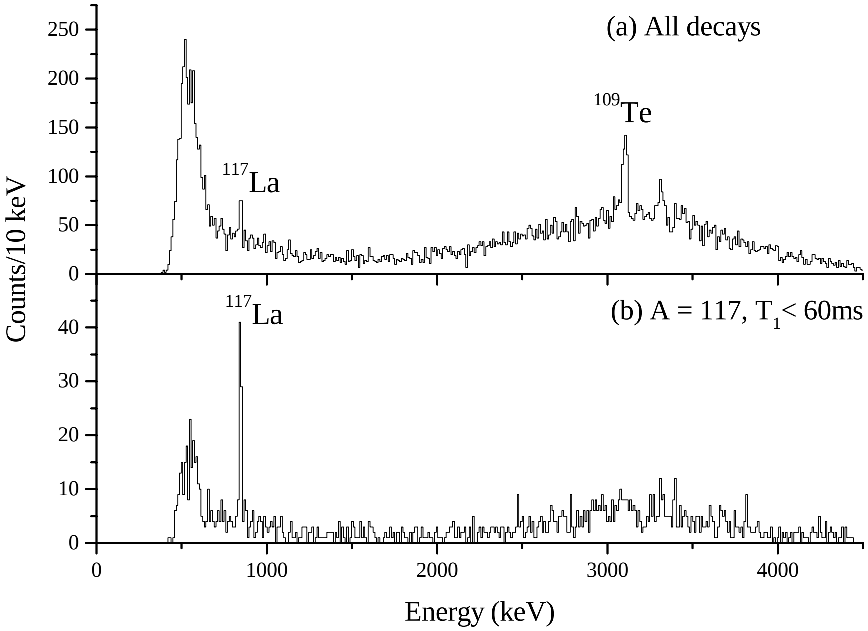

Figure 4.1: *Decay energy spectrum of all decays occurring within the DSSD and below 4.5 MeV, for both the 295 and 310 MeV ^{58}Ni beam bombarding a ^{64}Zn target for a combined total of 24 hours with: (a) no time gate, and (b) a 60 ms time gate.*

were positioned to insure that mainly A=117 recoils entered, but this does not preclude recoils with other masses entering the DSSD through, for example, charge state ambiguities as with the α-emitting nucleus, ^{108}Te where $108/24^{+} \simeq 117/26^{+}$. α-decay from ^{109}Te was also observed.

The background is mainly due to β-delayed protons, the hump around 3 MeV being delayed protons which have managed to deposit most of their energy within the DSSD. The background from escapes forms a continuum through most of the spectra, but in particular, the large background at 500 keV is from escapes through the front of the DSSD. The background present in Fig. 4.1 is what remains after 50% of the β events which are vetoed by the large back silicon detector. There are almost no other known direct α or proton emitters in the region accessed by the reaction; $^{58}Ni+^{64}Zn \rightarrow ^{122}Ce^{*}$.

A time gate requiring decays to occur within 60 ms of a recoil being implanted within the same pixel results in the spectrum shown in Fig. 4.1(b). Here, a peak can be seen at 800 keV, this low energy indicating it was from direct proton emission. A half-life of $t_{1/2} = 24(3)$ ms was obtained for this transition, using the method of maximum likelihood, mainly used for situations with relatively low statistics [Bev92, Sch84]. Utilising the nearby ^{147}Tm proton lines, at 1051.0(33) and 1110.8(39) keV, for the calibration, an energy $E_p = 806(5)$ keV was obtained for the observed transition, equivalent to a $Q_p = 813(5)$ keV for ^{117}La. It should be noted that the result from the runs at both energies are combined to produce the spectra shown. The cross-sections of the peak in the runs at both energies were found to be similar, 240 nb (310 MeV) and 230 nb (295 MeV), with a factor 2 uncertainty. HIVAP cross-section predictions for these two energies are 150 and 400 nb respectively. This in good agreement with the results from Legnaro, $\sigma \sim 200$ nb [Sor01]. There is a combined total of about 100 counts over a runtime of 24 hours with two charge states transmitted through the FMA.

^{117}La was one of the few proton emitting candidates in this region, the other being ^{116}La, see Sec. 4.1.3. Other A=117 candidates are predicted to have lower cross-sections at these energies, such as ^{117}Ce which is predicted by HIVAP to have a cross-section three orders of magnitude lower than ^{117}La, as well as being only slightly 2 proton unbound [Abo95]. Other A=117 isotopes such as Ba or Cs are 1p and 2p bound [Abo95, Mol97]. Therefore, the assignment to ^{117}La can be made on the basis of the recoil mass selection for A=117, supported by the half-life and cross-section being in good agreement with the results seen in Legnaro [Sor01].

The $g_{7/2}$ and $d_{5/2}$ proton orbitals are expected to lie near the Fermi surface in this region. WKB calculations using the real part of the Becchetti-Greenlees optical potential [Bec69] give proton partial half-life predictions of $t_{1/2,p}$ = 86 ms for a $\pi g_{7/2}$ configuration and 234 μs for a $\pi d_{5/2}$ configuration. The $g_{7/2}$ configuration can be ruled out since it implies an unphysical spectroscopic factor well in excess of unity. The $d_{5/2}$ spectroscopic factor implied by this analysis = 0.01. This very low value indicates that the transition is unlikely to be understood as occurring from a pure spherical shell model configuration. One can also note that ^{117}La has been predicted to be deformed [Mol95, Abo95], providing further indication that, as with $^{112,113}Cs$, deformation may play an important role in understanding its decay.

Calculations of the decay rate for ^{117}La were performed using the adiabatic approach described in Sec. 2.6.1, which was very successful in explaining the decay rates of the deformed proton emitters ^{131}Eu, ^{141}Ho, and ^{141m}Ho. The interaction between the quasi-bound proton and the deformed core includes deformed nuclear, spin-orbit, and Coulomb terms, with the parameters given in Appendix A of [Esb00]. The depth of the nuclear potential was adjusted to reproduce the experimental energy, corrected for recoil and atomic screening effects. Candidate deformed orbitals which may lie near the Fermi surface include $3/2^+[411]$, $3/2^-[541]$, and $1/2^-[550]$. $K = 3/2^+$ was favoured as the ground state for the nearby proton emitter, ^{113}Cs, for a deformation of $\beta_2 \sim 0.2$ [Bug89, Mag98]. Note that in the strong-coupling limit, used here, $K = \Omega$ are good quantum numbers [Rin80].

Fig. 4.2 shows the predicted proton decay half-lives for these spins,

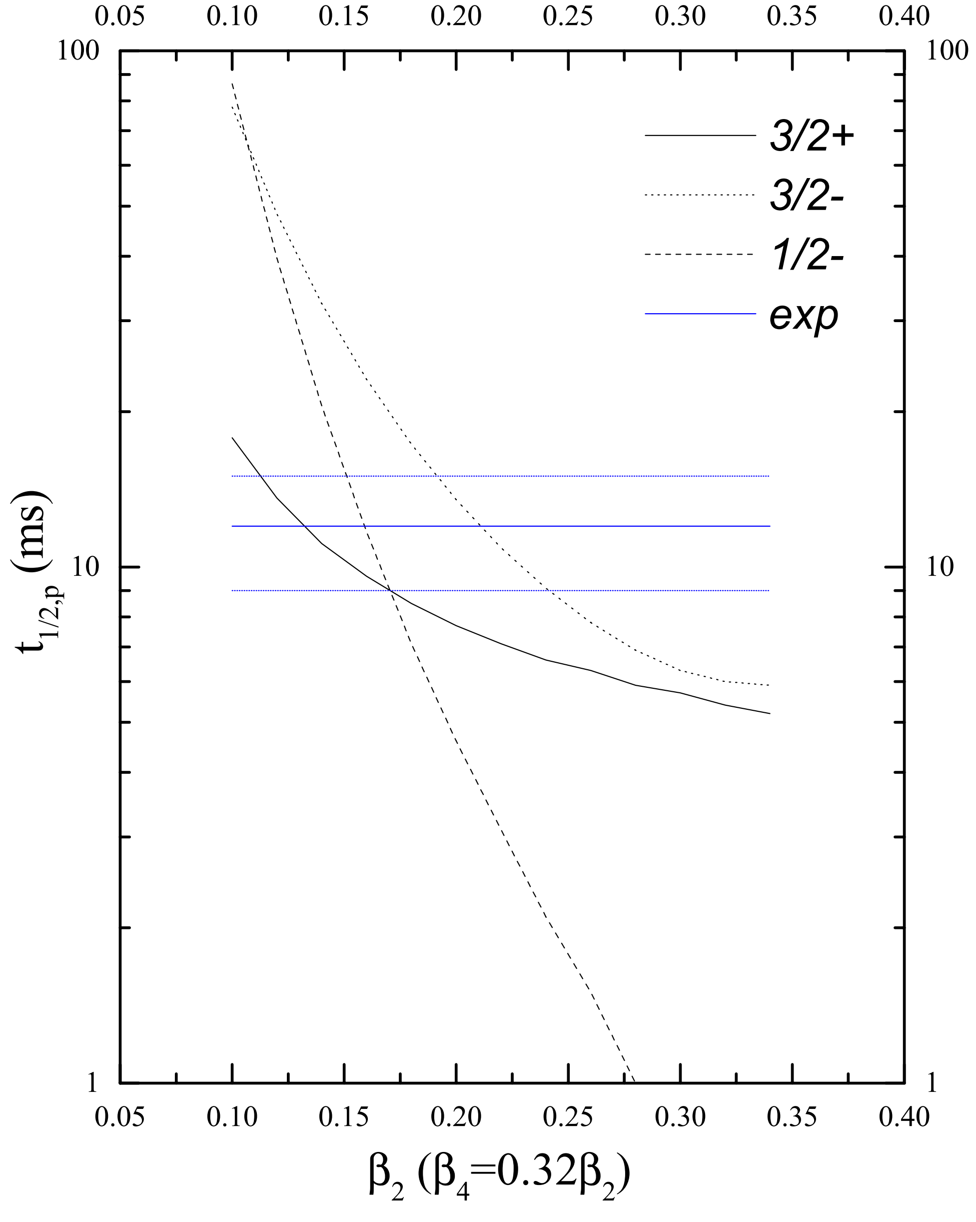

Figure 4.2: *Calculated proton partial half-lives for* ^{117}*La, for spins of* $1/2^-$, $3/2^+$, *and* $3/2^-$. *The horizontal coloured lines represent the experimental value with uncertainties and are folded with the theoretical prediction for the spectroscopic factor of 0.5.*

plotted as a function of β_2, with the corresponding value of β_4 set to $0.32\beta_2$. Smith *et al.* [Smi98] have extracted β_2-values of 0.24-0.27 for $^{124,122,120,118}Ba$ from experimental 2^+ excitation energies. These are consistent with the predictions of Möller *et al.* [Mol95] for these even-even neutron-deficient Ba isotopes. Möller *et al.* [Mol95] predict deformations for the daughter nucleus ^{116}Ba of $\beta_2 = 0.28$ and $\beta_4 = 0.09$, and a ^{117}La ground-state spin of $3/2^+$. At this deformation, $K = 3/2^-$ and $K = 1/2^-$ are also expected to be close to the Fermi surface. Thus, for deformations $\beta_2 > 0.2$, as we expect is the case for ^{116}Ba, the $K = 1/2^-$ option for ^{117}La appears to be ruled out. Under these circumstances, Fig. 4.2 suggests that the ground-state spin of ^{117}La is either $3/2^+$ or $3/2^-$. BCS spectroscopic calculations (Sec. 2.7.2) in this region are complicated by the need to calculate a large number of single-particle energies for all the deformed levels present near the Fermi surface. An approximate theoretical spectroscopic factor for the ground-state decay of $S_p^{th} \sim 0.5$ can be used, as has been used for a number of other deformed proton emitters in this region [Mag99, Mag00], reflecting the proximity of the Fermi surface to the proton emitting orbital [Bug89]. The actual experimental spectroscopic factors obtained using $\beta_2 = +0.28$ and $\beta_4 = +0.09$ [Mol95] are 0.23(5) and 0.27(6) for $K = 3/2^+$ and $K = 3/2^-$, respectively, with the uncertainties reflecting experimental half-life and proton energy uncertainties. One can see that $K = 3/2^-$ seems the most likely state, though with the uncertainties included, one cannot totally exclude $K = 3/2^+$. One can also note that the deformation may not be exactly $\beta_2 = 0.28$, which would change the experimental spectroscopic factor, with better agreement between the experimental and calculated proton half-lives to be found at more moderate deformations ($0.21 \lesssim \beta_2 \lesssim 0.26$), i.e. closer

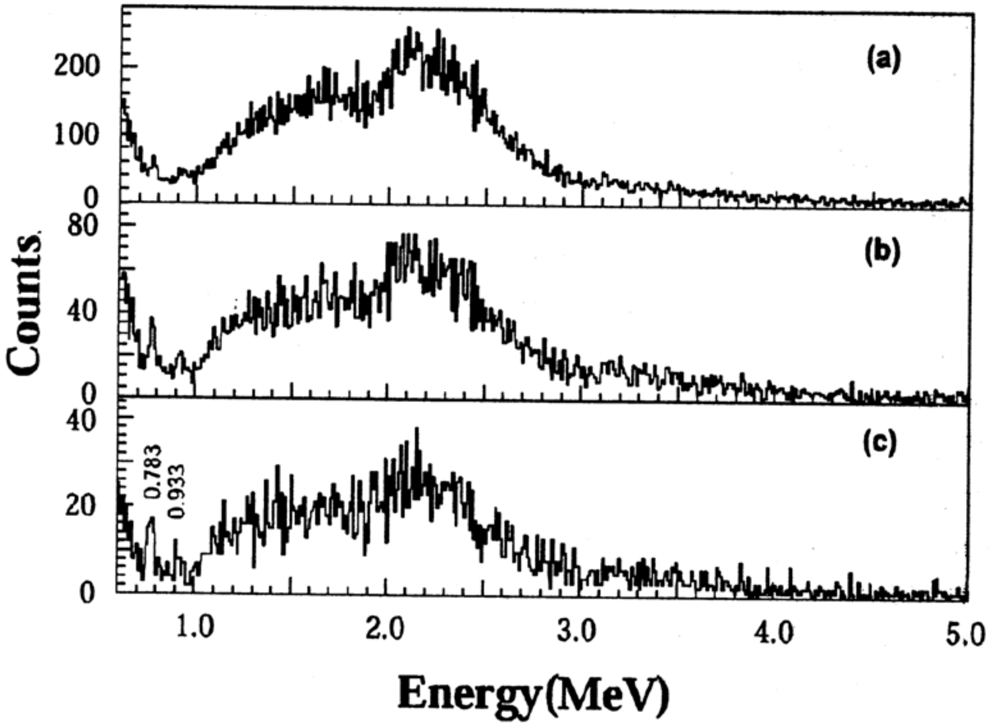

Figure 4.3: *Decay events collect in the DSSD during the 310 MeV* $^{58}Ni + ^{64}Zn$ *run. (a) shows all the decays. (b) displays decay events occurring in a 100 ms time interval after a recoil implantation in a given strip. In (c) an additional condition* $A/q = 117/30^+$ *for the recoils is required. These spectra are from Soramel* et al. *[Sor01] and are displayed for comparative purposes.*

to the deformation of ^{113}Cs.

For either spin, the branching ratio for decay to the 2^+ state of the daughter nucleus is expected to be too small to be observed, since the excitation energy is expected, using Grodzins formula [Gro62] for example, to be $\sim$ 200 keV or higher. An experimental limit of $\lesssim$ 25% is placed on any possible fine-structure decay branch in the ground state of ^{117}La.

4.1.3 Comparison with Legnaro Results

A comparison with the results from Legnaro can be made, with Fig. 4.3 showing the spectra from Soramel *et al.* [Sor01]. The cross-section of 240 nb obtained in this experiment is in good agreement with that of Legnaro, 200 nb. It should be noted that while a thinner ^{64}Zn target was used in the Argonne run, $0.73mg/cm^2$ instead of the $1mg/cm^2$ used at Legnaro, the excitation at the center of target was no more than 2 MeV lower, with the 310 MeV beam. This would be unlikely to cause a large change in the cross-section. The half-lives were also consistent, at $t_{1/2} = 24(3)$ ms for ANL and $t_{1/2} = 20(5)$ ms at LNL.

There is some disagreement with the energies, LNL having measured a lower energy of $E_p = 783(6)$ keV, as opposed to $E_p = 806(5)$ keV observed at Argonne. All one can say is that the calibration used in this work only used transitions occurring within the DSSD from the calibration reaction, in comparison with Legnaro where external α's were used. Various effects previously mentioned, such as recoil energies and pulse height defect, were also accounted for in the ANL analysis. The presence of α-lines from ^{108}Te and ^{109}Te during the run provide another verification of the calibration. An external α calibration performed at the end of the run insured that no measurable gain shifts occurred during the experiment. A FWHM of 17 keV was obtained for the ^{117}La peak, for which we had greater statistics than Legnaro, as indicated by the more precise energy and half-life values. One can also observe that the background is generally lower in the experiment performed at ANL, as shown in Fig. 4.1. It should also be noted that our experiment encountered none of the difficulties with noise mentioned in the

Legnaro experiment, and that our DSSD was fully instrumented, the Legnaro group only being able to fully instrument the vertical strips.

The ground state peak of ^{117}La was assigned to the $K = 3/2^+$ state, with $\beta_2 \sim 0.3$, using the formalism by Maglione *et al.* [Mag99]. They state an experimental spectroscopic factor of $S_{exp} = 0.6(1)$ for deformations $\beta_2 = 0.2 - 0.4$, this difference in spectroscopic factor mainly due to the different experimental energy used in the calculation.The $3/2^+$ state was a strong candidate for ^{117}La with calculations performed at ANL.

The other major discrepancy between these sets of results is the observation by Soramel *et al.* of a second, higher energy peak which they assign to a $9/2^+$ isomeric state ^{117m}La [$E_p = 933(10)$ keV, $t_{1/2} = 10(5)$ ms]. A cross-section of a third that of the main peak is stated for the isomer, which would be 67 nb. However, the results presented in this thesis show no sign of any second peak. Fig. 4.1(b) would show any 10 ms state with a reasonable cross-section. The background is much smaller than that of LNL, and the statistics in the main peak larger. A cross-section limit on any peak with a 20 μs $\leq$ t$_{1/2}$ $\leq$ 100 ms is set at 5 nb, a factor of twenty lower than that observed at Legnaro. If this state was present, with the properties reported by Soramel *et al.*, it should have been clearly visible in this experiment, and its non-observation here casts grave doubts on its existence as reported in [Sor01].

4.1.4 Search for ^{116}La

In the same experimental run in which ^{117}La was observed, a search for ^{116}La was undertaken using a 325 MeV ^{58}Ni beam on the same, 730 μm/cm^2, ^{92}Mo

target. The beam energy was, again, that indicated by a HIVAP calculation as yielding the largest production cross-section for the $p5n$ evaporation channel, approximately 10 nb. The FMA was set to A=116.5, Q=27.5 and A=116.5 to transmit two charge states of mass 116 recoils through the FMA, with slits in place. Sample spectra are shown in Fig. 4.4. One can see that some ^{117}La was able to pass through the slits, as part of the tail of a neighbouring mass peak.

^{116}La is the odd-odd partner to ^{117}La and is predicted by Möller *et al.* and Liran-Zeldes to have a S_p that is 130 keV [Mol97], or 300 keV [Lir76], larger than that of ^{117}La, which has $S_p = 813(5)$ keV. This would indicate that ^{116}La would emit a 1 MeV proton, which would mean it possessed a half-life $\sim 300\mu$s, assuming ^{116}La was spherical and the proton came from a $g_{7/2}$ orbital. As ^{116}La would probably be deformed like ^{117}La ($\beta_2 = 0.28$ [Mol97]), one possible situation could be that exhibited by the cesium proton emitters where ^{112}Cs, the odd-odd nucleus further away from stability, had a proton decay energy value which 150 keV lower than ^{113}Cs which lies closer to stability. If this was true with ^{116}La, it might explain why proton decay was not observed from this nucleus, since ^{116}La would have to have a Q_p of at least 700 keV to be observable, or it wouldn't be fast enough to compete with β-decay. Discovering conclusively what the actual case was in this example would be of great interest. ^{116}La could also provide another example to confront deformed proton decay theory with.

Once again, we see the strong dependence of proton decay half-lives to energy. If ^{116}La has too low an energy, it will either have too long a half-life to compete with β-decay, and perhaps a small or negligible proton branch. If the energy is too high, its will decay before the electronics have recovered

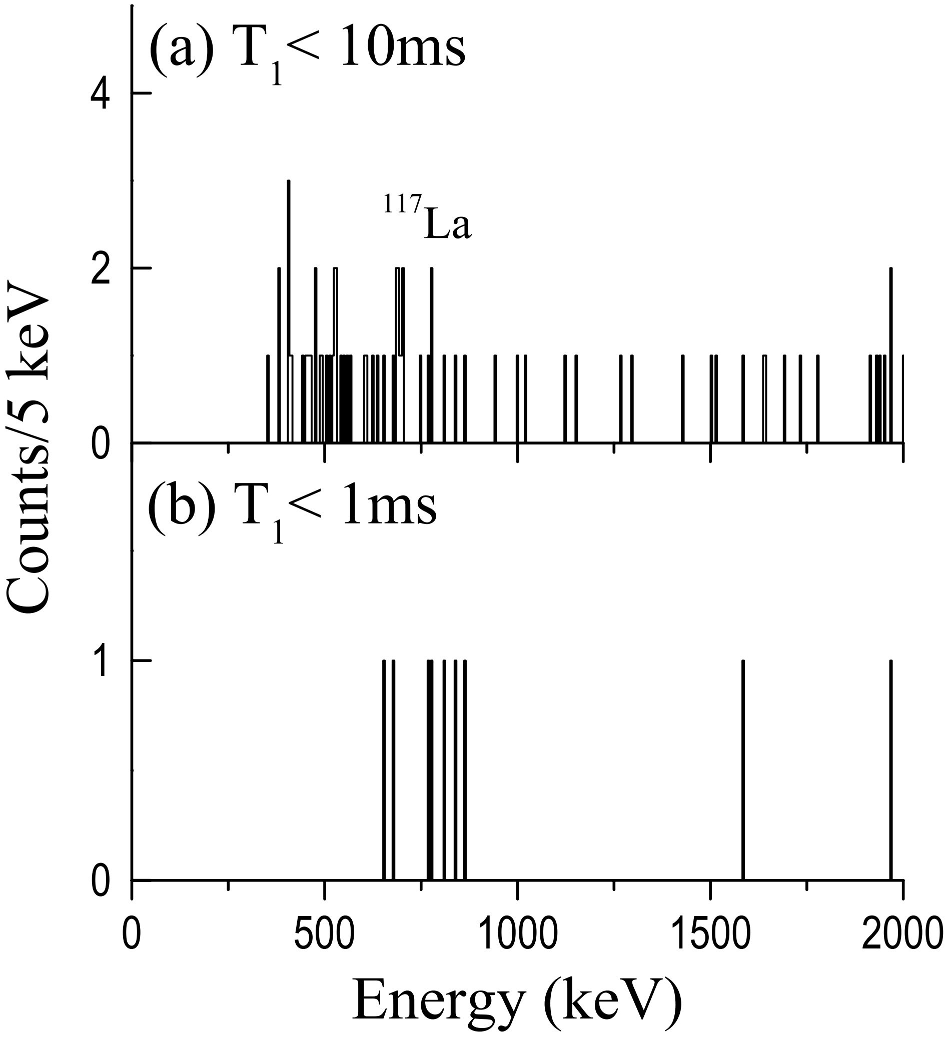

Figure 4.4: *Decay energy spectrum of all decays occurring within the DSSD and below 2 MeV, for a 325 MeV* ^{58}*Ni beam bombarding a 730* $\mu g/cm^2$ ^{64}*Zn target for a total of 1.5 days, within: (a) 10 ms of an implantation, and (b) 1 ms of an implantation within the same pixel.*

from the high energy implant signal, and therefore not be detected by our experimental setup.

After 29 hours running with a 3.5 pnA beam, a cross-section limit of $\sim$ 5 nb is placed on ^{116}La for proton decay with half-lives 20 μs $\leq$ $t_{1/2}$ $\leq$ 20 ms. Another $p5n$ proton emitting isotope, ^{140}Ho, has been successfully produced with a cross-section of 13 nb, so the cross-section limit placed on ^{116}La represents a reasonable limit for a meaningful search. The $p5n$ channel nuclei seem to have a cross-section over an order of magnitude lower than $p4n$ nuclei such as ^{141}Ho ($\sim$ 200 nb) and ^{161}Re ($\sim$ 150 nb). Of course the other options mentioned, of too short or too long a proton partial half-life, are still present as explanations for the non-observation of ^{116}La.

4.2 Search for Odd-Odd Proton Emitters

The success of the ^{117}La run was followed by an experimental run to search for new, odd-odd proton emitters in September of the same year (2000). In all three cases, the isotopes desired were from elements which already had at least one other, odd-even, proton emitting isotope. The objective here was to look for the odd-odd proton emitting isotopes further from stability. Of particular interest was ^{130}Eu, since its neighbouring isotope, ^{131}Eu, was heavily deformed, as well as exhibiting fine-structure. It would provide the opportunity to contrast the well-studied ^{131}Eu with its odd-odd neighbouring isotope. ^{130}Eu would be one of the few odd-odd proton emitters discovered in the predicted region of large prolate deformation predicted by Möller *et al.*, see Fig. 2.4.

It should be noted that when the experiment began, ^{164}Ir was an unknown nucleus, with no information from conferences or publications to indicate otherwise. However, at the end of the run in 9/2000, after observing evidence for the nucleus in the online analysis, information came to light in private communications that a group at Jyväskylä had observed a few unknown events which could also have been from the proton decay of ^{164m}Ir. This has since been confirmed, and the results published [Ket01], but the results obtained from the ANL run do provide a completely independent observation of ^{164m}Ir.

4.2.1 Experimental Details

Detectors used in this experimental run included the standard PPAC, as well as a 48×48 DSSD. The smaller area of this detector, 256 mm^2 as opposed to the 1600 mm^2 of the 40×40 would not be a great disadvantage, particularly since we would be using a number of inverse reactions in this run, which focuses the recoils more tightly forward. The standard back silicon detector was used, as well as the BOX since it could prove useful to veto, in particular, escape α's since a number of regions of interest in this run would be contain large numbers of α-emitters.

A ^{78}Kr beam was used throughout the runs in this experiment. The calibration run used a 362.5 MeV ^{78}Kr beam on 1.14 mg/cm^2 ^{92}Mo to produce two proton lines from ^{167}Ir, as well as a number of α-emitters, see Fig. 3.10. During the run which yielded ^{164m}Ir, the known proton emitter, ^{165m}Ir, was also produced and was used as a third point in the proton calibration. There were many internal α-lines for use in the explicit α-calibration.

HIVAP calculations were used to choose the optimum beam energies for all the searches for the new isotopes desired in this experiment. Also, in all the searches undertaken, a 2.96 mg/cm^2 thick aluminum degrader was placed before the DSSD to insure that the desired recoils were implanted in the DSSD at a reasonable energy, as mentioned in the previous chapter.

4.2.2 Decay of ^{130}Eu

^{130}Eu was produced using a 432 MeV beam on a 425 μg/cm^2 thick ^{58}Ni target, with an excitation energy of 99 MeV at the center of the target, again as indicated by a HIVAP calculation. This is the same beam+target combination that was used to produce ^{131}Eu, but with a higher energy to more readily access the $p5n$ evaporation channel. The FMA was set to E=221.6, Q=33.5 and A=130, with slits in position to only transmit the A=130 recoils with charge states of 33^+ and 34^+ through to the detectors. This was done to allow the A=130 recoil rate on the PPAC to be set as high as possible since the cross-section for the $p5n$ nucleus, ^{130}Eu, would be very small. The PPAC rate was $\sim$ 4.5 kHz, near the limit sustainable by the detector.

The decay spectra seen in Fig. 4.5(a) is ungated, and mainly consists of β related background from delayed protons. However, when conditions are imposed requiring the decay to occur within 3.2 ms of an A=130 recoil being implanted in the same pixel, the background is removed, with a peak clearly visible at $\sim$ 1 MeV. Due to the events being too fast to be β-related, and being too low in energy to be from an α-decay, this peak is assigned to a new proton emitter with an energy $E_p = 1020(15)$ keV.

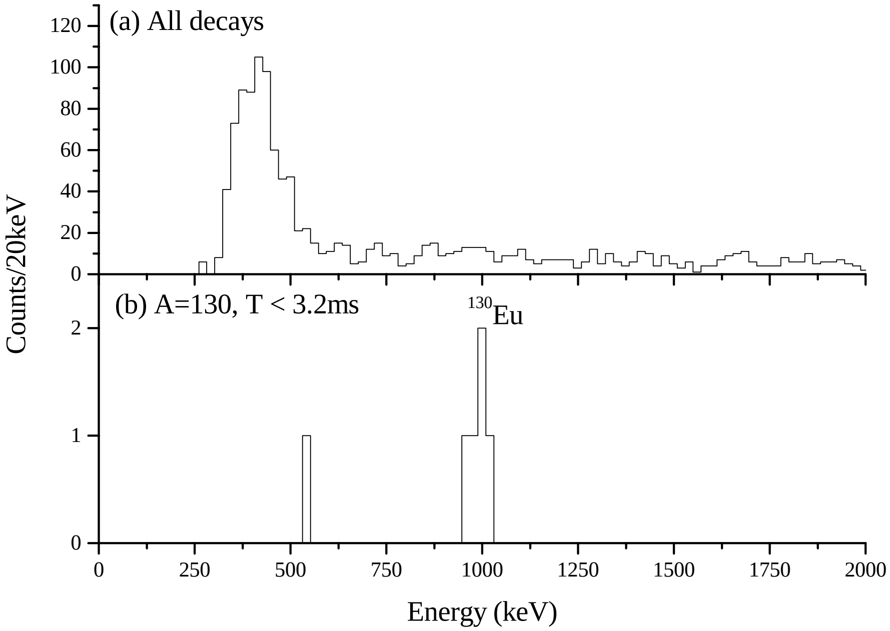

Figure 4.5: *Spectra showing (a) all the decay products from the reaction* $^{78}Kr+^{58}Ni$ *with slits in place to only transmit A=130 recoils and (b) the decay products which are present after a 3.2 ms time gate has been placed between an implanting recoil and a decay occurring within the same pixel of the DSSD.*

The production mechanism limits the number of possible candidates, as being lower in N and Z than the compound nucleus ^{136}Gd. Systematics and theoretical mass predictions indicate that isotopes with $A = 130$ of elements lower in Z than Eu are single proton bound [Mol97, Aud95]. With a higher and even Z, ^{130}Gd is predicted to be close to, if not beyond, the single proton dripline [Mol97, Lir76, Com88, Tac88], but HIVAP [Rei81] cross-section calculations indicate that, with this experimental setup, ^{130}Eu would be produced with a cross-section approximately a factor 400 larger than that of ^{130}Gd, ($\sigma \sim 15$ nb versus $\sigma \sim 40$ pb). We can therefore conclude that the proton peak observed in Fig. 4.5(b) is from the decay of the new isotope ^{130}Eu.

The single count at 0.5 MeV seen in Fig. 4.5(b) is attributed to an escape from the main peak. It is so fast that it is unlikely to be a β-related event. It is also too low in energy to be from any possible decay of ^{130}Eu to an excited state in ^{129}Sm, a ^{130}Eu proton with ~0.5 MeV would have a partial half-life of days. Since the ^{130}Eu recoil ions are implanted to a depth of around 12μm, and 1 MeV protons have a range of $\sim$ 17μm in silicon, approximately 25% of them are predicted to escape. Therefore, with 6 counts in the main peak, one escape is reasonable.

Due its large proton Q-value (Q_p = 1028(15) keV), ^{130}Eu ($t_{1/2} = 900^{+490}_{-290}\ \mu$s) decays via proton emission, with a possible small β-decay branch. Möller *et al.* predict a beta half-life of 49.1 ms [Mol97] and therefore, in this work, we assume a 100% proton decay branch.

After running for almost 2 days with a $\sim$ 3.5 pnA beam current, transmitting two charge states of A=130 recoils through the FMA, the production cross-section for ^{130}Eu was found to be $\sigma\sim$ 9 nb (with a factor of two uncertainty), similar to the 15 nb predicted by HIVAP. It is approximately an order of magnitude lower than the cross-section of its odd-even neighbour ^{131}Eu, one neutron closer to stability, which had a cross-section of $\sigma\sim$ 90 nb in an experiment using a similar setup and beam+target combination [Son99]. This is entirely consistent with results seen by K. Rykaczewski *et al.* with $^{141}Ho(\sigma\sim$ 130 nb) and $^{140}Ho(\sigma\sim$ 13 nb) [Ryk99], which reinforces the assignment of the new proton line to ^{130}Eu.

Spherical WKB [Woo97] calculations did not agree with the experimental results. For a $d_{5/2}$ proton, a half-life of $\sim 30\mu$s was calculated, and for a $g_{7/2}$ proton, the calculated half-life was $\sim$ 6ms, neither of which were reasonable when compared to the 900^{+610}_{-260} μs experimental half-life of ^{130}Eu. This is supported by the fact that the neighbouring isotope, the proton emitter ^{131}Eu, is deformed and so one would expect that ^{130}Eu could be deformed as well. In fact Möller *et al.* predict ^{130}Eu and its proton-daughter, ^{129}Sm, to have a quadrupole deformation β_2= 0.331 [Mol95, Abo95].

Therefore, detailed calculations on this nucleus, taking into account the angular momentum of the odd neutron, as well as the deformation of the potential barrier were undertaken using the formalism of Ferreira and Maglione *et al.* [Fer01].

The calculation was made assuming the proton is in the $3/2^+[422]$ orbital, consistent with that of it's odd-even neighbour ^{131}Eu [Dav98], where detailed analysis of the fine-structure exhibited by this nucleus supported this assignment [Son99, Mag00]. A similar case can be made for assuming that ^{130}Eu has the same deformation as ^{131}Eu, $\beta_2 = 0.33$, this also being consistent with the Möller *et.al.* prediction [Mol95]. Calculations for the half-life of ^{130}Eu were made for two values of the neutron spin which are predicted to lie near the Fermi surface [Mol97], $K_n = 1/2^+$ and $K_n = 7/2^-$, along with the associated total spin in the parent nucleus, $J = K_T$. It should be noted that the spin of daughter nucleus spin, ^{129}Sm, is assumed to be that of the odd neutron, $J_D = K_n$, the odd-proton having been emitted and the core having no spin.

The results are shown in Fig. 4.6, where it can be seen that the case for $K_n = 7/2$ is very weak, and that $K_T = 1^+$ is not a promising candidate unless ^{130}Eu is much more strongly deformed than expected ($\beta_2 > 0.35$). The calculations indicate that the most likely ground state spin for ^{130}Eu is 2^+, with the unpaired spectator neutron having $K_n = 1/2^+$. This yields an experimental Spectroscopic factor of $S_{exp} = 0.41^{+0.25}_{-0.31}$ which is reasonably close to the $S_p^{th} \sim 0.5$ expected from BCS theory, though note again that detailed BCS calculations are hampered by the abundance of Nilsson single-particle orbitals.

There was no strong evidence to indicate that ^{130}Eu would necessarily exhibit fine-structure, and none was observed in this experiment, unlike the neighbouring ^{131}Eu. An upper limit of $\lesssim 30\%$ being set for the branching ratio for the decay to any possible low-lying excited state in the daughter nucleus ^{129}Sm, assuming two new counts were observed in a fine-structure peak.

4.2.3 Decay of ^{164m}Ir

^{164}Ir was pursued using a 437 MeV beam on a $0.773\mu g/cm^2$ thick ^{92}Mo target, yielding an excitation energy at the center of the target of 86 MeV. The FMA was set to E=166, Q=34 and A=164, transmitting three charge

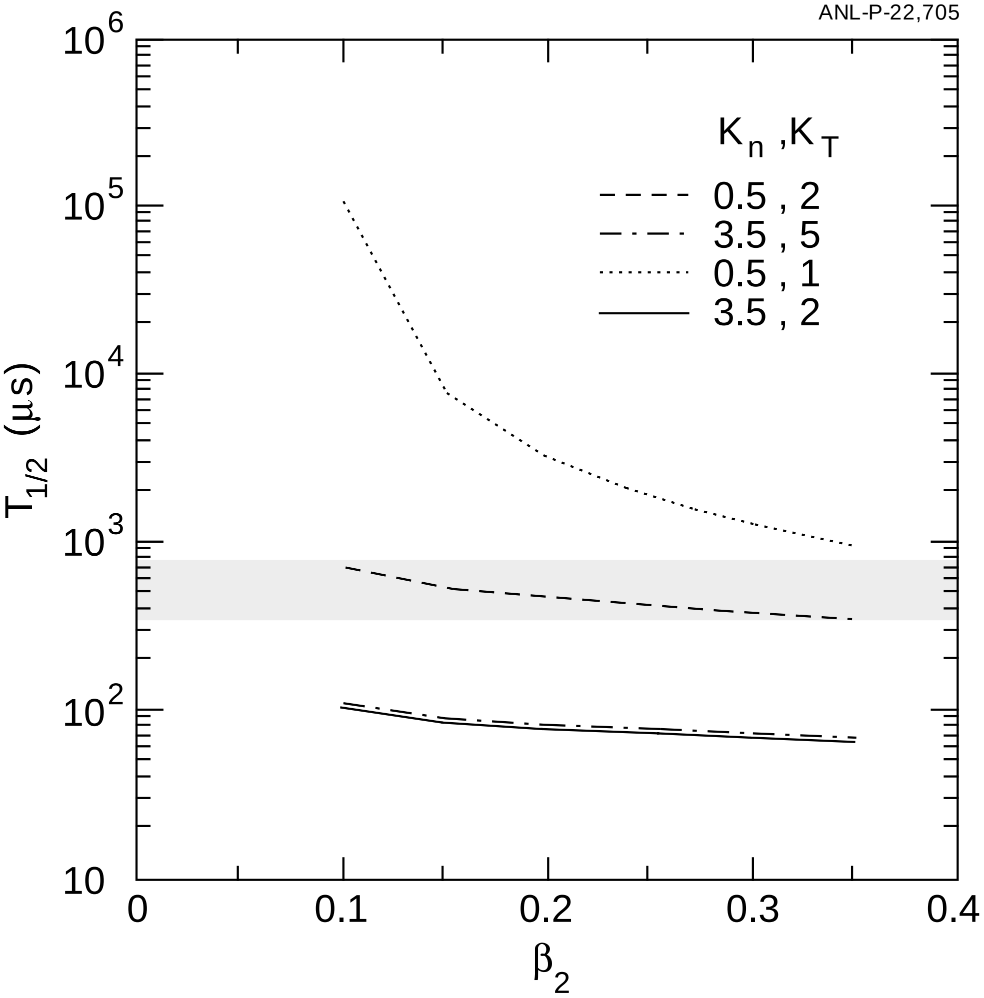

Figure 4.6: *Graph showing proton half-life versus quadrupole deformation, β_2 for ^{130}Eu. The shaded area encloses the experimental half-life, including uncertainty, folded with the theoretical prediction of a Spectroscopic factor of 0.5. The odd proton is assumed to have the same spin projection as ^{131}Eu, $K_p = 3/2$. Calculations for the half-life of ^{130}Eu for two values of the neutron spin, $K_n = 1/2$ and $K_n = 7/2$, are shown, along with the associated total spin in the parent nucleus, $J = K_T$. It should be noted that the spin of the daughter nucleus spin, ^{129}Sm, is assumed to be that of the odd neutron, $J_D = K_n$, the odd-proton having been emitted and the core having no spin.*

states of ^{164}Ir, $33^+, 34^+$ and 35^+. There was no need, in this case, to use slits in front of the PPAC due to excessive scattered beam.

Proton emission has already been observed from three Ir isotopes, ^{165}Ir, ^{166}Ir and ^{167}Ir [Dav97]. These results are consistent with proton decay from a spherical nucleus. Isomeric proton decays were assigned to $\mathrm{h}_{11/2}$ proton emission in $^{166,167}Ir$ in addition to ground state proton decays from lower spin states. In the case of ^{165}Ir only $h_{11/2}$ proton emission was observed, indicating the low spin ground state proton state was too short-lived for experimental observation [Dav97].

In this experiment, the known proton decay ^{165m}Ir can clearly be seen in Fig. 4.7(b), which was used as part of the proton calibration. When a further condition, requiring the daughter ^{163}Os α-decay to be observed is set, we see a peak at E_p = 1807(14) keV, equivalent to a proton Q-value Q_p = 1818(14) keV, see Fig. 4.7(c). This peak is assigned to the nucleus, ^{164}Ir, on the basis of the mass selection as well as daughter α correlations. The half-life of this peak is $t_{1/2} = 58^{+32}_{-19}$ μs. This is in good agreement with results reported from the independent experiment at Jyväskylä [Ket01], where the proton energy was reported as being 1817(9) keV and $t_{1/2} = 113^{+62}_{-30}$ μs, which provides mutual corroboration of the identification of this decay as coming from a state in ^{164}Ir. When we compare our results to those for the neighbouring proton-emitter, ^{165m}Ir (E_p = 1707(7), $t_{1/2}$ = 300(60) μs, BR=0.87(4) [Dav97]) we can see that the 100 keV proton energy increase between these two isotopes decreases the half-life of ^{164m}Ir by approximately a factor of 5, clearly illustrating the strong dependence of the half-life to the energy, among other factors. The half-life of ^{165m}Ir was measured in this work as being $t_{1/2} = 220^{+55}_{-40}$ μs, in reasonable agreement with the previous

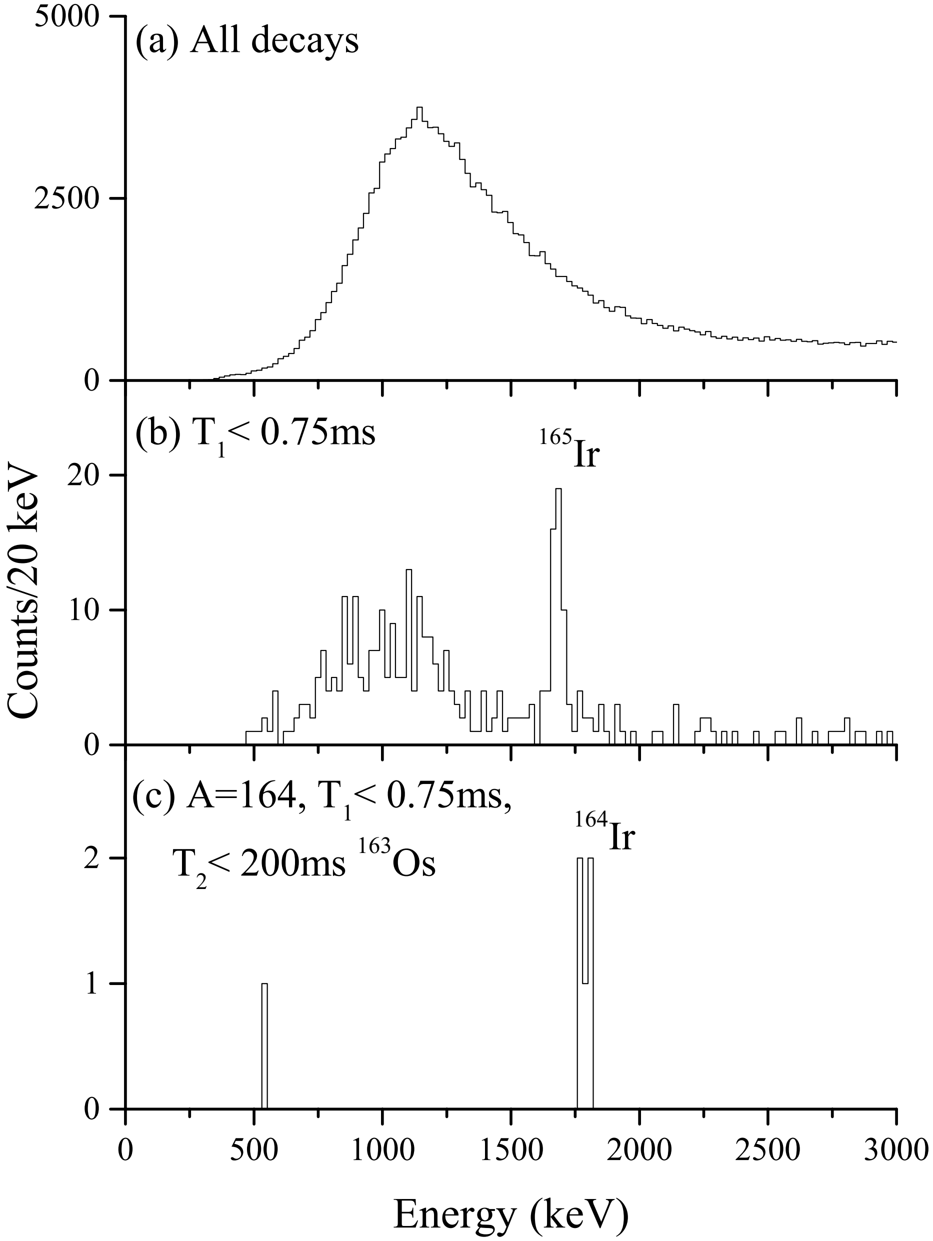

Figure 4.7: *Spectra showing the decays, below 3 MeV, from recoils produced in the reaction* ^{78}Kr + ^{92}Mo *with (a) no conditions and (b) the condition that the decay occurs within 0.75 ms after a recoil has been implanted within the same pixel of the DSSD. The conditions are tightened in (c) to further require the daughter* α*-decay of* ^{163}Os *within 200 ms of the initial decay within the same pixel, and only decays associated with A=164 recoils are shown.*

value.

It should be noted that while ^{165m}Ir was observed to have a small α-decay branch, no appreciable branch was observed in this experiment, with a branching ratio limit of $BR_\alpha < 20\%$ for one α event correlated to a subsequent daughter decay. This limit is relatively high due to the low number of ^{164m}Ir events, and the BR_α is expected to be much lower due to the fast proton decay of ^{164}Ir when compared to predicted α partial half-life of 1.38 ms [Mol97].

Spherical WKB calculations, shown in Table. 4.2, indicate that the proton emitting orbital is probably $\pi h_{11/2}$, similar to the odd-even neighbour ^{165m}Ir. This assignment would yield a $S_{exp} = 0.35^{+0.29}_{-0.13}$, in good agreement with a low-seniority shell model prediction of 0.33 [Dav97], as well as the $\sim$ 0.23 from spherical BCS calculations [Åbe97]. Therefore it is consistent with ^{164m}Ir being a near spherical nucleus. This is similar to the spectroscopic factor calculated by Kettunen *et al.* of 0.19(7) [Ket01] using the formalism of Cary *et al.* [Dav97]. As with ^{165m}Ir, it is most likely that the proton decay observed in this experiment is from an isomeric state with the low spin ground state decay being too short-lived for observation. This would be consistent with the level ordering found for proton emitting states in the odd-odd neighbour ^{166}Ir. By looking at the energy difference between the ground and isomeric states in ^{166}Ir, an estimate of the excitation energy of ^{164m}Ir can be made as being $\sim$250 keV, which is similar to ^{165m}Ir [Dav97]. This can be used to estimate the energy of a possible ^{164}Ir $s_{1/2}$ state as being $\sim$1560 keV, and hence the proton half-life of this state as $\sim$ 0.1 μs, which would make the ground state of ^{164}Ir experimentally unobservable.

After running for 23 hours with a 4 pnA beam, transmitting three

Table 4.2: *Comparison of experimental and calculated proton partial half-lives for the spherical nuclei, ^{164m}Ir and ^{170m}Au, using a WKB approximation and a Becchetti and Greenlees optical potential.*

Nucleus	$Q_{p,nuc}{}^{a}$	$t_{1/2,p}^{exp}$ (μs)	Proton orbital	$t_{1/2,p}^{WKB}$ (μs)
^{164m}Ir	1834(14)	58^{+32}_{-19}	$s_{1/2}$	0.0003
			$d_{3/2}$	0.013
			$h_{11/2}$	20
^{170m}Au	1762(9)	760^{+260}_{-160}	$s_{1/2}$	0.016
			$d_{3/2}$	0.11
			$h_{11/2}$	160

---

[a] Proton Q-value plus screening correction from Huang and Mark [Hua76].

charge states through the FMA, ^{164m}Ir was found to have been produced with a cross-section $\sigma \sim 11$ nb which is over an order of magnitude lower than the 200 nb quoted for ^{165m}Ir [Dav97]. It should be noted that ^{130}Eu and ^{164m}Ir are currently some of the few known proton emitters to have been produced via the $p5n$ fusion evaporation channel. This explains their low production cross-sections' which are similar to the 13 nb production cross-section of ^{140}Ho [Ryk99]. The cross-section limit for any, experimentally observable, proton emitting ground state is set at $\sigma < 4$ nb, for two events correlated with daughter decays.

The element Iridium is presently unique in exhibiting proton decay from four different isotopes.

4.2.4 Decay of ^{170m}Au

^{170}Au was the next isotope studied, using a 400 MeV beam on a 513 $\mu g/cm^2$ thick ^{96}Ru target, with 401 $\mu g/cm^2$ of ^{197}Au in front of the target to support the fragile ^{96}Ru target. This resulted in an excitation energy at the center of the target of 58 MeV. Three charge states of A=170 recoils were initially transmitted. However, in the middle of the ^{170}Au run, the PPAC rates, which were usually $\sim$ 4 kHz, started falling. The run was stopped, the target checked and a hole was found in the fragile ^{96}Ru target. The target position was changed slightly, so the beam hit a fresh part of the target. The beam was retuned during this period, which required that the FMA settings had to be rechecked (since changing the beam parameters can change the behaviour of the scattered beam reaching the FMA focal plane). The new FMA setting which were then used were E=158, Q=32.67 and A=170, with a central obstruction in place to occlude the scattered beam which was observed, effectively creating the slits through which two charge states of A=170 recoils were transmitted.

^{171}Au is the only previously observed proton emitting Au isotope [Dav97, Pol99]. Proton emission has been observed from the short-lived $s_{1/2}$ ground state [Pol99] and a longer lived $h_{11/2}$ isomeric state at an excitation energy of 250 keV [Dav97].

The proton decay of ^{170}Au is clearly present at an energy E_p = 1735(9) keV in Fig. 4.8(b) (and even more visible in Fig. 4.8(c)). The half-life of this state is $t_{1/2} = 570^{+260}_{-160}$ μs. An alpha branch was also identified from this state in ^{170m}Au (with an alpha energy E_α = 7.056(15) MeV). Only two events are observed, in Fig. 4.9(c), one of which is an escape which is not unusual when we expect almost 40% of the α-particles to escape out of the front of the DSSD. Note that BOX veto for escape particles was not used in Fig. 4.9(c). The low statistics meant that extra correlations were used to verify the assignment of these decays to ^{170m}Au, with the high energy α followed by the decay of ^{166m}Ir and ^{162m}Re. The discovery of these α decays yields a proton decay branch $B_p = 0.75(15)$ ($B_\alpha = 0.25(15)$). Note that we

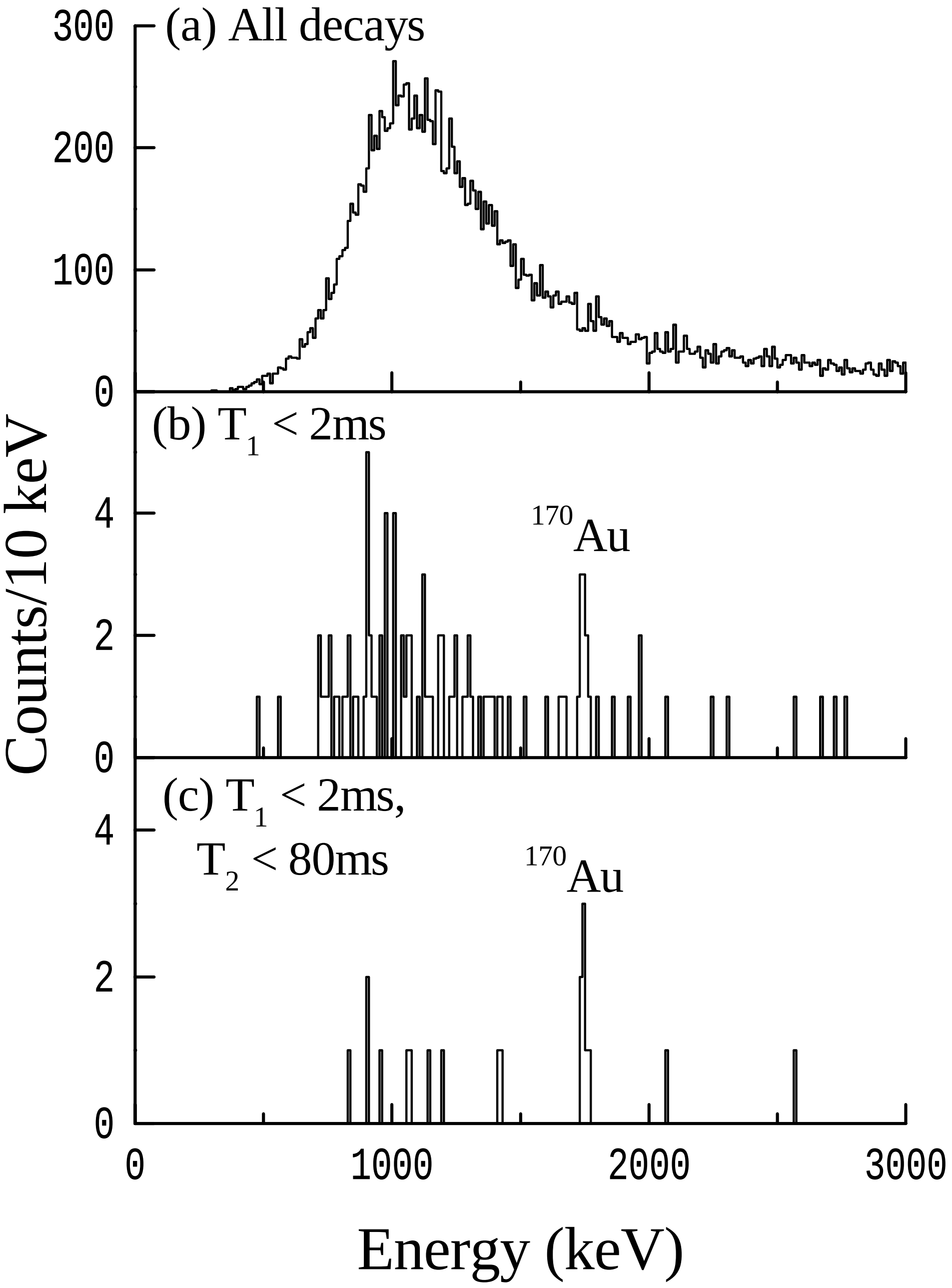

Figure 4.8: *Spectra showing the decays, below 3 MeV, from recoils produced in the reaction* ^{78}Kr + ^{96}Ru *with (a) no conditions and (b) the condition that the decay occurs within 2 ms after a recoil has been implanted within the same pixel of the DSSD. A further condition that a second decay occurs within 80 ms of the first is added in (c).*

assume a negligible β-decay branch, which is supported by the predicted β partial half-life, $t_{1/2,\beta} = 272$ ms, of Möller *et al.* [Mol97].

WKB calculations, see Table. 4.2, indicate that the proton was emitted from a $\pi h_{11/2}$ orbital, probably with a $[\pi h_{11/2}, \nu h_{9/2}]10^+$ or possibly 1^+ configuration. The neutron assignment is made by adding two neutrons on the base of the ^{166}Ir, $\nu f_{7/2}$ neutron configuration [Dav97], resulting in the valence neutron being in the next orbital. This assignment is supported by shell level calculations by Möller *et al.* [Mol97]. The spectroscopic factor for this decay is $S_{exp} = 0.21^{+0.08}_{-0.12}$, and is in good agreement with a low-seniority shell model prediction of 0.22 [Dav97], as well as the ~ 0.15 from BCS calculations [Åbe97], indicating that ^{170m}Au is spherical.

The reduced width of the α-decay branch was calculated as being 38^{+31}_{-36} keV using the formalism developed by Rasmussen [Ras59] and assuming a $\Delta l = 0$ transition to the $h_{11/2}$ state in ^{166m}Ir. This is similar to the reduced width calculated for the decay of ^{166m}Ir to ^{162m}Re which was 43(3) keV [Dav97]. The large error in the reduced width of ^{170m}Au was due to the low α-decay statistics in this experiment.

^{170}Au could also have a low lying ground state, for example $s_{1/2}$, which was not observed, perhaps due to its cross-section being too low. An upper limit of 2 nb being placed on the production cross-section of a low-lying state. This could be due to the fact that generally the fusion evaporation production mechanism preferentially populates high spin states, at the expense of lower spin states. An alternative reason for the low-spin state not being observed could be that it may be too fast to be detected with the experimental setup used. This fast speed of the decay of a possible ground state would be due to the proton orginating from a lower angular momentum

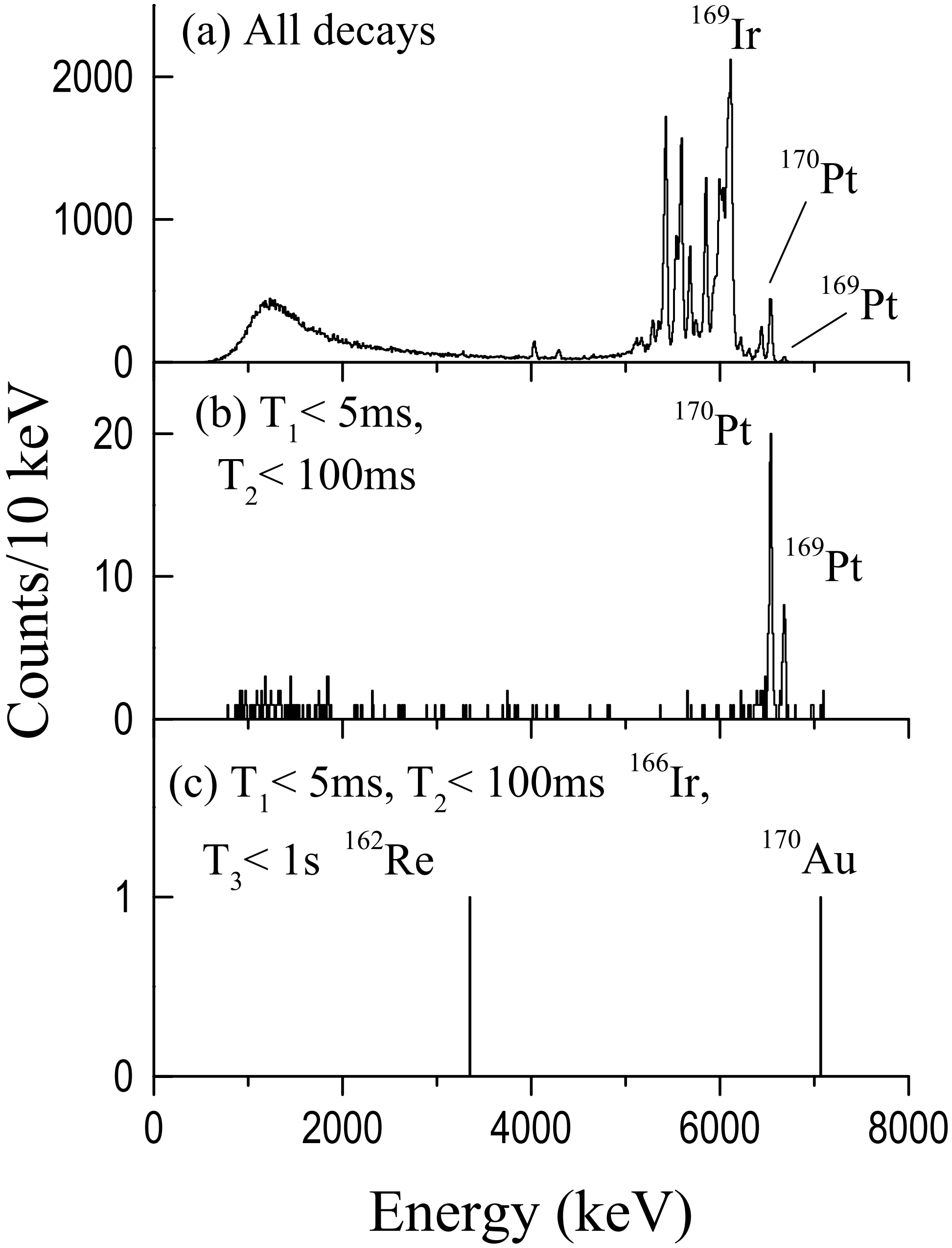

Figure 4.9: *Spectra showing the decay products from the reaction ^{78}Kr + ^{96}Ru with (a) no conditions and (b) the condition that the decay occurs within 5 ms after a recoil has been implanted within the same pixel of the DSSD, and are followed by a daughter decay in the same pixel within a further 100 ms. Finally, the conditions are tightened; requiring the first daughter decay occur not only within 100 ms, but that it have the correct energy for that of an ^{166m}Ir α, and be followed within a further second by an ^{162m}Re α.*

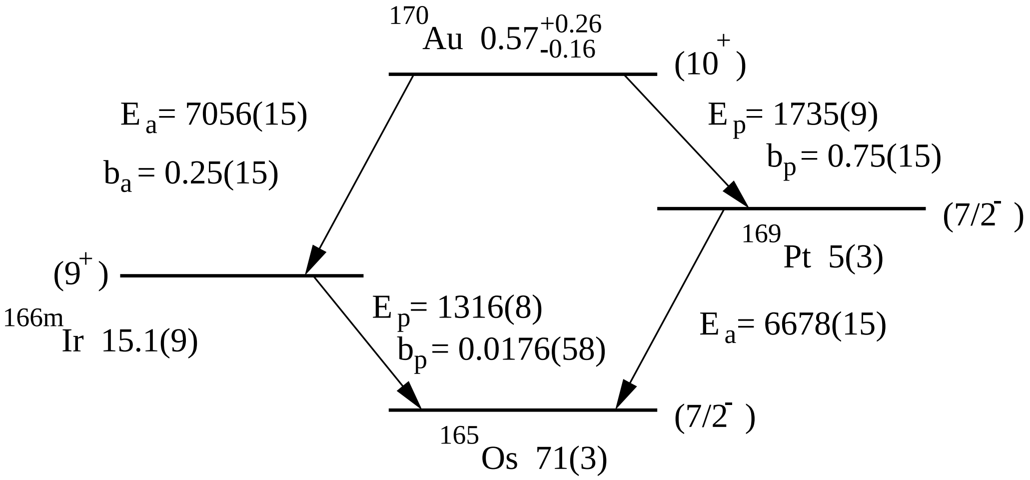

Figure 4.10: *Decay scheme for ^{170m}Au. Half-lives are stated in ms, and all energies are in keV.*

state. This would result in a lower centrifugal barrier and would therefore provide less hinderance than for a proton with more angular momentum. For example, we can assume an excitation energy for ^{170m}Au of up to 250 keV, similar to that of its α-daughter ^{166}Ir, as well as the 200 keV of the neighbouring ^{171m}Au. This would yield a ground state proton $>$ 1.5 MeV. This would have a partial half-life of < 2 μs ($s_{1/2}$) or < 14 μs ($d_{3/2}$). These two states lie close together, but the $d_{3/2}$ would be the most likely candidate for a possible low-lying ground state of the odd-odd nucleus ^{170}Au following the trend of $^{166,167}Ir$, $^{160,161}Re$ and $^{156,157}Ta$ [Dav97, Pag92, Irv97, Uus99]. In all these cases, the proton in the ground state of the odd-odd nucleus is $d_{3/2}$, while for the even-N ground state, including ^{171}Au, the proton occupies the $s_{1/2}$ orbital.

The decay chain linking ^{170m}Au with the known proton emitting state, ^{166m}Ir is shown in Fig. 4.10.

The effective cross-section for the production of ^{170m}Au was found to be of the order of $\sigma \sim 20$ nb, over an order of magnitude lower than that of other $p3n$ proton emitters such as ^{160}Re (~ 1 μb [Pag92]). In fact, this cross-section is as low as the $p5n$ proton emitters mentioned in this paper, even though ^{170m}Au is a $p3n$ nucleus. The reason is due to the large fission probability of ^{170m}Au, predicted by HIVAP to be 94%, meaning most of the compound nuclei ^{174}Hg, de-excited via fission as opposed to via particle evaporation. This would result in a lower than expected yield of evaporation recoils such as ^{170m}Au.

4.2.5 Search for ^{126}Pm

A search was also undertaken for the new isotope, ^{126}Pm, using the same 432 MeV ^{78}Kr beam used in the ^{130}Eu run, and a 751 $\mu g/cm^2$ ^{54}Fe which was available in the target wheel. ^{126}Pm was the only Promethium isotope realistically accessible with the beam and time available. Two charge states of ^{126}Pm were transmitted through the FMA, 32^+ and 33^+.

No fast (< 300 μs) decays were seen below 2 MeV, which would indicate proton emission, and the promethiums are not expected to be α-emitters, so there was no clear indication of decay from an unknown nucleus. The spectra for longer correlation times are shown in Fig. 4.11, where no prominent peaks can be seen.

A half-life dependent cross-section limit is set on ^{126}Pm. The longer the half-life, the greater the implant-decay correlation time leading to a larger background and hence the more decay events necessary to register as significant with respect to the background. For half-lives 50 ms $\leq t_{1/2} \leq$

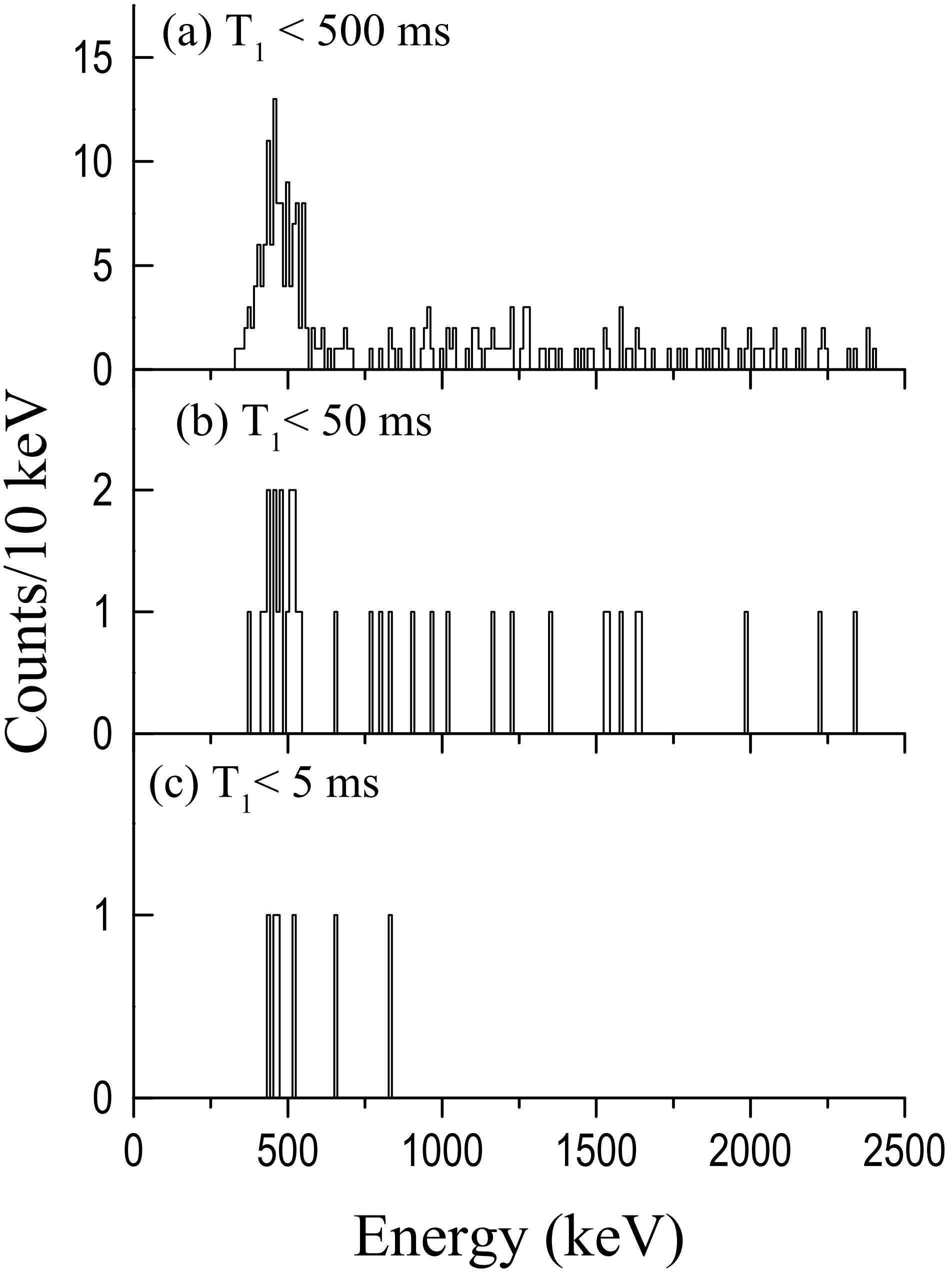

Figure 4.11: *Decay energy spectrum of all decays occurring within the DSSD and below 2 MeV, for a 432 MeV ^{58}Ni beam bombarding a 751 $\mu g/cm^2$ ^{54}Fe target for a total of 1.5 days, within: (a) 500 ms of an implantation, (b) 50 ms of an implantation and (c) 5 ms of an implantation within the same pixel.*

500 ms; $\sigma \sim 10$ nb. For a half-life 5 ms $\leq t_{1/2} \leq$ 50 ms, $\sigma \sim 4$ nb and for 5 μs $\leq t_{1/2} \leq$ 5 ms, a limit of $\sim$ 2 nb, which are reasonable for a $p5n$ nucleus, see Sec. 4.1.4, and close to the HIVAP prediction for this energy of $\sim$ 18 nb. One possibility is that the beam energy, and hence excitation energy of the compound nucleus $^{132*}Sm$, was not near the optimum for the $p5n$ channel in this instance, with HIVAP predicting the optimum cross-section at a lower beam energy of $\sim$ 420 MeV.

4.3 Mass Model Predictions

With the progress in proton radioactivity studies, we can confront the three mass models described in Sec. 2.4 with available experimental data on neutron-deficient nuclei between $50 < Z < 82$, in the form of proton separation energies. While most of this is obtained directly from the proton decay energies, some data was obtained indirectly by following α-decay chains to a nucleus for which an experimental mass excess was obtained. This has been done for decay chains from ^{166}Ir and ^{177}Tl [Dav97, Dav00c]. Figures 4.12, 4.13 and 4.14 show predictions from Liran-Zeldes, Möller *et al.* and Aboussir *et al.* respectively.

The Liran-Zeldes model seems to produce best overall predictions for this neutron-deficient region, with the smallest mean and RMS deviation between predicted and experimental proton decay values as shown in Table. 4.3. This is interesting considering it is the oldest model of the three presented, and hence would contain a smaller database of known masses for parametrisation of coefficients. The S_p predictions vary smoothly along each element, with an odd-even staggering which is less pronounced than

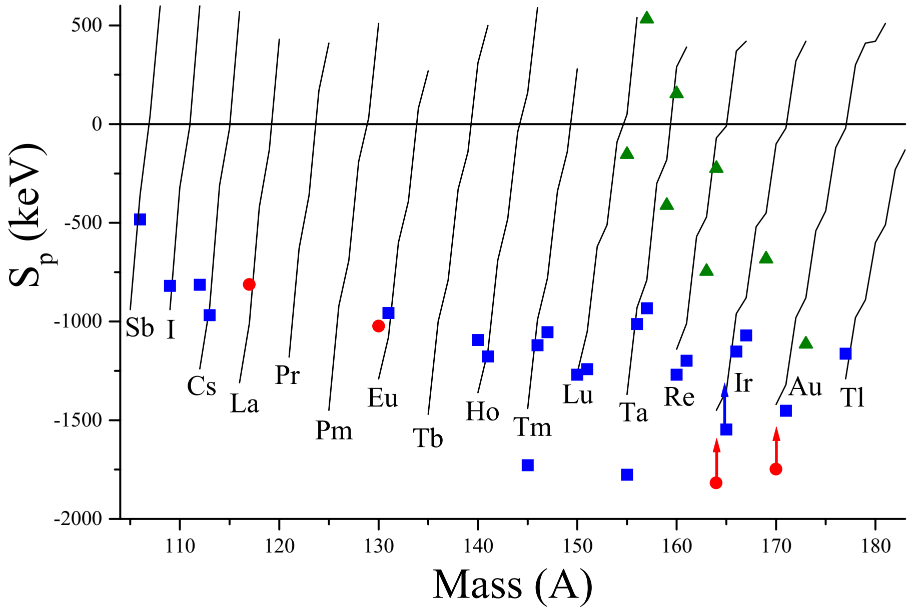

Figure 4.12: *Graph showing proton separation (S_p) energies along the dripline for odd Z nuclei from Sb to Tl. The red circles represent S_p values for the proton emitters presented in this thesis. The blue squares are S_p values obtained experimentally from other proton emitters and the green triangles are S_p values obtained from mass excess values which were found by following α-decay chains from the known proton emitter ^{167}Ir down to an isotope with a known mass. The arrows indicate proton emitting isotopes for which only a high-spin isomer has been observed, the S_p value being lower than this by the unknown excitation energy. The lines represent predictions by Liran-Zeldes [Lir76].*

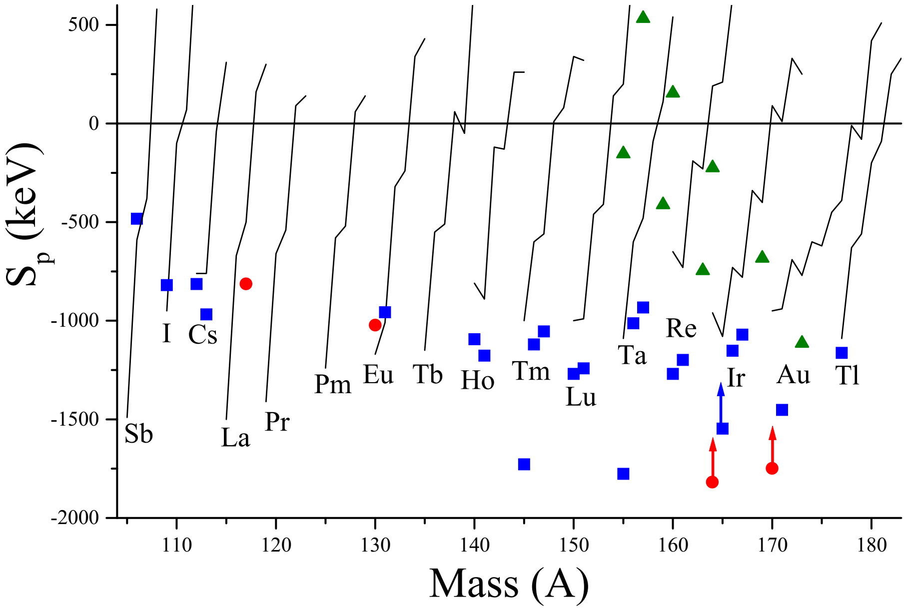

Figure 4.13: *As with Fig. 4.12, but now with predictions by Möller* et al. *[Mol97].*

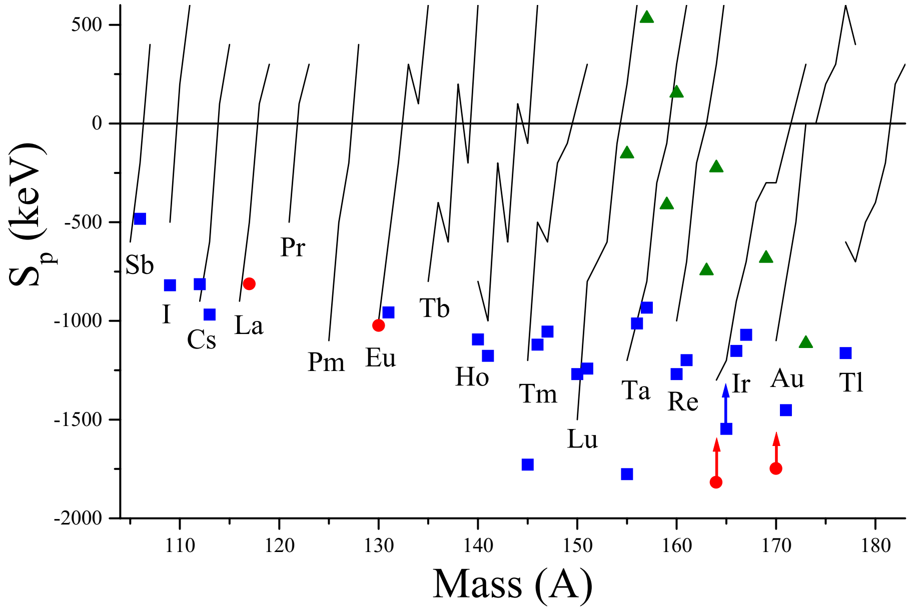

Figure 4.14: *As with Fig. 4.12, but now with predictions by Aboussir* et al. *[Abo95].*

Table 4.3: *Mean and RMS deviations for the experimental proton decay energies versus model predictions.*

Model	Mean Deviation (keV)	RMS Deviation (keV)
[Lir76]	-7	232
[Mol97]	173	442
[Abo95]	257	360

that exhibited by the other two models presented here. This could account for the small mean deviation, smearing out the predicted values relative to the experimental ones.

One can observe that the discrepancy between the predictions and experiment is larger for higher Z, overbinding the heavier elements in this region. This may be related to the fact that deformation effects are generally seen to be important for the lighter elements in this region, perhaps since so much recent interest has been involved in studying more exotic and deformed nuclei, and hence a greater bias towards reproducing their mass excesses may have been inadvertently introduced to some degree. In particular, the model by Möller *et al.* has the largest RMS deviation, not only overbinding the heavier elements, but underbinding the lighter nuclei, indicating the unreliability of this macroscopic-microscopic model far from the region of known masses, relative to the other two models.

Aboussir *et al.* is the newest model of the three, and the only one calculated on a purely microscopic basis - hence it uses the least mature method for calculating masses. It also has the fewest number of parameters that are adjusted to fit known masses, only 8 compared to Möller *et al.* with 16. Taking this into account, it does reasonably well, with deviations similar to that from the more developed Möller *et al.* model. The self-consistency of the microscopic model compared to the micro-macroscopic models seems to already be apparent, and one can deduce that further development and refinement of purely microscopic models may yield predictions with much greater reliability in the future.

4.3.1 Mass Measurements

As an aside, we can note that decay chains from ^{164m}Ir and ^{170m}Au end on nuclei closer to stability, and that measuring the mass excess of one member of the chain results in information on all the members of the chain, analogous to ^{167m}Ir [Dav97]. The decay chain for ^{164m}Ir terminates with ^{152}Lu. For ^{170}Au, the decay chain from its proton emitting branch terminates with ^{153}Yb, and from its α branch with ^{154}Lu. These decay chains all terminate near the $N = 82$ shell closure and measuring the mass of any of the terminating isotopes would yield masses for all the isotopes constituting the decay chain. It should be noted that the daughters of ^{170}Au lie closer to stability, particularly ^{153}Yb which is only 15 neutrons deficient from its nearest stable isotope, providing easier experimental access. The proton emitter ^{166}Ir is also connected to this decay chain which would mean that any measurement of the mass of ^{170}Au yields a mass measurement of ^{166}Ir and vice versa.

4.4 α-emitters, ^{162}Os and ^{158}W

As mentioned previously, the experimental method developed for proton radioactivity studies is well suited for α-spectroscopy as well, and α-emission is prevalent in nuclei lying close to most heavier proton emitters. An explicit example of an α-spectroscopy experiment would be the search for fine structure in ^{107}Te [Sew02]. In a number of cases, however, we can obtain new information on α-decay during proton decay experiments, such being the case with ^{170m}Au.

4.4.1 ^{162}Os and ^{158}W

The previously observed α-emitters, ^{162}Os and its daughter ^{158}W [Hof81b], were produced during the search for the proton emitter ^{157}Ta [Irv97]. A 270 MeV, 3 particle nA ^{58}Ni beam which bombarded a 1.1 mg/cm^2 thick ^{106}Cd target for 38 hours to produce the compound nucleus ^{164}Os, with an excitation energy of 42 MeV at the center of the target. Among other nuclei, $2n$ nucleus ^{162}Os was produced and implanted in a 48×48 DSSD. The daughter nucleus, ^{158}W was also produced.

Fig. 4.15 shows the nuclei present with reasonable statistics, and measurements were taken of the α-decay of these two nuclei with an accuracy greater than those of previous experiments (see Table. 4.4). For ^{162}Os, an energy of E_α=6600(3) keV was obtained, with a half-life $t_{1/2}$=1.9(2) ms. It was produced with a cross-section $\sigma \sim 280$ nb in this run, under conditions which were not optimised for the $2n$ channel.

^{158}W was measured as having a half-life of $t_{1/2}$=1.5(2) ms and an α energy E_α=6445(3) keV. Since the initial population of ^{158}W was known, being due to the α-decay of ^{162}Os, its branching ratio could be measured as being b_α=96(6)%.

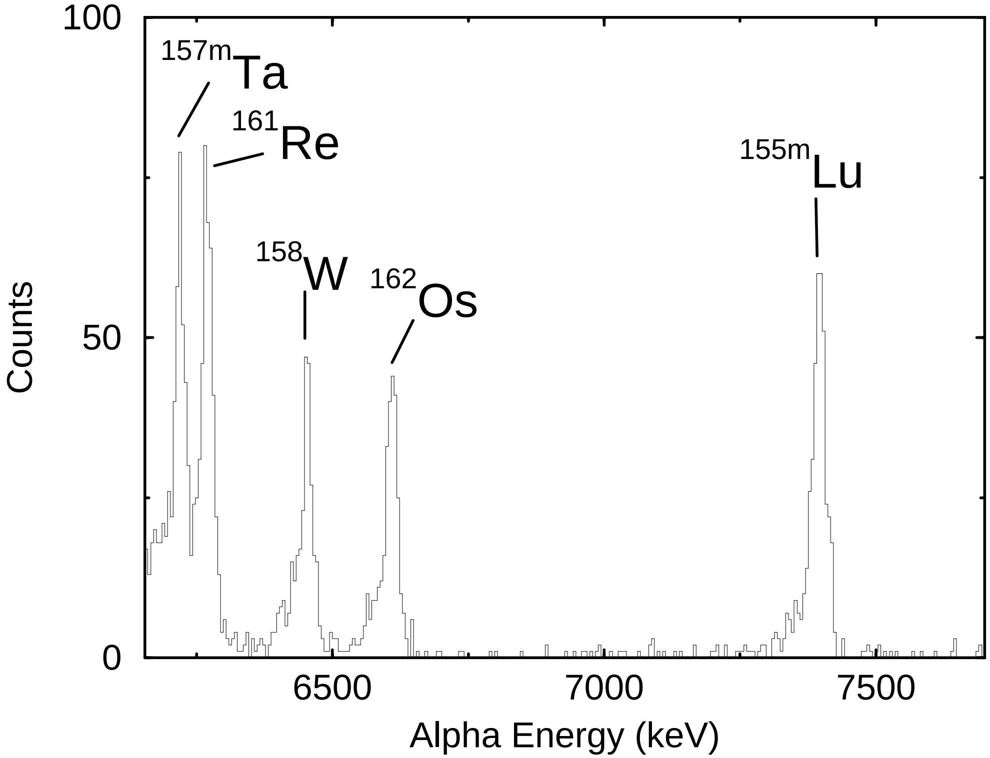

Figure 4.15: *α-decay energy spectrum, in the region 6.15 MeV to 7.7 MeV, of decays occurring within 20 ms of an implantation event in the same pixel in the DSSD, for the 270 MeV* ^{58}Ni *beam bombarding a* ^{106}Cd *target.*

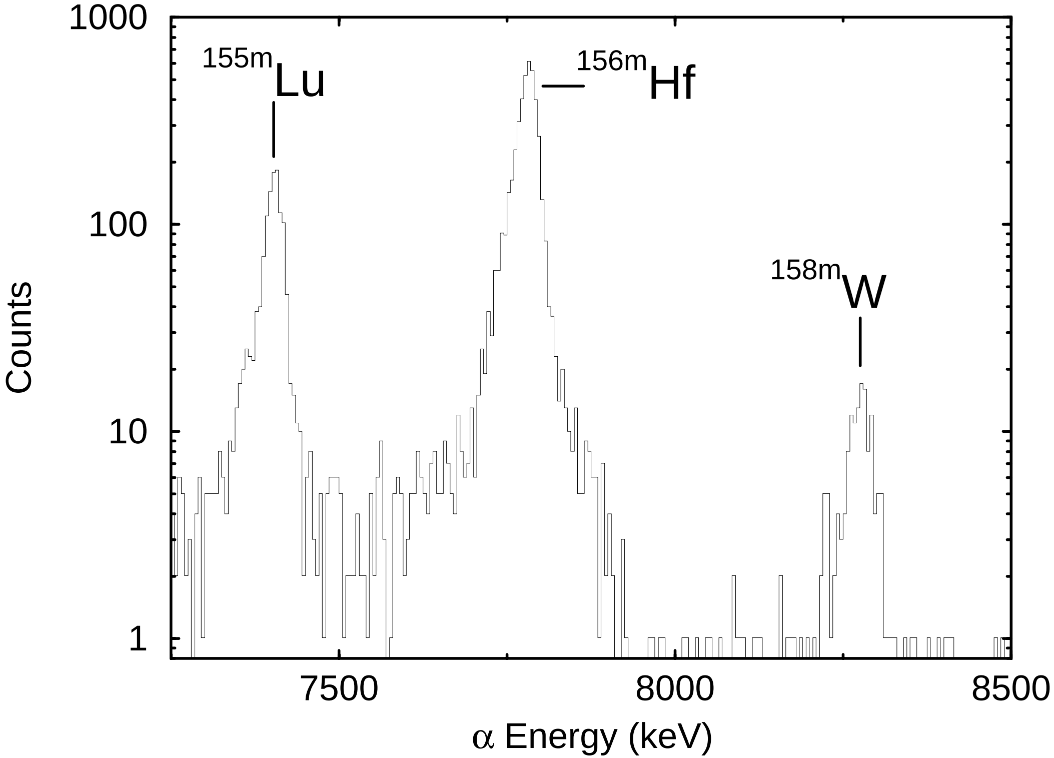

Figure 4.16: *α-decay energy spectrum, in the region 7.25 MeV to 8.5 MeV, of decays occurring within 1.5 ms of an implantation event in the same pixel in the DSSD, for the 270 MeV ^{58}Ni beam bombarding a ^{102}Pd target.*

4.4.2 ^{158m}W

The isomeric state ^{158m}W, first observed by S. Hoffman *et al.* [Hof89b], was observed during the search for ^{161}Re [Irv97]. The state was directly populated by bombarding a 1 mg/cm^2 ^{102}Pd target with a 270 MeV ^{58}Ni beam for 33 hours to produce the compound nucleus ^{160}W at a center of target excitation energy of 48 MeV using the standard DSSD detector setup.

Fig. 4.16 clearly shows the high energy ^{158m}W [E_α= 8286(7) keV, $t_{1/2}$=

Table 4.4: *Alpha decay energies, half-lives and reduced widths for* ^{162}*Os,* ^{158}*W and* ^{158m}*W. Reduced widths are calculated using the method described by Rasmussen in [Ras59], with* $\Delta l = 0$*. Where available, reduced widths are quoted from the cited references. Q-values used in the calculation include a screening correction [Per57]*

Nuclide	Energy (keV)	Half-life (ms)	Ref.	Width (keV)
^{162}Os	6600(3)	1.9(2)	[Mah00]	112(12)
	6619(10)	$1.5^{+0.7}_{-0.5}$	[Bin96]	120^{+80}_{-50}
	6611(30)	1.9(7)	[Hof89b]	100^{+100}_{-40}
^{158}W	6445(3)	1.5(2)	[Mah00]	73(11)
	6432(30)	$0.9^{+0.4}_{-0.3}$	[Pag96]	140^{+70}_{-60}
	6433(30)	0.9(3)	[Hof89b]	140^{+50}_{-60}
^{158m}W	8286(7)	0.14(2)	[Mah00]	3.69(55)[a]
	8291(24)	0.16(5)	[Pag96]	3(1)[a]
	8280(30)	0.01-0.1	[Hof89b]	

---

[a] The reduced widths for ^{158m}W were calculated assuming $\Delta l = 8$.

0.14(2) ms] α-line, which was measured with improved precision relative to previous experiments due to the improved statistics. S. Hoffman *et al.* assigned this state to a $[\nu f_{7/2} h_{9/2}]^{8+}$ shell model configuration, and no evidence was observed to contradict this assignment, see Sec. 4.4.3.

4.4.3 Discussion of the α-decay of ^{162}Os and ^{158}W

The measurements obtained at ANL for the α-decay of ^{162}Os, ^{158}W and ^{158m}W are shown in Table. 4.4. They are compared with previous experimental measurements and are seen to possess greater accuracy, particularly with regards to the energy where the present uncertainty is at least a factor 3 better than previously measured, due to the higher statistics. The results are in good agreement with the previous values, with the exception of the half-life of ^{158}W. Here, we can see the measured half-life presented is longer than the previous value.

Table. 4.4 also includes reduced α-widths which can be obtained using the expression:

$$Width = \frac{hb_{\alpha}\ ln2}{Bt_{1/2}} \tag{4.1}$$

where B is the Barrier penetration probability obtained using WKB calculations. It is the decay rate in the absence of a potential barrier, and is related to the preformation probability of the α-particle in the parent nucleus.

Half-life calculations for the high-spin isomer ^{158m}W were made for various angular momenta, assuming the reduced width was that of ^{212}Po, which is assumed to be unhindered since it consists of doubly magic ^{208}Pb and an α-particle. When WKB half-live calculations were made, only a $\Delta l = 8$ transition was consistent with the experimental half-life, and the reduced width, shown in Table 4.4, was obtained accordingly. This supports the assignment Hofmann *et al.* [Hof89b] originally made of ^{158m}W being in a $[\nu f_{7/2}h_{9/2}]^{8+}$ shell model configuration. The reduced width of ^{158m}W implies a hindrance factor for the $\Delta l = 8$ decay of 19.4(28) compared to the reduced width of ^{212}Po and agrees well with the value calculated by Page *et al.* [Pag96]. It further emphasizes the similarities between the N=84 isomeric decays of ^{157m}Ta, ^{156m}Hf and ^{155m}Lu, all of which are believed to have $\Delta l = 8$ transitions with hindrance factors of ~20 and are therefore interpreted as having similar decay mechanisms — the odd Z isomeric decays being assigned to a $[\pi h_{11/2}\nu f_{7/2}h_{9/2}]^{25/2-}$ shell configuration [Hof89b, Pag96].

To calculate the reduced width of ^{162}Os, an α-branching ratio of 99% was used, obtained from the experimental half-life and the β-partial half-life predicted by Möller *et al.* [Mol97]. Since the α-partial half-life was

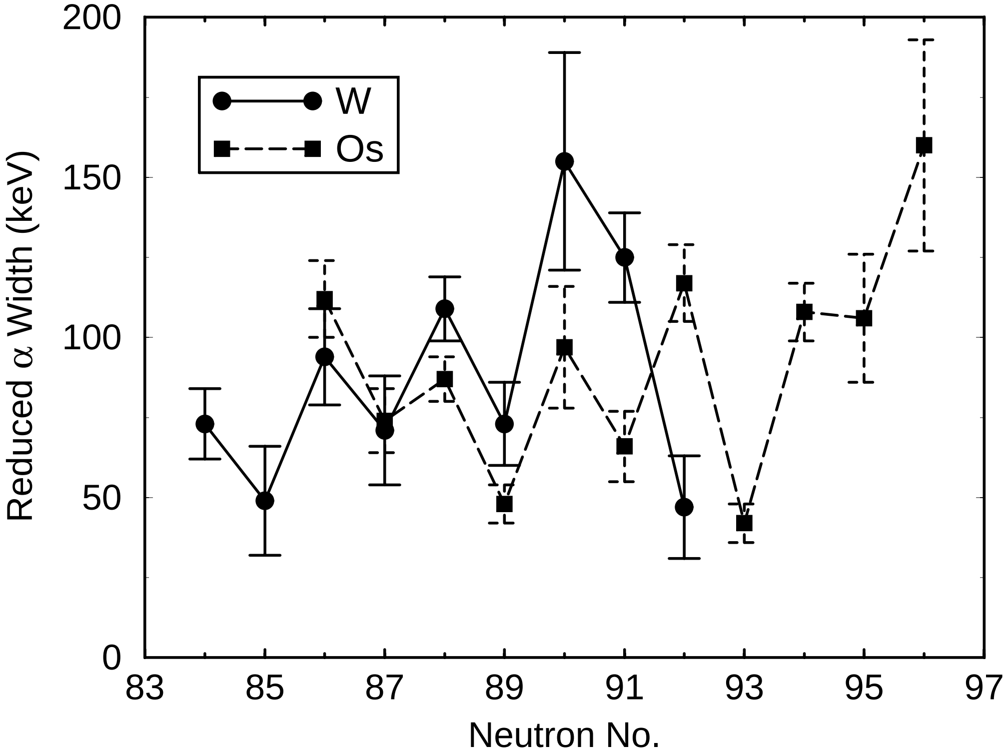

Figure 4.17: *Reduced α-decay width for Os and W neutron-deficient isotopes including the new data for* ^{162}*Os (N=86) and* ^{158}*W (N=84).*

so short, any uncertainty in the β half-life calculated in this model had a negligible affect on the branching ratio. The reduced width for ^{162}Os is in good agreement with those found in [Hof89b] and [Bin96], though with much smaller errors reflecting the more precise data obtained in this experiment. However, due to the longer half-life in the present work, the ^{158}W width is smaller than that calculated using the values from Page *et al.* [Pag96]. The α-reduced width for the known neutron deficient Os and W isotopes are shown in Fig. 4.17 as a function of neutron number, calculated with no angular momentum carried by the α-particle ($\Delta l = 0$) and using currently available data. The new data on ^{162}Os and ^{158}W now gives comparable, and in some cases improved precision compared to more stable isotopes. The present data continues a trend of odd-even staggering and the absolute reduced widths are broadly in agreement with neighbouring even-even isotopes. In particular, there is no evidence for an enhancement of the reduced width at N=84, corresponding to a transition from ^{158}W to ^{154}Hf at the N=82 major shell closure. This is similar to the situation at N=126 where a lack of enhancement of the reduced widths above the major shell closure has also been observed [Roe89].

4.4.4 Search for ^{161}Os

The possibility existed that the new $3n$ nucleus ^{161}Os may have been produced in the $^{58}Ni +^{106}Cd$ reaction, and would manifest itself by a fast, high energy α-decay. An upper limit on the cross-section of $\sigma \sim 3$ nb (corresponding to one full energy α-decay event) was estimated for the production of ^{161}Os. This represents a reduction of at least a factor of 100 for the $3n$

compared to the $2n$ evaporation channel estimated cross-section at this beam energy. HIVAP [Rei81] calculations predict a reduction in cross-section of only a factor of ~60. As a comparison, the nearby Pt isotope ^{167}Pt has been produced by a $3n$ evaporation channel with σ ~65 nb and indeed the $4n$ channel ^{166}Pt was measured with σ ~4 nb [Bin96]. The cross-section limit for ^{161}Os is, therefore, relatively low. It is noteworthy that ^{161}Os is predicted by Möller *et al.* to be the first two-proton unbound Os isotope [Mol97], and the proximity of the dripline could account for the dramatic reduction of the $2n$ to the $3n$ evaporation channel cross-section in this instance.

Chapter 5

Conclusion

5.1 Summary

A search for new examples of proton emission from ground and low-lying states was successfully conducted at Argonne National Laboratory. In particular, proton emission was observed in deformed, and odd-odd, proton emitters, and the results examined using the latest theoretical developments in the calculation of proton decay rates.

In an initial experiment, a measurement of the proton emitter ^{117}La, seen by Soramel *et al.* [Sor01], was combined with the search for a new proton emitter ^{116}La. The experimental proton decay rate was compared to calculations made by C. N. Davids, using the coupled-channel formalism of Esbensen and Davids [Esb00], and was found to be consistent with emission from a prolate deformed $3/2^{-}$ state, at the predicted deformation. One of the most interesting aspects of this experiment was that no evidence was found for a high spin isomer in ^{117}La reported by Soramel *et al.* [Sor01]. There was also a discrepancy of ~ 20 keV between the ANL and Legnaro results. One possible way to account for this is to recognise the technical difficulties experienced at Legnaro during their first positive proton radioactivity run, which are mentioned in Sec. 4.1. The results in this thesis represent measurements taken in the absence of a number of these difficulties. The search for ^{116}La yielded no new decays.

Data on proton emission from the new, deformed, odd-odd isotope ^{130}Eu was presented, this being one of the few $p5n$ channel proton emitters produced to date (with three of the four known produced at ANL), illustrating the progress in our ability to probe one step even further away from stability. The decay was assigned to the 2^+ ground state using a formalism by Ferreira and Maglione [Fer01]. This represents the first use of this formalism on a new isotope, providing an independent test of this formalism, and adding to the limited number of examples of odd-odd, deformed proton emitters. Some assumptions made in the odd-odd calculation were based on assignments of the neighbouring deformed isotope, ^{131}Eu, and the fact the this calculation was then successful provides a certain level of confidence on the previous work done on ^{131}Eu.

The new isotope, ^{170}Au, was also observed with a proton line from the $h_{11/2}$ proton orbital, probably in the $[\pi h_{11/2}, \nu h_{9/2}]10^+$ state, with a reasonable experimental spectroscopic factor of $S_{exp} = 0.21^{+0.08}_{-0.12}$. This assignment was made on the basis of a comparison of measured proton half-lives with those calculated using WKB barrier penetration calculations. A high energy α-decay line is also reported from this new nucleus, calculations from data on this decay branch which supported the assignment made. An independent observation of the proton decay of the spherical odd-odd isotope

^{164m}Ir was also made in the same experimental run. The observed proton line was assigned to the $h_{11/2}$ proton orbital with a spectroscopic factor $S_{exp} = 0.35^{+0.29}_{-0.13}$, which was in good agreement with theoretical predictions and is therefore consistent with ^{164m}Ir being a near spherical nucleus. All the results for this nucleus were in good agreement with the observation by Kettunen *et al.* at JYFL [Ket01]. The results for these two nuclei indicate that the spherical proton emitters just below Z=82 are now reasonably well understood, with a number of known states which are explained using current theoretical approaches.

5.2 Further Progress

Beyond 2000, when the experiments in this thesis were performed, various improvements have been made to the experimental setup at the FMA, the first of which was the addition of a 80 × 80 DSSD, shown in Fig. 5.1. This combines the granularity of the 48×48 with the a larger area, and was commissioned by the ANL/Edinburgh collaboration in 2001 with the search for ^{135}Tb [Mun02].

The development of the new DSSD has been coupled with a new PPAC transmission detector, able to withstand a rate of at least 20 kHz, as well as a new split anode for the FMA to cut down on scattered beam. The split anode has a gap that enables the beam to be dumped on a beam spot situated away from the central path of the FMA, inhibiting any scattering beam particles from following this path through to the end of the FMA. This results in a higher proportion of true recoils reaching the detector setup. New delay-line amplifiers have also been developed, able to quickly recover from

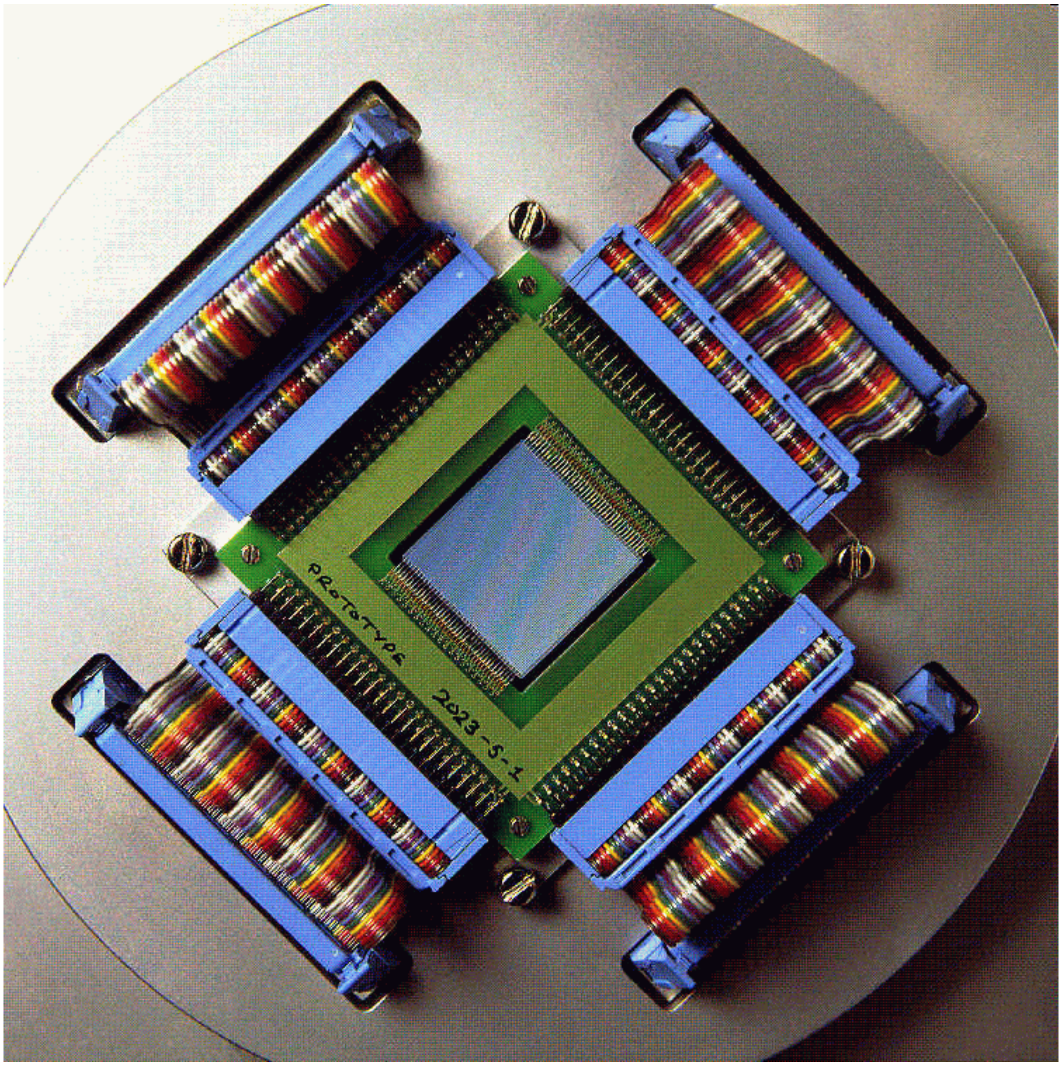

Figure 5.1: *The* 80×80 *DSSD.*

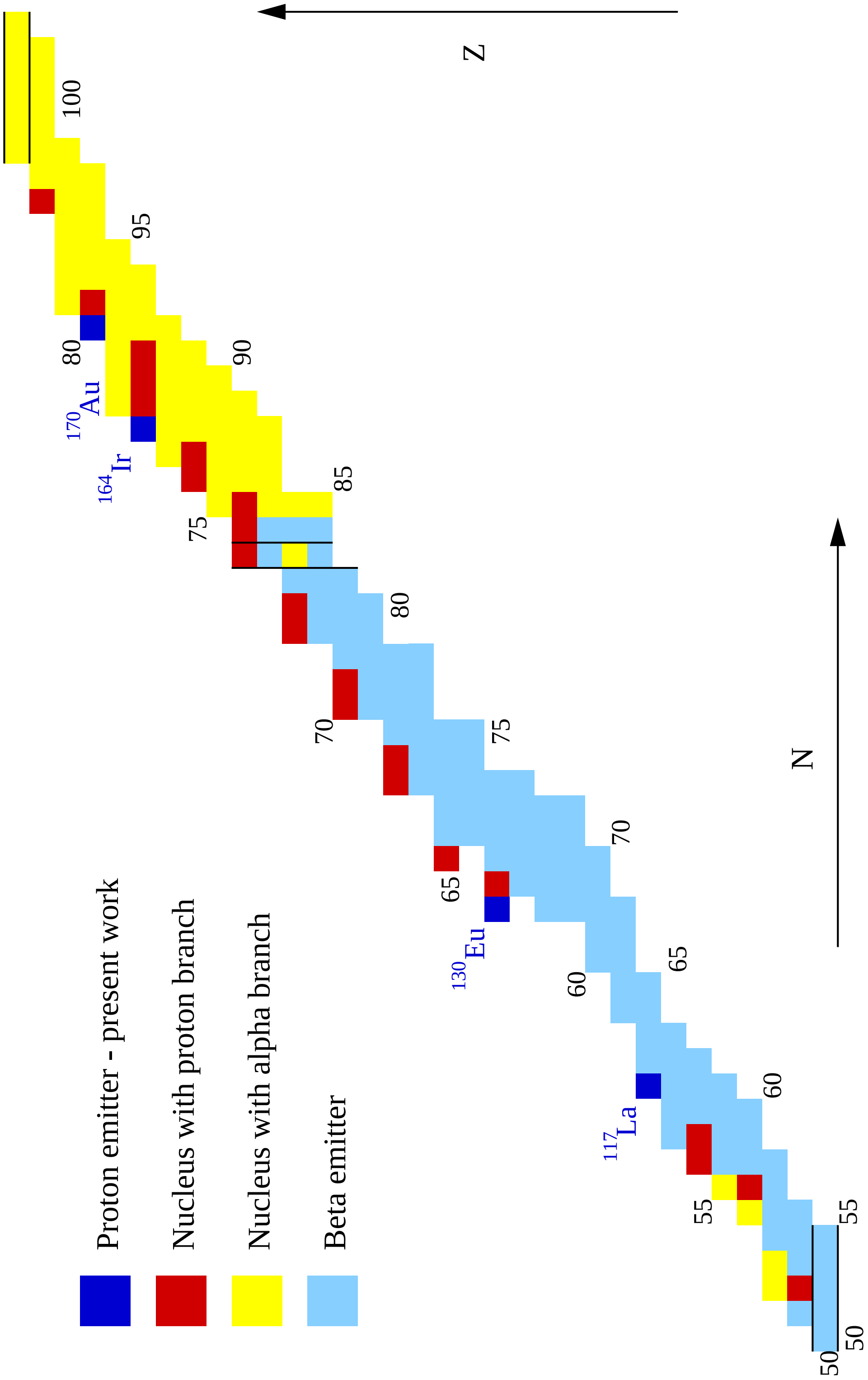

Figure 5.2: *The proton dripline from Z=50-82.*

implant signals, and accept decays within 2 μs of an implantation. The final component of this upgrade program will be updating the acquisition system to handle higher rates, along with a faster FERA system. When combined, these upgrades will increase the acceptable rates by almost an order of magnitude, improving the sensitivity of the system.

A number of avenues may become accessible in the field as a result of increased sensitivity. As one can see in Fig. 5.2, the sequence of proton emitters between $50 < Z < 82$ is nearly complete, with praseodymium and promethium being the last two elements sought. The candidate isotopes here are ^{121}Pr and ^{125}Pm which are the subject of current investigation at the time of writing. One can also push further beyond the currently known proton emitters, such as looking for ^{129}Eu, which should be faster than the other europium proton emitters, with a predicted proton energy of 1.5 MeV [Abo95]. A common theme of current interest in the field is using proton spectroscopy to examine deformed nuclei. Of particular interest would be new examples of deformed, odd-odd proton emitters to further test our new theoretical methods to understand the process of emission through a deformed potential. Work presented in this thesis shows that progress has been made, though efforts are still ongoing.

Fine-structure is of particular fascination, providing an even more sensitive probe of proton emission from odd-even deformed nuclei such as ^{145}Tm. For odd-odd nuclei, the situation can be less straightforward since the levels schemes of both the daughter and parent may be complex, such as with ^{146}Tm where five proton lines have been observed from its ground and isomeric state to various states in the daughter nucleus ^{145}Er [Ryk01]. This is the first example of proton fine-structure decay to more than one excited state in the daughter, and added statistics may clarify or confirm some of the tentative assignments made in the original observation. Coupled with the search for the new examples of proton emission and fine-structure decay, one could take advantage of the return of Gammasphere to the FMA, and perform RDT experiments on some of the most interesting nuclei in the region since, to date, very few proton emitters have been studied using γ-spectroscopy.

One could take the opportunity to consolidate our understanding of the proton emitters already known, such as performing an independent measurement of ^{105}Sb, which has only been observed in the original experiment, despite several attempts at other laboratories to repeat the observation. Searches for alternative states in known proton emitting nuclei could be undertaken, for example, the ground state of ^{170}Au should be observable with the improved system at ANL. An option to improve the sensitivity of certain experiments would be the increased use of gas-filled spectrometers which have larger transmission efficiencies then conventional mass separators, though at the cost of mass selectivity. These would be generally more beneficial when looking for slightly heavier proton emitters, in the region where α-daughters are common and can provide clear identification of unknown decays through correlations.

Having nearly completed the sequence of $50 < Z < 82$ proton emitters, the search for new proton emitters will shift further to heavier elements $(Z > 82)$, of which ^{185m}Bi is the only current example. In this regard, the improved sensitivity of new experimental systems, or the use of gas-filled spectrometers, could play an important role in the search for candidates such as $^{191,189}At$, where fission is a major consideration, limiting the implantation rate of candidate recoils ions in the detector. A side benefit of this search would be the study of α-decays, this being a common decay mode for these heavier, proton rich nuclei. An alternative production mechanism for heavy proton emitters that has been proposed is fragmentation reactions using heavy beams such as uranium, where very high luminosity beams could offset low cross-sections. This method of accessing the proton dripline has been successfully used at GSI in the recent observation of the two proton emitter, ^{45}Fe [Pfü02]. A major factor contributing to this success was the presence of fast, charge reset pre-amplifiers which enabled the detection of fast decays occurring after the huge (∼1 GeV) implantation signal

In closing, one can state that the study of proton radioactivity has provided structural information on nuclei far beyond the limits of stability, as well as allowing us further opportunities to explore the phenomenon of tunnelling through a potential barrier, whether spherical or deformed. One can also see how new experimental discoveries have fuelled theoretical efforts in the field. Now that a large portion of the proton dripline from $50 < Z < 82$ has been probed, one can plan for future work among the heavier elements of the proton dripline.

Bibliography

[Åbe97] S. Åberg, P. B. Semmes and W. Nazarewicz, Phys. Rev. C **56**, 1762 (1997).

[Abo95] Aboussir *et al.*, At. Data Nucl. Data Tables **61**, 127 (1995).

[Ars69] D. A. Arseniev, A, Sobiczewski and V. G. Soloviev, Nucl. Phys. A **126**, 15 (1969).

[Aud95] G. Audi and A. H. Wapstra, Nucl. Phys. A **595**, 409 (1995).

[Axe98] L. Axelsson *et al.*, Nucl. Phys. A **634**, 475 (1998)

[Bar63] R. Barton *et al.*, Can. J. Phys. **41**, 2007 (1963).

[Bar74] A. R. Barnett *et al.*, Comp. Phys. Com. **8**, 377 (1974).

[Bat98] J. C. Batchelder *et al.*, Phys. Rev. C **57**, R1042 (1998).

[Bec69] F. D. Becchetti, Jr. and G. W. Greenlees, Phys. Rev. **182**, 1190 (1969).

[Bei75] M. Beiner *et al.*, *Proc. 5th Int. Conf. on At. Masses and Fund. Consts.*, eds. J. H. Sanders and A. Wapstra, Plenum, New York (1975).

[Ben85] T. Bengtsson and I. Ragnersson, Nucl. Phys. A **436**, 14 (1985).

[Bet36] H. A, Bethe and R. F. Bacher, Rev. Mod. Phys. **8**, 82 (1969).

[Bev92] P. R. Bevington and D. K. Robinson, *Data Reduction and Error Analysis for the Physical Sciences*, 2nd Ed. McGraw-Hill, (1992).

[Bin96] C. R. Bingham *et al.*, Phys. Rev. C **54**, R20 (1996).

[Bla96] B. Blank *et al.*, Phys. Rev. Lett. **77**, 2893 (1996).

[Blu96] D. J. Blumenthal, http://www.phys.anl.gov/fma/fmarecoil_form.html (1996).

[Boc92] O. V. Bochkarev *et al.*, Sov. J. Nucl. Phys. **55**, 955 (1992).

[Boh69] A. Bohr and B. R. Mottelson, *Nuclear Structure*, Vol. I, McGraw-Hill, (1969).

[Bug85] V. P. Bugrov *et al.*, Sov. J. Nucl. Phys. **41**, 717 (1985).

[Bug89] V. P. Bugrov and S. G. Kadmenskii, Sov. J. Nucl. Phys. **49**, 107 (1989).

[Cai02] X. Z. Cai *et al.*, Phys. Rev. C **65**, 024610 (2002).

[Cas00] R. J. Casten, *Nuclear Structure from a Simple Perspective*, Oxford, 2nd Ed. (2000).

[Cer70] J. Cerny *et al.*, Phys. Lett. B **33**, 284 (1970).

[Chr02] M. J. Chromik *et al.*, Phys. Rev. C **66**, 024313 (2002).

[Com88] E. Comay, I. Kelson and A. Zidon, At. Data Nucl. Data Tables **39**, 235 (1988).

[Cwi87] S. Cwiok *et al.*, Comput. Phys. Commun. **46**, 379 (1987).

[Dav89] C. N. Davids and J. D. Larson, Nucl. Instr. and Meth. B **40/41**, 1224 (1989).

[Dav90] T. Davinson *et al.*, Nucl. Instrum. Methods Res. A **288**, 245 (1990).

[Dav92] C. N. Davids *et al.*, Nucl. Instr. and Meth. B **70**, 358 (1992).

[Dav96] C. N. Davids *et al.*, Phys. Rev. Lett. **76**, 592 (1996).

[Dav97] C. N. Davids *et al.*, Phys. Rev. C **55**, 2255 (1997).

[Dav98] C. N. Davids *et al.*, Phys. Lett. **80**, 1849 (1998).

[Dav00a] C. N. Davids and H. Esbensen, Phys. Rev. C **61**, 054302 (2000).

[Dav00b] C. N. Davids, *Proc. PROCON'99* ed. J. C. Batchelder, AIP, New York, 200 (2000).

[Dav00c] C. N. Davids *et al.*, ANL Sci. Rep. PHY-9694-HI-2000 (2000).

[Dav01] C. N. Davids and H. Esbensen, Phys. Rev. C **64**, 034317 (2001).

[D'Au78] J. M. D'Auria *et al.*, Nucl. Phys. A **301**, 397 (1978).

[Dud80] J. Dudek, A. Majhofer and J. Skalski, J. Phys. G **6**, 447 (1980).

[Esb00] H. Esbensen and C. N. Davids, Phys. Rev. C **63**, 014315 (2000).

[Fae84] T. Faestermann *et al.*, Phys. Lett. B **137**, 23 (1984).

[Fer00] L. S. Ferreira and E. Maglione, Phys. Rev. C **61**, 021304R (2000).

[Fer01] L. S. Ferreira and E. Maglione, Phys. Rev. Lett. **86**, 1721 (2001).

[Fer02] L. S. Ferreira, E. Maglione and D. E. P. Fernandes, Phys. Rev. C **65**, 024323 (2002).

[Fes92] H. Feshbach, *Theoretical Nuclear physics: Nuclear Reactions*, Wiley (1992).

[Gam28] G. Z. Gamow, Phys. **51**, 204 (1928).

[Gil87] A. Gillitzer *et al.*, Z. Phys. A **326**, 107 (1987).

[Gio01] J. Giovinazzo *et al.*, Eur. Phys. J. A **10**, 73 (2001).

[Gio02] J. Giovinazzo *et al.*, Nucl. Phys. A *to be published* (2002).

[Gol60] V. I. Goldanskii, Nucl. Phys. **19**, 482 (1960).

[Gol66] V. I. Goldanskii, Ann. Rev. Nucl. Phys. **16**, 1 (1966).

[Gro62] L. Grodzins, Phys. Lett. **2**, 88 (1962).

[Hax49] O. Haxel, J. H. D. Jensen and H. E. Suess, Phys. Rev. **75**, 1766 (1949).

[Hey94] K. Heyde, *The Nuclear Shell Model*, Springer-Verlag, Berlin, (1994).

[Hof81a] S. Hofmann *et al.*, *Proc. 4th Int. Conf. on Nuclei Far From Stability*, eds. P. G. Hansen and O. B. Nielson, CERN 81-09, CERN, Geneva, 190 (1981).

[Hof81b] S. Hofmann *et al.*, Z. Phys. A **299**, 281 (1981).

[Hof82a] S. Hofmann *et al.*, Z. Phys. A **305**, 111 (1982).

[Hof82b] S. Hofmann *et al.*, GSI Sci. Rep. 1981 **GSI 81-1**, 241 (1982).

[Hof84] S. Hofmann *et al.*, *Proc. 7th Int. Conf. on Atomic Masses and Fundamental Constants*, ed. O. Klepper, THD-Schriftenreihe Wissenschaft und Technik, 26 (1984).

[Hof89a] S. Hofmann, *Particle Emission from Nuclei*, Vol. 2, eds. D. N. Poenaru and M. S. Ivascu, CRC Press Inc., Florida, 25 (1989).

[Hof89b] S. Hofmann *et al.*, Z. Phys. A **333**, 107 (1989).

[Hua76] K.-N. Huang and H. Mark, At. Data Nucl. Data Tables **18**, 243 (1976).

[Irv97] R. J. Irvine *et al.*, Phys. Rev C **55**, R1621 (1997).

[Jac70] K. P. Jackson *et al.*, Phys. Lett. B **33**, 281 (1970).

[Kar63] V. A. Karnaukhov, G. M. Ter-Akopian and V. G. Subbotin, *Proc. Asilomar Conf. reactions between complex Nuclei*, eds. A. Ghiorso, R. M. Diamond and H. E. Conzett, University of California Press, Berekley, Calif., 434 (1963).

[Kad96] S. G. Kadmensky and V. P. Bugrov, Phys. At. Nucl. **59** 399 (1996).

[Käp98] F. Käppler, F.-K. Thielmann and M. Wiescher, Ann. Rev. Nucl. Part. Sci. **48**, 175 (1998).

[Ker56] A. K. Kerman, Mat. Fys. Medd. K. Dan. Vidensk. Selsk. **20** (1956).

[Ket01] H. Kettunen *et al.*, Acta Phys. Pol. B **32**, 989 (2001).

[Kle82] O. Klepper *et al.*, Z. Phys. A **305**, 125 (1982).

[Koo90] S. E. Koonin and D. C. Meredith, *Computational Physics*, Addison-Wesley Pub. Co. (1990).

[Kry95] R. A. Kryger *et al.*, Phys. Rev. Lett. **74**, 860 (1995).

[Lar83] P. O. Larsson *et al.*, Z. Phys. A **314**, 9 (1983).

[Law80] R. D. Lawson, *Theory of the Nuclear Shell Model*, Clarendon, Oxford, (1980).

[Lea82] G. A. Leander and P. Möller, Phys. Lett. B **110**, 17 (1982).

[Len86] W. N. Lennard *et al.*, Nucl. Instr. Meth. Phys. Res. A **248**, 454 (1986).

[Lew99] R. Lewis and A. C. Hayes, Phys. Rev. C **59**, 1211 (1999).

[Lip60] H. J. Lipkin, Ann. Phys. N. Y. **9**, 272 (1960).

[Lir76] S. Liran and N. Zeldes, At. Data Nucl. Data Tables **17**, 431 (1976).

[Lis85] C. J. Lister *et al.*, Phys. Rev. Lett. **55**, 810 (1985).

[Liv93] K. Livingston *et al.*, Phys. Lett. B **312**, 46 (1993).

[Mag98] E. Maglione, L. S. Ferreira and R. J. Liotta, Phys. Rev. Lett. **81**, 538 (1998).

[Mag99] E. Maglione, L. S. Ferreira and R. J. Liotta, Phys. Rev. C **59**, R589 (1999).

[Mag00] E. Maglione and L. S. Ferreira, Phys. Rev. C **61**, 047307 (2000).

[Mah00] H. Mahmud *et al.*, Phys. Rev. C **62**, 057303 (2000).

[Mah01] H. Mahmud *et al.*, Phys. Rev. C **64**, R031303 (2001).

[Mah02a] H. Mahmud *et al.*, Eur. J. Phys. A *15*, 85 (2002).

[Mah02b] H. Mahmud *et al.*, Phys. Rev. C *to be published* (2002).

[Man64] H. J. Mang, Ann. Rev. Nuc. Sci. **14**, 1 (1964).

[May49] M. G. Mayer, Phys. Rev. **169**, 1969 (1949).

[Mol74] P. Möller and J. R. Nix *Proc. Third IAEA Symp. on Phys. and Chem. of Fission, Vol. 1* IEAE, Vienna, 103 (1974).

[Mol95] P. Möller *et al.*, At. Data Nucl. Data Tables **59**, 185 (1995).

[Mol97] P. Möller *et al.*, At. Data Nucl. Data Tables **66**, 131 (1997).

[Mom00] M. Momayezi *et al.*, *Proc. PROCON'99* ed. J. C. Batchelder, AIP, New York, 307 (2000).

[Mot55] B. R. Mottelson and S. G. Nilsson, Phys. Rev. **99**, 1615 (1955).

[Mun79] G. Münzenberg *et al.*, Nucl. Instr. and Meth. **161**, 65 (1979).

[Mun02] P. Munro *et al.*, *private communcations.*

[Mye76] W. D. Myers, At. Data Nucl. Data Tables **17**, 411 (1976).

[Mye77] W. D. Myers, *Droplet Model of the Atomic Nucleus*, Plenum, New York (1977).

[Naz90] W. Nazarewicz, M. A. Riley and J. D. Garrett, Nucl Phys. A **512**, 61 (1990).

[Nog64] Y. Nogami, Phys. Rev. B **134**, 313 (1964).

[Pag92] R. D. Page *et al.*, Phys. Rev. Lett. **68**, 1287 (1992).

[Pag94] R. D. Page *et al.*, Phys. Rev. Lett. **72**, 1798 (1994).

[Pag96] R. D. Page *et al.*, Phys. Rev. C **53**, 660 (1996).

[Pai81] G. Paić *et al.*, Nucl. Instr. and Meth. **188**, 119 (1981).

[Pat99] Z. Patyk *et al.*, Phys. Rev. C **59**, 704 (1999).

[Per57] I. Perlman and J. O. Rasmussen, *handbuck der Physik*, Vol. 42, Springer-Verlag, (1957).

[Pfü02] M. Pfützner *et al.*, Eur. Phys. J. A, *to be published*, 73 (2002).

[Poe89] *Particle Emission from Nuclei*, Vol. 3, eds. D. N. Poenaru and M. S. Ivascu, CRC Press Inc., Florida (1989).

[Pol99] G. L. Poli *et al.*, Phys. Rev. C **59**, R2979 (1999).

[Pol01] G. L. Poli *et al.*, Phys. Rev. C **63**, 044304 (2001).

[Ras59] J. O. Rasmussen, Phys. Rev. **113**, 1593 (1959).

[Rei81] W. Reisdorf, Z. Phys. A **300**, 227 (1981).

[Rei85] W. Reisdorf, Nuc. Phys. A **444**, 154 (1985).

[Res00] J. J. Ressler *et al.*, Phys. Rev. C **84**, 2104 (2000).

[Rin80] P. Ring and P. Schuck, *The Nuclear Many-Body Problem*, Springer-Verlag, (1980).

[Roe89] E. Roekl and D. Schardt, *Particle Emission from Nuclei*, Vol. 2, eds. D. N. Poenaru and M. S. Ivascu, CRC Press Inc., Florida, 14 (1989).

[Rud98] D. Rudolph *et al.*, Phys. Rev. Lett. **80**, 3018 (1998).

[Rud02] D. Rudolph *et al.*, Phys. Rev. Lett. **89**, 022501 (2002).

[Rut16] E. Rutherford and A. B. Wood, Philos Mag. **31**, 379 (1916).

[Ryk99] K. Rykaczewski *et al.*, Phys. Rev. C **60**, 011301 (1999).

[Ryk01] K. Rykaczewski *et al.*, Nucl. Phys. A **682**, 270c (2001).

[Sch79] D. Schardt *et al.*, Nucl. Phys. A **326**, 65 (1978).

[Sch84] K.-H. Schmidt *et al.*, Z. Phys. A **316**, 19 (1984).

[Sel92] P. J. Sellin *et al.*, Nucl. Instrum. Methods Res. A **311**, 217 (1992).

[Sel93] P. J. Sellin *et al.*, Phys. Rev. Lett. **47**, 1458 (2001).

[Sew01a] D. Seweryniak *et al.*, Nucl. Phys. A **682**, 247c (2001).

[Sew01b] D. Seweryniak *et al.*, Phys. Rev. Lett. **86**, 1458 (2001).

[Sew02] D. Seweryniak *et al.*, Phys. Rev. C. *in preparation*, 1458 (2002).

[She61] R. K. Sheline, T. Sikkeland and R. N. Chanda, Phys. Rev. Lett. *7*, 446 (1961).

[She69] H. Sherif, Phys. Rev. Lett. **131**, 532 (1969).

[Smi98] J. F. Smith *et al.*, Phys. Rev. C **57**, R1037 (1998).

[Son99] A. A. Sonzogni *et al.*, Nuc. Phys. A **183**, 1116 (1999).

[Sor66] R. A. Sorensen, E. D. Lin and B. L.Cohen, Phys. Rev. **142**, 729 (1966).

[Sor00] F. Soramel, *Proc. PROCON'99* ed. J. C. Batchelder, AIP, New York, 68 (2000).

[Sor01] F. Soramel *et al.*, Phys. Rev. C **63**, R031304 (2001).

[Str67] V. M. Strutinsky, Nucl. Phys. A **95**, 420 (1967).

[Str68] V. M. Strutinsky, Nucl. Phys. A **122**, 1 (1968).

[Tac88] T. Tachibana *et al.*, At. Data Nucl. Data Tables **39**, 251 (1988).

[Tan85] I. Tanihata *et al.*, Phys. Rev. Lett. **55**, 2676 (1985).

[Tho90] S. L. Thomas, T. Davinson and A. Shotter, Nucl. Instrum. Methods Res. A **288**, 212 (1990).

[Tho00] M. Thoennessen, M. J. Chromik and P. G. Thirolf, *Proc. PROCON'99* ed. J. C. Batchelder, AIP, New York, 105 (2000).

[Tig94] R. J. Tighe *et al.*, Phys. Rev. C **49**, R2871 (1994).

[Uts01] Yutaka Utsana *et al.*, Phys. Rev. C **64**, 011301R (2001).

[Uus99] J. Uusitalo *et al.*, Phys. Rev C **59**, R2975 (1999).

[Ver84] D. Vermeulen *et al.*, Z. Phys. A **318**, 157 (1984).

[Wei35] C. F. von Weizsäcker, Z. Phys. A **96**, 431 (1935).

[Woo54] R. D. Woods and D. S. Saxon, Phys. Rev **95**, 577 (1954).

[Woo89] P. J. Woods *et al.*, Nucl. Instr. and Meth. A **276**, 196 (1989).

[Woo97] P. J. Woods and C. N. Davids, Ann. Rev. Nucl. Part. Sci. **47**, 541 (1997).

[Yan96] F. Yang and J. H. Hamilton, *Modern Atomic and Nuclear Physics*, McGraw-Hill, (1996).